論文 / 著書情報
Article / Book Information

題目(和文)	無線リソース冗長化を活用したミリ波帯移動通信システムに関する研究
Title(English)	Design of Millimeter-wave Mobile Communication Systems Based on Redundant Radio Resource Control
著者(和文)	岩渕匡史
Author(English)	Masashi Iwabuchi
出典(和文)	学位:博士(工学), 学位授与機関:東京工業大学, 報告番号:甲第12371号, 授与年月日:2023年3月26日, 学位の種別:課程博士, 審査員:廣川 二郎,阪口 啓,青柳 貴洋,西方 敦博,TRAN GIA KHANH
Citation(English)	Degree:Doctor (Engineering), Conferring organization: Tokyo Institute of Technology, Report number:甲第12371号, Conferred date:2023/3/26, Degree Type:Course doctor, Examiner:,,,,
学位種別(和文)	博士論文
Type(English)	Doctoral Thesis

Doctoral Dissertation

Design of Millimeter-wave Mobile Communication Systems Based on Redundant Radio Resource Control

Supervisors Professor Kei Sakaguchi

Department of Electrical and Electronic Engineering
School of Engineering
Tokyo Institute of Technology

Masashi Iwabuchi

Contents

List of Figures

List of Tables

Acronyms

3GPP 3rd Generation Partnership Project. 1, 7, 8, 59, 77–79, 81, 102, 106

4G Fourth generation mobile communications. 1

5G Fifth generation mobile communications. 1–3, 8

ACK Acknowledge ACknowledge. vii, 8, 85, 87

AF Amplifier-and-Forward. 7, 55

AMC Adaptive Modulation and Coding. 92, 97, 103, 106

AR Augmented Reality. 1

ARU Analog Radio Unit. 14, 20, 28, 31, 32, 46

BBU BaseBand Unit. 89

BS Base Station. 14, 28, 31, 32, 36, 37, 42, 46, 58, 59, 64, 73, 78–80, 83, 87, 90

CAM Cooperative Awareness Message. 50, 55, 61, 63, 70, 73, 75, 106

CC Component Carrier. 23, 36

CDD Cyclic Delay Diversity. 28

CPE Customer Premises Equipment. 14, 28, 31, 32, 35, 39, 42

CSI-RS Channel State Information Reference Signal. 20, 23, 58

DF Decode-and-Forward. 7, 55

DL Downlink. 8, 13, 18, 20, 22, 39, 42, 46, 55, 78–80, 83, 85–87, 92, 93, 95, 97

DMRS DeModulation Reference Signal. 87

eMBB enhanced Mobile BroadBand. 1, 3

FDD Frequency Division Duplex. 8

GNSS Global Navigation Satellite System. 59, 73

GPS Global Positioning System. 59

HAPS High Altitude Platform Station. 2

HARQ Hybrid Automatic ReQuest. 8, 79, 80, 86, 92

IAB Integrated Access and Backhaul. 7

ITS Intelligent Transport Systems. 50, 55

ITU-R International Telecommunication Union - Radio communication sector. 1

KPI Key Performance Indicator. 78

LDPC Low Density Parity Check. 23

LiDAR Light Detection And Ranging. 59, 61, 73

LOS Line-Of-Sight. 3, 59

LTE Long Term Evolution. 1

MCS Modulation and Coding Scheme. 86, 90, 97

MIMO Multiple Input Multiple Output. 2, 7, 9, 28, 39, 49, 50, 55, 57, 58, 62–64, 67, 70, 75, 106

mMTC massive Machine Type Communications. 1

mmWave Millimeter wave. 5–7, 9, 13, 14, 18, 28, 39, 42, 46, 49, 50, 55, 58, 59, 64, 78, 103, 105, 106

MR Mixed Reality. 1

NACK Negative ACknowledge. vii, 8, 85, 87, 92

NLOS Non Line-Of-Sight. 3, 32, 35, 39, 42, 46, 59, 64, 87, 103, 105, 106

NR New Radio Access Technologies. 2, 8, 61, 62, 70, 77, 78, 81

NTN Non-Terrestrial Networks. 2

OFDM Orthogonal Frequency Division Multiplexing. 2, 8, 23, 79, 81, 83, 91, 93, 103, 106

OFDMA Orthogonal Frequency Division Multiple Access. 18

PRB Physical Resource Block. 79, 86

QAM Quadrature Amplitude Modulation. 23, 36, 90

QPSK Quadrature Phase Shift Keying. 23, 90, 97

RAN Radio Access Networks. 2

RF Radio Frequency. 14, 20, 28, 32

RFU Radio Frequency Unit. 89

RIS Reconfigurable Intelligent Surface. 7

RTT Round Trip Time. 79, 80, 86

SDU Service Data Unit. 78, 79

SFBC Space-Frequency Block Coding. 28, 87, 90

SNR Signal-to-Noise Ratio. 87, 93, 95, 97, 103

SVD Singular Value Decomposition. 57, 64

TB Transport Block. 86, 90, 92, 95, 97

TDD Time Division Duplex. 2, 8, 18, 78–81, 89

TM Transmission Mode. 23, 28, 31, 36, 37

TTI Transmission Time Interval. 77

UE User Equipment. iv, 8, 18, 20, 22, 32, 35, 42, 46, 50, 55, 57–59, 61–64, 67, 70, 72, 73, 75, 79, 83, 87, 89, 90, 106

UL Uplink. 8, 20, 79, 83, 85–87, 92, 93, 95, 97

URLLC Ultra-Reliable and Low Latency Communications. 1, 3, 6, 9, 77–80, 85, 86, 102, 103, 106

V2X Vechcular-to-Everything. iv, 7, 50, 56, 59, 61, 70, 73, 75

VR Virtual Reality. 1

Abstract

Toward fifth-generation mobile communications (5G) and beyond 5G, higher speed and higher capacity communications are expected. To enhance the performances, higher frequency bands are developed. Vehicle-to-Everything (V2X) is one of use cases and a typical V2X application is an autonomous-driving car. To safely control an autonomous vehicle, a large amount of data exchange is required among vehicles, road-side units and networks. Therefore, higher capacity communications using higher frequency bands is needed. However, applying millimeter-wave bands to mobile communications has some issues. The typical examples are smaller coverage areas caused by significant pathloss and Multiple-Input Multiple-Output (MIMO) stream reduction due to less scattering. To solve these issues, this research focuses to radio resource redundancy. Firstly, the performance of millimeter-wave bands in mobile communications is experimentally verified. 39-GHz band device with beam tracking is installed to a vehicle and evaluated the performance. The evaluations clarify that mobile communication with high data rate is possible. On the other hand, we also show that millimeter-wave bands have smaller coverage in non-line-of-sight (NLOS) and limitation of spatial multiplexing. Secondly, to solve the issues, massive analog-relay MIMO is proposed as redundancy of spatial resources. The proposed system can improve coverage in NLOS and enhance the spatial multiplexing to a single user. Furthermore, relay-beam tracking method utilizing cooperative awareness message, which is one of intelligent transport system messages, is proposed. It is clarified that the proposed method can obtain the benefit of massive analog-relay MIMO while keeping the overhead of beamforming for analog relay. Finally, the redundancy of time resources is considered. The reception quality is improved by transmitting the same radio signal using different time resources and combining the received signals. Since latency is a concern in time redundancy, a fast retransmission method based on 5G air interface is also experimentally verified. The experiment shows that redundancy of time resource contributes to improvement of transmission success probability.

Acknowledgments

I would like to thank everyone who helped me in writing this thesis. We would like to express our sincere gratitude. I would like to thank my supervisor, Prof. Kei Sakaguchi, for his kind guidance and support in accomplishing this research. His advice and support throughout this research have been instrumental in helping me. I would also like to thank Prof. Hirokawa, Associate Prof. Tran, Associate Prof. Nishikata, Associate Prof. Aoyagi, and Specially Appointed Prof. Fujii as my committee members who gave me much grateful advice to improve the quality of this thesis and research. Furthermore, I am grateful to emeritus Prof. Araki and special Associate Prof. Yu Tao for their valuable advice during my seminar presentations. I would also like to thank Ms. Minami and Ms. Funabashi for their kindness and assistance in my lab Life.

I would also like to thank my supervisors and colleagues at NTT Access Service Systems Laboratories and NTT DOCOMO., especially Dr. Yasushi Takatori, Mr. Tomoaki Ogawa, Dr. Yoghitha Ramamoorthi, Mr. Takahiro Asai, Dr. Yoshihisa Kishiyama, Dr. Satoshi Suyama, Dr. Anass Benjebbour and all concerned, for their support. In chapters 2 and 4 of this thesis, I received a lot of cooperation from the members of Huawei Technologies and Huawei Technologies Japan at the time, especially Mr. Tingjian Tian, Ms. Guangmei Ren, Mr. Liang Gu, Dr. Yang Cui and Mr. Terufumi Takada. I would like to express my deep gratitude to everyone involved.

Finally, I would also like to give special thanks to my family for their continuous support and understanding throughout the activity to complete this research and writing this research.

Chapter 1

Introduction

1.1 Background

1.1.1 Radio access networks toward 5G and beyond

Research and development activities on the fifth generation mobile communications (5G), which is the next generation following the fourth generation mobile communications (4G) also called Long Term Evolution (LTE) or LTE-Advanced, have been conducted around the world. 5G system is a key component in our future networked society and handles the explosive increase in mobile traffic and the diversification of services. Mobile network data traffic is expected to continuously increase at an annual average of 46 % and reach 77 exabytes per month by 2022 [1]. New applications using mobile communication, such as Augmented Reality (AR)/Virtual Reality (VR)/ Mixed Reality (MR), smart factories and autonomous driving, are also expected.

5G requires extendibility for such various services. To meet these demands in a timely fashion, the vision of the International Telecommunication Union - Radio communication sector (ITU-R) for mobile communication systems in 2020 and beyond was published in September 2015 where three typical usage scenarios for 5G were identified [2]. These are (1) enhanced Mobile BroadBand (eMBB), (2) massive Machine Type Communications (mMTC), supporting massive numbers of simultaneous connections, and (3) Ultra-Reliable and Low Latency Communications (URLLC) [2, 3]. After defining target 5G requirements [3], the 3rd Generation Partnership Project (3GPP), which is a standardization organization for mobile communications systems, initiated work on 5G radio interface specifications in March 2016.

The first edition of the 5G specifications called Release 15 was released in December 2017 [4], and commercial services were started from 2020 in Japan.

In 5G, new radio access technologies (NR) have been standardized to support various requirements. Among the various technologies that have been adopted, the key technologies are as follows.

- Development of higher frequency bands (including millimeter-wave bands)
- Advanced antenna technologies (e.g. massive MIMO)
- Flexible air interface design (e.g. Various OFDM subcarrier spacing, new reference signal configuration, dynamic TDD)

In particular, the development of the higher frequency band was noted as an approach to significantly improve the system capacity of mobile communications. In many countries, 5 GHz and 28 GHz bands are allocated and commercialized for 5G.

Currently, research and development on the sixth-generation mobile communication system (6G) have been started around in some research communities [5, 6, 7]. In addition to further improving the performance of Radio Access Networks (RAN), 6G is expected to achieve multiple requirements combined. Furthermore, the coverage expansion is also attracting attention. It is expected to incorporate Non-Terrestrial Networks (NTN) such as satellites and High Altitude Platform Station (HAPS) into mobile communications. In order to further improve the performance in 6G, the development of new frequency bands is essential. The development of the high frequency band is still under consideration, and it is trying to reach the sub-terrahertz bands such as 100 GHz or more. Technical updates and improvements to utilize the millimeter wave bands also continue to be discussed. The utilization of the higher frequency bands is an approach that can greatly improve the performance of RAN, and further development is expected. However, since there are many issues in the use of higher frequency bands, further technological evolution is required.

1.1.2 Challenges of higher frequency bands

Since higher frequency bands are being used for mobile communications for the first time in 5G, higher frequency bands would only be used for limited scenarios in the initial deployment of 5G, e.g., in small cell deployments or for fixed wireless access. In 5G and beyond, in order

to enhance better the benefits offered by the higher frequency bands, there will be a need to improve further the utilization of these bands by enabling their use over various scenarios including wide area coverage, Non Line-Of-Sight (NLOS), and high mobility. Furthermore, 6G may require a combination of multiple requirements. For example, the high frequency band needs to support eMBB and URLLC at the same time. Then, although high frequency bands are attracting attention as an approach to achieve eMBB in 5G, it may be necessary to have the capability to achieve URLLC in 6G. Main impediments of higher frequency bands propagation are higher path loss due to high carrier frequency, reduced scattering which reduces the available diversity and space-multiplexing gain, atmospheric attenuation and blockage by obstacles (e.g. buildings, vehicles, and human body). In addition, the effect of noise power is more pronounced due to the usage of larger bandwidths.

1.1.2.1 Path loss

The free space path loss is dependent on the carrier frequency f_c. Letting c and d be the speed of light and distance respectively, the path loss in free space is expressed as $L_{fs} = 10\log\frac{4\pi}{c} + 20\log d + 20\log f_c$ (dB). Hence, if the carrier frequency f_c is increased tenfold, the propagation loss increases by 20dB. On the other hand, the relationship between antenna gain G and carrier frequency f_c is expressed as $G = 10\log\frac{\eta\pi^2}{c^2} + 20\log D + 20\log f_c$ (dB). Here, D and η mean antenna aperture and efficiency, respectively. To obtain the same antenna gain G, the antenna size D can be reduced as f_c is increased. If D is constant, the antenna gain G can cancel the effect of path loss L_{fs}. On the contrary, keeping the antenna aperture constant at both ends will surprisingly reduce the free path loss with $20\log f_c$ (dB). Obtaining high gain with a large antenna aperture results in narrow beamforming. Therefore, beam control is important in higher frequency bands.

1.1.2.2 Blockage

Since higher frequency bands suffer less diffraction than the microwave, it makes them susceptible to blockage. The characteristic of such bands causes a large performance difference according to the lack and existence of Line-Of-Sight (LOS). As already mentioned, higher frequency bands require the use of beamforming to compensate for path loss. However, it results in reduced scattering. It is also a factor that increases the effect of blockage. Thus, the connection set will shift from being usable to unusable based on the presence of blockages.

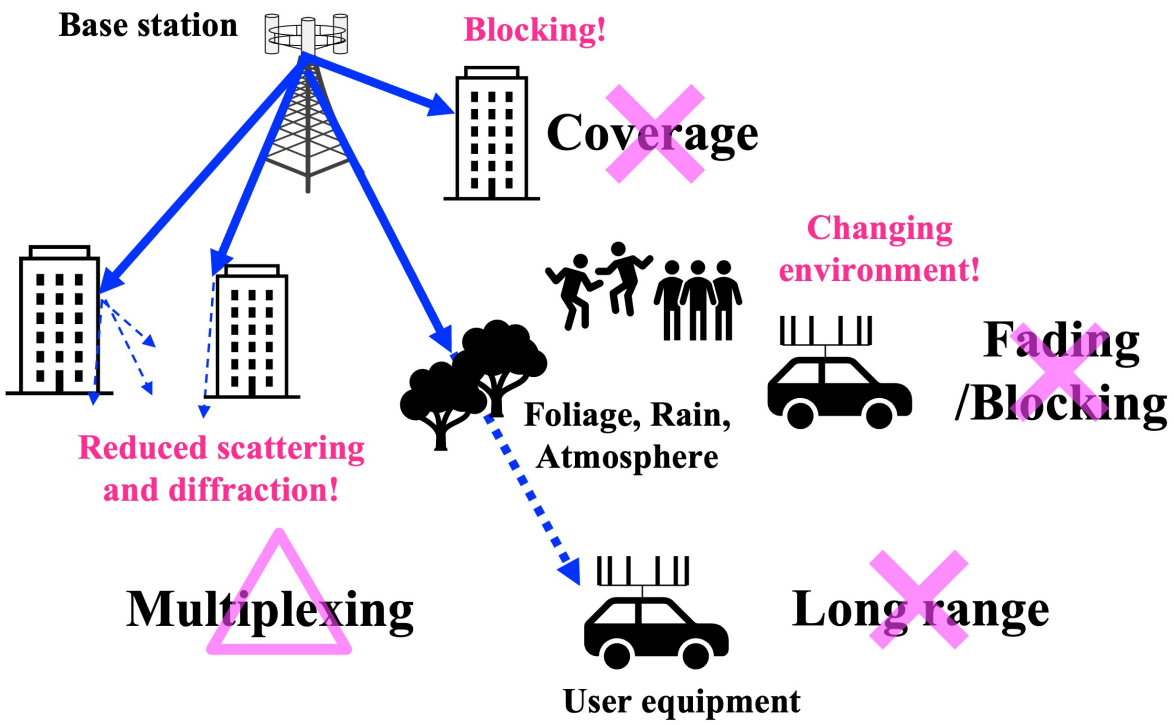

Figure 1.1 Challenges in higher frequency bands

This will result in a large scale drawback that cannot be bypassed with small scale diversity countermeasures.

1.1.2.3 Rain attenuation and oxygen absorption

For mobile communications utilizing higher frequency bands, rain, foliage, and atmospheric absorption may also be an impediment that cannot be ignored. Atmospheric attenuation due to oxygen absorption or heavy rain can be on the order of 10-20 dB/km. For example, in the 60-GHz band, the absorption due to air and rain is notable, especially the 15 dB/km oxygen absorption [8]. Hence, they are a major degradation in long-range communications using higher frequency bands. However, if we assume application to small cells, the effects are mitigated. These effects are summarized in Table 1.1. It can be noticed that the 28 GHz and 38 GHz bands at the range of 200 m suffer from low rain attenuation and oxygen absorption, while their effect is significant in the 60 GHz and 73 GHz bands.

Table 1.1 Rain attenuation and oxygen absorption of mmWave bands [8]

Frequency band	Rain attenuation @200 m		Oxygen absorption
	5 mm/h	25 mm/h	@200m
28 GHz	0.18 dB	0.9 dB	0.04 dB
38 GHz	0.26 dB	1.4 dB	0.03 dB
60 GHz	0.44 dB	2 dB	3.2 dB
73 GHz	0.6 dB	2.4 dB	0.09 dB

1.2 Research objective and approach

Assuming that traffic will continue to increase in the future, we will have to utilize higher frequency bands. However, due to the issues of radio wave characteristics and equipment costs already mentioned, there is concern that millimeter waves will be difficult to spread in mobile communication systems. Therefore, as the ultimate goal of this research, we aim to apply the millimeter wave band to any place and situation. As the first step, it is necessary to improve performance in the environment shown in Figure 1.2.

The purpose is to solve the problems in mmWave bands described in the previous sections and to improve the performance in mobile communication systems. This study firstly verifies the potential of applying mmWave bands to mobile communications. We build a mmWave communication system and verify its performance in several scenarios. The purpose is to experimentally clarify the potential and the issues of mmWave bands.

Next, redundant radio resource controls as an approach to solve the clarified issues are studied. Radio resources include space, time, and frequency. First, we focus on spatial resources. Multiple communication paths can be generated by spatially separating transmission and reception using beamforming, which is a prerequisite for mmWave bands. However, it is difficult for the transmitter to flexibly make communication paths because the radio waves tend to propagate straighter as the frequency increases. Therefore, we aim to make it possible to artificially generate communication paths by utilizing relay solutions, such as analog repeater. If there are multiple communication paths between transmitter and receiver, the effect of blockage can be alleviated and the effect of spatial multiplexing can be improved. In addition, the utilization of wireless relay solutions can amplify the power of radio wave and mitigate the received power degradation caused by path loss and atmospheric attenuation.

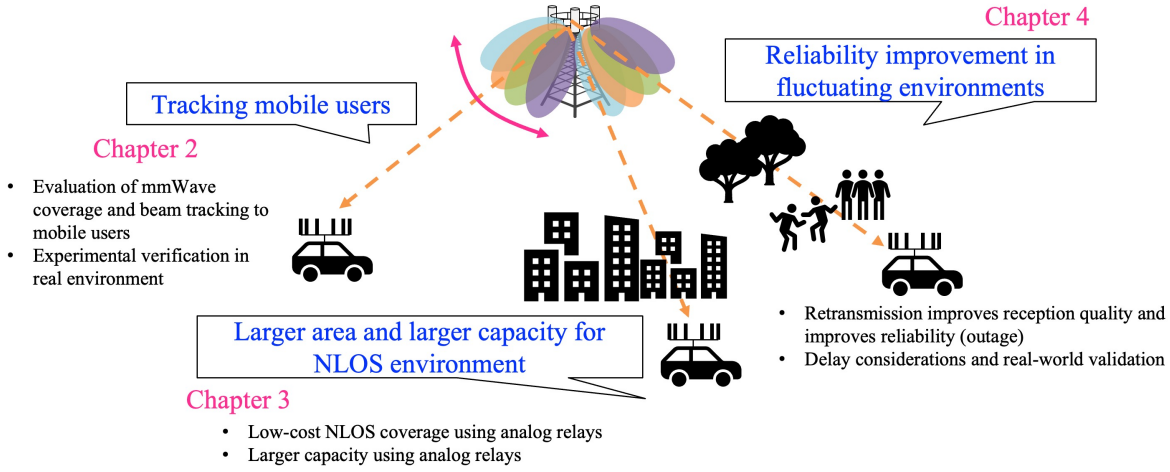

Figure 1.2 Overall picture of this research

Furthermore, time resource redundancy is also studied. Time resource redundancy means retransmission control in wireless communication systems. This approach is particularly suitable for use cases where even a little improvement in wireless communication quality is desired, such as URLLC. Future radio access is expected to require URLLC requirements even in mmWave bands. Therefore, radio frame design is studied to achieve the URLLC requirements. In retransmission control, gain can be obtained by transmitting multiple same signals, but there is a trade-off with communication delay. A radio frame considering the trade-off is proposed.

1.3 Related works

1.3.1 Applicability of millimeter waves to mobile communications

Some studies on mmWave propagation models and outdoor experiments have been conducted [11, 12, 13, 14, 15, 16]. In [11, 12, 13], radio propagation models were proposed based on experiments. In [11], 28-GHz and 38-GHz path-loss models based on measurements were presented. Outdoor experiments using mmWaves were introduced in [14,15,16]. The throughput performance made possible by using the 28-GHz band was verified in [14] and [15]. The mobility performance was also investigated in [14]. Performance in the 70-GHz band in an

outdoor experiment was evaluated in [16].

The above-mentioned studies target several hundred meters as the radius of mmWave coverage area; however, no experiments on long-distance transmission and mobility have been reported. Compared to the frequency bands evaluated in above studies, few experiments have investigated transmission performance in the 39-GHz band [17]. In [17], an outdoor experiment utilizing the 39-GHz band was conducted. However, the transmission distance was limited to 150 m, and the throughput was megabit-per-second class with 2 stream transmission. Moreover, mobility was not evaluated.

1.3.2 Utilization of relay solutions for space-resource redundancy

As a technical field for enhancing the potential of communication systems, the concept of controllable radio environments is attracting attention [31, 32]. This concept assumes a large number of relay devices to control the radio environment. There are several technologies for wireless relay. The Decode-and-Forward (DF) relay method is one of the typical methods, and it has been discussed as Integrated Access and Backhaul (IAB) in the standardization of the 3GPP Release 16 [33]. The DF relay can reduce noise and flexibly control radio resources by its decoding and re-encoding operations. However, this operation causes delay due to signal processing on Relay Nodes (RNs). Furthermore, since the cost is higher than other relay methods, it is not suitable for deploying large number of RNs. Reconfigurable Intelligent Surface (RIS), is a reflector that can switch the reflection direction of radio waves using meta-surface technologies, is also a remarkable solution [34, 35][9, 10]. However, RIS extends coverage by forming extremely sharp beams instead of amplifying signal power, so it is not easy to apply high mobility scenarios such as V2X. Therefore, we focus on Amplifier-and-Forward (AF) relay method that is easier to implement. The latest development of AF relay has been discussed in 3GPP Release 18 [36]. It is termed as a smart repeater that consists of a repeater with beamforming abilities. Radio environments can be controlled by spatially distributing RNs and operating them dynamically [37]. In [38], enhancement of single-user MIMO utilizing a massive AF relay with beamforming, which is called as massive analog-relay MIMO, is proposed. However, a control method in a system with multiple analog-relays has not been considered in these studies.

1.3.3 Radio frame design for time-resource redundancy

Time resource redundancy corresponds to retransmission control in wireless communication systems. A representative retransmission method is Hybrid Automatic ReQuest (HARQ) which is categorized in acknowledge/negative acknowledge (ACK/NACK)-based (A/N-based) retransmission. The transmitter decides whether or not to resend the same signal again based on ACK or NACK feedback from the receiver. However, this redundant method causes longer latency. With HARQ control in the downlink (DL) transmission, the set of user equipment (UE) attempts to receive data on the Physical Downlink Shared Channel (PDSCH). The UE transmits the decoding result as a HARQ feedback signal, such as ACK or NACK, in an uplink (UL) subframe. Since Frequency Division Duplex (FDD) allows transmission and reception in any subframe, the HARQ feedback signal for data received in the DL is sent uniformly 4 ms later in the UL subframe. In contrast, since TDD has constraints on the timing, the interval between transmission and its HARQ feedback becomes 4 ms or more. Therefore, HARQ causes a longer latency if the channel conditions are poor and retransmissions are needed, especially in TDD. Unfortunately, TDD is recommended for high frequency bands in 5G and beyond. To address this problem, ACK/NACK-less (A/N-less) retransmission was proposed in [61] and [62]. Since this method sends the repetition signals even before the ACK or NACK signal is received, it is possible to improve the packet success probability and to suppress the user-plane latency. The above-mentioned studies are concept-level proposals or estimations based on computer simulations.

To reduce the increase in packet transmission delay due to time resource redundancy, an additional approach is needed to be taken in the design of the frame structure. For example, a mini slot based on the LTE-Advanced frame structure [56, 57] and a wider subcarrier spacing [58, 59] with NR have been proposed. The mini-slot design applies a shorter slot length than that for LTE-Advanced with the same subcarrier spacing. It was shown that the mini slot with one Orthogonal Frequency Division Multiplexing (OFDM) symbol per slot can reduce the user-plane latency [56]. On the other hand, wider subcarrier spacing can also be used to reduce the user-plane latency even if the number of OFDM symbols is the same as that for LTE-Advanced because it can shorten the OFDM symbol length. In [58], the authors proposed reducing the latency using the subcarrier spacing of 312.5 kHz in an ultra-dense small cell network. In [59], the latency using the subcarrier spacing of 60 kHz was estimated. In the 3GPP standards, several subcarrier spacings (15, 30, 60 and 120 kHz) are supported in the NR specification [60].

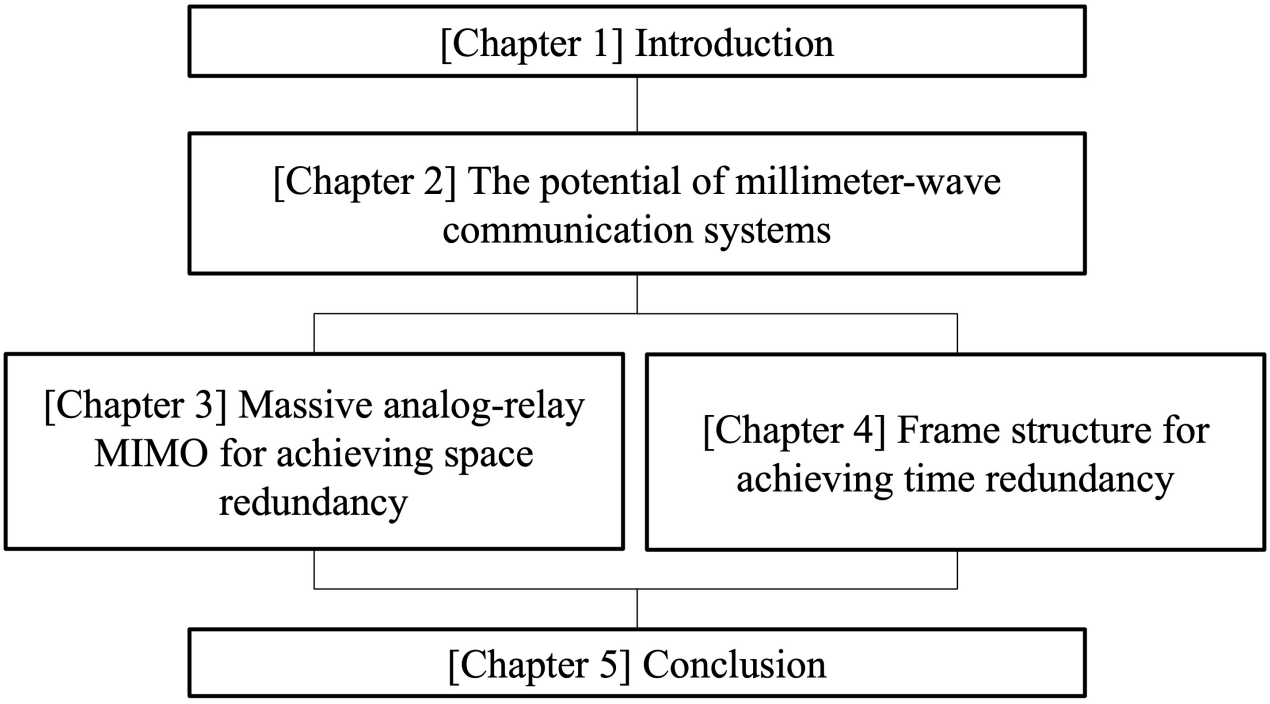

Figure 1.3 Thesis structure

1.4 Outline of this thesis

The rest of the thesis is organized, as shown in Figure 1.3.

Chapter 2 introduces the design of mmWave communication system and the experiments using the design equipment. mmWave will bring great benefit to us. However, considering the characteristics of radio waves, it is a significant challenge to apply mmWave to mobile communications. In this chapter, experiment results clarify that how much benefits and difficulties mmWave have. Chapter 3 provides the improvement of mmWave communications by spatial resource redundancy. Massive analog-relay MIMO is proposed as an approach to spatial redundancy. Multiple relay nodes can newly generate communication paths. It can reduce the effects of large pass loss and less scattering, and improve the performance of mmWave communications. In this chapter, a simple relay beam control method is proposed and discussed its effect. Chapter 4 provides an approach that focuses on time resource redundancy. Time resource redundancy causes communication delays. Therefore, we propose the radio frame that takes into account time resource redundancy and delay. Adopting URLLC

requirement as an evaluation indicator, the effect of time resource redundancy is evaluated through experiments in this chapter. Finally, Chapter 5 concludes the thesis.

The results of Chapter 2 are published in

- M. Iwabuchi, A. Benjebbour, Y. Kishiyama, G. Ren, C. Tang, T. Tian, L. Gu, Y. Cui, and T. Takada, Outdoor Experiments on Long-Range and Mobile Communications Using 39-GHz Band for 5G and Beyond, IEICE transaction on communications, Vol. E102-B, No. 8, pp. 1437-1446, Aug., 2019.
- A. Benjebbour, M. Iwabuchi, Y. Kishiyama, W. Guangjian, L. Gu, Y. Cui, and T. Takada, "Outdoor Experimental Trials of Long Range Mobile Communications Using 39 GHz", 2018 IEEE 87th Vehicular Technology Conference (VTC Spring).

The results of Chapter 3 are published in

- K. Sakaguchi, T. Yoneda, M. Iwabuchi, and T. Murakami, Mmwave massive analog-relay MIMO, ITU J-FET,Vol. 2, Issue 6, pp. 43-55, 2021.
- M. Iwabuchi, Y. Ramamoorthi, and K. Sakaguchi, User-driven relay beamforming in massive analog relay MIMO, https://doi.org/10.3390/s23021034, MDPI Sensors, 23(2), 1034; Jan. 2023.

The results of Chapter 4 are published in

- M. Iwabuchi, A. Benjebbour, Y. Kishiyama, G. Ren, C. Tang, T. Tian, L. Gu, Y. Cui, and T. Takada, 5G Experimental Trials for Ultra-Reliable and Low Latency Communications Using New Frame Structure, IEICE transaction on communications, Vol. E102-B, No. 2, pp.381-390, Feb., 2019.
- M. Iwabuchi, A. Benjebbour, Y. Kishiyama, G. Ren, C. Tang, T. Tian, L. Gu, T. Takada, and T. Kashima, "5G Field Experimental Trials on URLLC Using New Frame Structure", 2017 IEEE Globecom Workshops.
- M. Iwabuchi, A. Benjebbour, Y. Kishiyama, G. Ren, C. Tang, T. Tian, L. Gu, T. Takada, and Y. Cui, "Evaluation of Coverage and Mobility for URLLC via Outdoor Experimental Trials", 2018 IEEE 87th Vehicular Technology Conference (VTC Spring) Workshops.

Chapter 2

The potential of millimeter-wave communication systems

2.1 Motivation

In this chapter, in order to verify the potential of mmWave bands with higher throughput, we selected the 39-GHz band, which is a candidate frequency band for 5G [10]. The benefit from using mmWave bands for mobile communications is the capability to use a bandwidth of several hundred megahertz or greater than 1 GHz, which can boost both the data rate and capacity. However, one challenge in designing cellular networks in the mmWave bands is coverage. It is generally understood that mmWaves can only be used for small cells and limited coverage. This is because of the increased path loss of mmWave bands. Thus, for the mmWave, coverage enhancement is an important challenge. We expect that mmWave can support not only small cells but also rural macro-cells. Since the cell radius of the rural macro-cell is defined as approximately 1 km [9], we aim to achieve the mmWave coverage of 1 km or more. Furthermore, 5G and beyond should achieve at least a performance level exceeding the 4G requirement. Therefore, for 5G and beyond, we target the DL data rate of 1 Gbit/s or more within the coverage instead of the peak DL data rate of 1 Gbit/s required in 4G. To compensate for the increased path loss, beamforming becomes one of the key technologies for mmWave communication systems [19]. One of the other issues to be clarified is whether it is possible to provide high data rates to a mobile user. Although beamforming is a premise in mmWave bands, the instantaneous coverage made by beamforming is narrow. It is difficult to provide communication to a mobile user without proper beam tracking. In this chap-

ter, a 39GHz-band transmission system is designed, and the performance is experimentally measured in the real field.

The rest of this chapter is organized as follows. Section 2.2 describes the concept and the main features adopted in the experiment including the antenna design and the radio interface design. Section 2.3 describes the configuration of the field experiments including descriptions of the experiment equipment and environment. Section 2.4 presents the results of the outdoor experiments. Finally, Section 2.5 concludes the paper.

2.2 Design of mmWave mobile communication system

To clarify the mmWave performance, a 39GHz band transmission system for mobile communications is constructed. Beamforming is a key technology in applying mmWave to mobile communications. In this section, the antenna structure, the beam tacking procedure and the radio frame structure for beam tracking are introduced.

2.2.1 Beamforming using lens antenna

To compensate for the path loss in the mmWave bands, a lens antenna, which provides a high beamforming gain with a compact antenna size [20, 21], is used in this experiment. The structure of the lens antenna is shown in Fig. 2.1. The structure is called an Analog Radio Unit (ARU). It has a flat shape and is constructed using metamaterials that have a specific distribution of dielectric constants [21]. A radio wave emitted from a port is incident to the metamaterial part. The incident radio waves passing through the metamaterial are subject to different phases depending on the dielectric constant of the incident point on the metamaterial part. As a result, the energy of the wave radiated from the metamaterial can be concentrated in a particular direction. In addition, we can easily control the beam direction by switching the emitting port when using multiple ports to emit the radio waves.

One ARU, which is used for the Base Station (BS) and Customer Premises Equipment (CPE) Type 1 in the experiment (introduced in more detail in Section 2.3), has 64 candidate beam-patterns with single polarization. The mapping of the beam indices is indicated in Fig. 2.2. The ARU has 8 candidate beams each in the horizontal and vertical directions. As shown in Fig. 2.1, the ARU has 4 Radio Frequency (RF) channels, and 1 RF channel supports 16 candidate beams. The envelope of the beam patterns is shown in Fig. 2.3 and 2.4. Fig. 2.3 shows the envelope of beam patterns in azimuth, and it is drawn with 8 beams

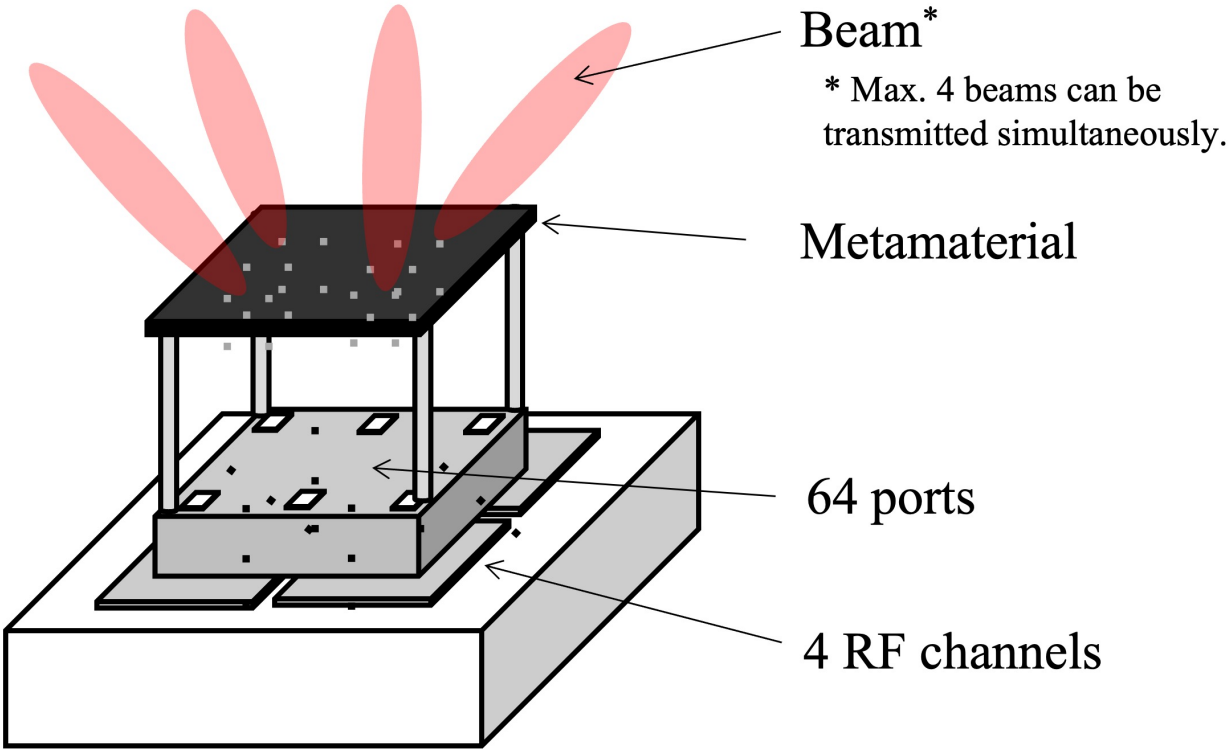

Figure 2.1 Structure of lens antenna

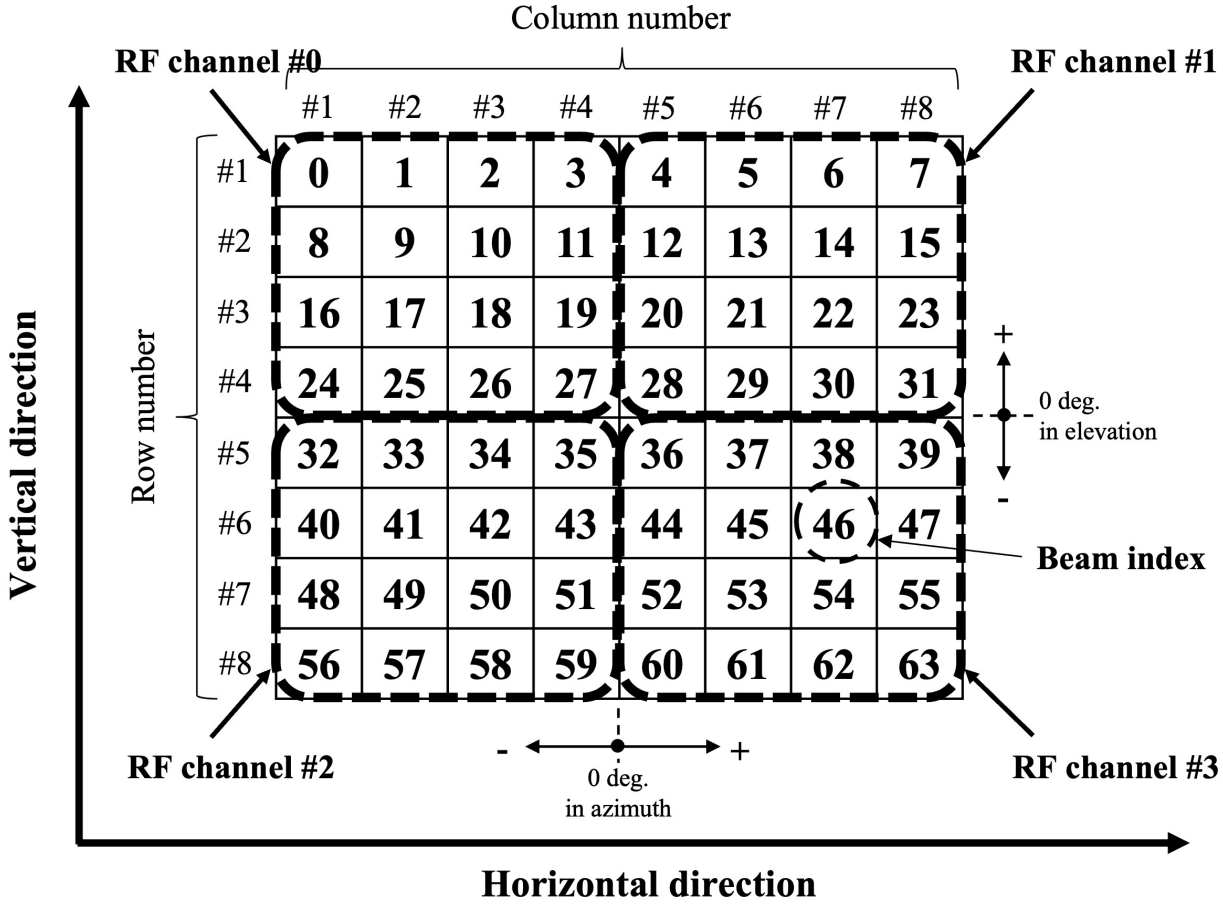

Figure 2.2 Mapping of beam indices (ARU for BS and CPE Type 1)

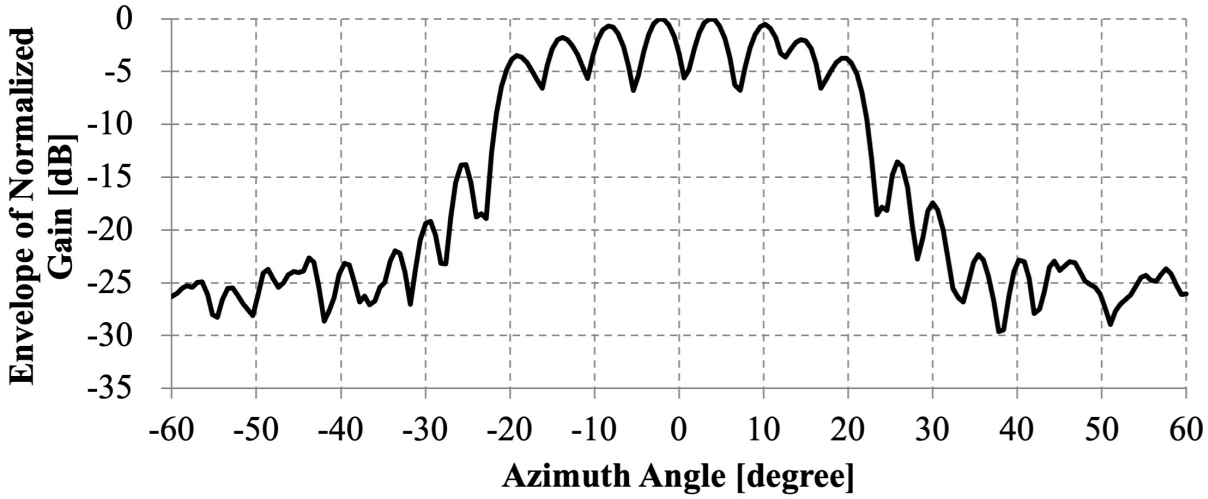

Figure 2.3 Beam pattern in azimuth (Row number #4)

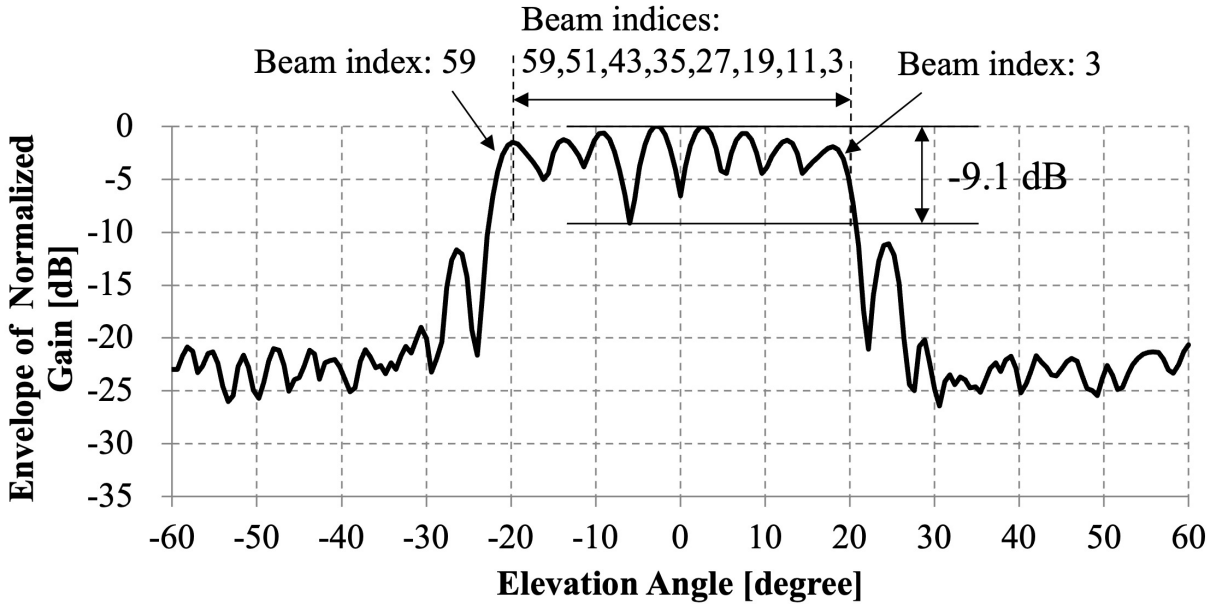

Figure 2.4 Beam pattern in elevation (Column number #4)

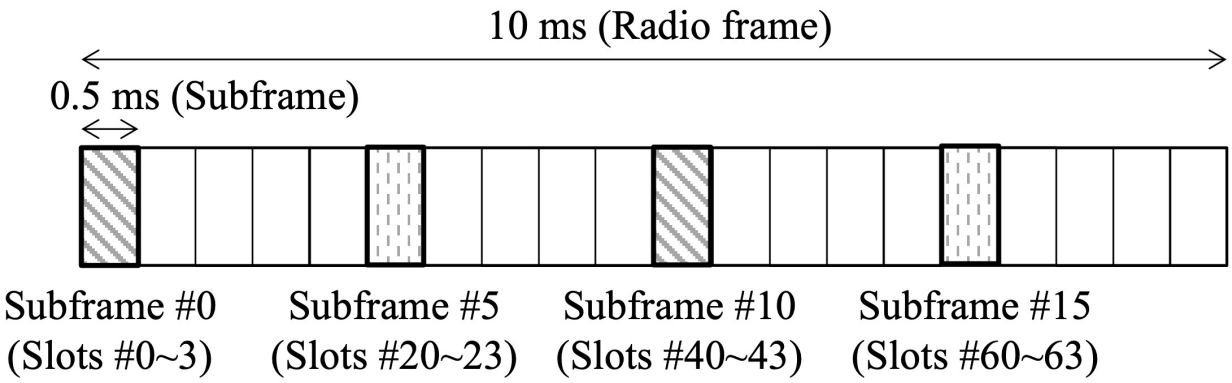

Figure 2.5 Frame structure for the 39-GHz system

with row number #4 shown in Fig. 2.2. Since the beamforming using the lens antenna is analog beamforming, there is a gain gap between the beam and the adjacent beams. The maximum gap is approximately 6.8 dB in Fig. 2.3. In Fig. 2.4, the envelope of beam patterns is generated using 8 beams with column number #4. The beam patterns also have a gain gap between beams, and the maximum gap is approximately 9.1 dB. The gain gap means that the antenna gain cannot be sufficiently obtained depending on the position of the set of UE. Note that the beam patterns of other row numbers and column numbers are almost the same as those in 2.3 and 2.4.

2.2.2 Frame structure

TDD based Orthogonal Frequency Division Multiple Access (OFDMA) is used as the multiple access scheme. The frame structure is designed to provide high capacity access service with mmWaves. In order to provide high capacity using the 39-GHz band, the frame structure must be designed to support beam searching and tracking. The employed radio frame structure is depicted in Fig. 2.5. The subcarrier spacing is 120 kHz, and has the slot length of 0.125 ms. A set of 4 slots is defined as 1 subframe in this paper, and the subframe length is 0.5 ms. Each 10-ms radio frame consists of 80 slots (20 subframes). The following five types of slots are used in the radio frame.

1. DL sweeping slot including synchronization signal, broadcast information, and Channel

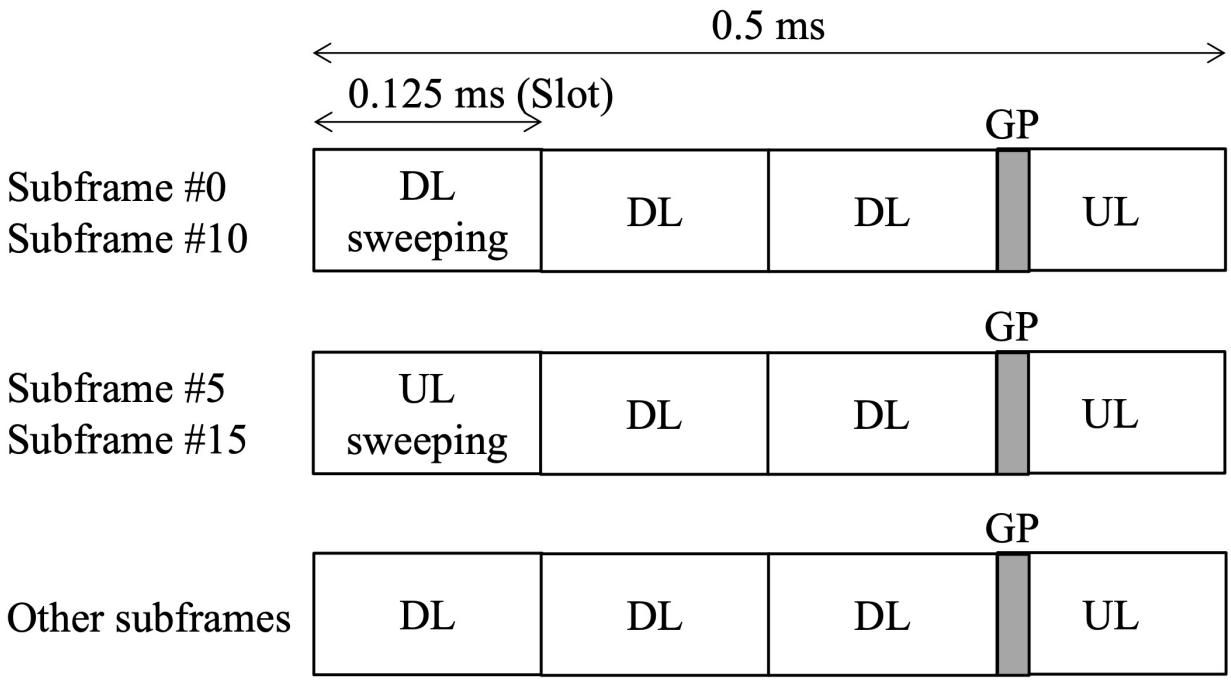

Figure 2.6 Subframe structure

State Information Reference Signal (CSI-RS) for beam detection, e.g., slot #0.

2. DL slot including control channel and DL data channel, e.g., slot #1.

3. DL slot including only DL data channel, e.g., slot #21.

4. Uplink (UL) sweeping slot including a preamble signal for random access and UL time synchronization, e.g., slot #20.

5. UL slot including a guard period (GP), UL data channel, and UL control channel, e.g., slot #3.

There are 3 types of subframes shown in Fig. 2.6. Subframes #0 and #10 include a DL sweeping slot, and subframes #5 and #15 include an UL sweeping slot. The other subframes have DL and UL slots.

2.2.3 Beamforming using multiple beam candidates

Differently from fixed wireless access, in mobile communications, the UE can be moving. Thus, it is important to follow the movement of the UE and to switch the beam direction dynamically to maintain a high received power level. To find the best beam pair between the BS and UE, a beam searching and tracking method is applied in the 39-GHz testbed. The beam searching and tracking method is shown in Fig. 2.7. The case of 1 ARU is described in this section. Even if multiple ARUs are used, each ARU operates in the same way.

To find the best beam pair between the BS and UE, the received power for each beam pair is measured. The measurement is conducted using the CSI-RS included in the DL sweeping slot shown in Fig. 2.6. On the UE side, four reception beams are set for the measurement and these beams are fixed during one radio frame. Then, one beam is selected for each RF channel. Sets of beam indices are listed in Table 1, and the list is based on beam indices shown in Fig. 2.2. For example, beam set #0 consists of beam index #0, #4, #32, and #36 and is first selected on the UE-side ARU. Similarly, the BS-side ARU selects a beam set, e.g., beam set #0, and the BS transmits a CSI-RS over the selected 4 beams. After transmitting the CSI-RS, the BS selects a different set of 4 beams, e.g., beam set #1, and transmits the next CSI-RS over the beam set. Since the DL sweeping slot has 12 CSI-RSs and the ARU can transmit 4 beams simultaneously, the quality of beam pairs between 48 transmission beams and 4 reception beams can be measured using 1 DL sweeping slot. After completing the

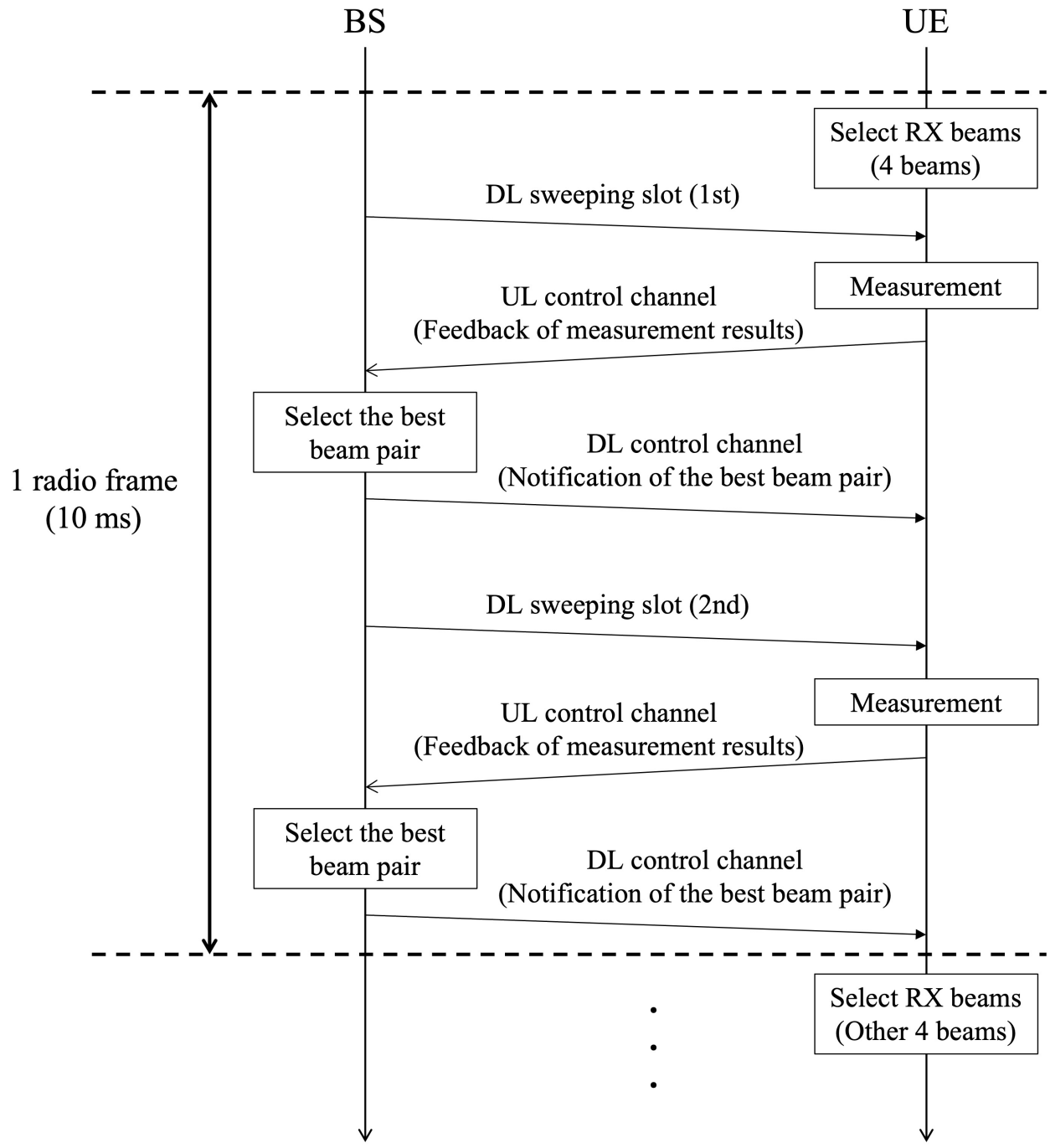

Figure 2.7 Flowchart of beam searching and tracking method

Table 2.1 Set of beam indices for beam searching

Beam Set #	Set of Beam Indices
#0	{ #0, #4, #32, #36 }
#1	{ #1, #5, #33, #37 }
#2	{ #2, #6, #34, #38 }
#3	{ #3, #7, #35, #39 }
#4	{ #8, #12, #40, #44 }
#5	{ #9, #13, #41, #45 }
#6	{ #10, #14, #42, #46 }
#7	{ #11, #15, #43, #47 }
#8	{ #16, #20, #48, #52 }
#9	{ #17, #21, #49, #53 }
#10	{ #18, #22, #50, #54 }
#11	{ #19, #23, #51, #55 }
#12	{ #24, #28, #56, #60 }
#13	{ #25, #29, #57, #61 }
#14	{ #26, #30, #58, #62 }
#15	{ #27, #31, #59, #63 }

measurement, the results are sent from the UE to the BS. The BS selects the best beam pair from the results for the past 160 ms and notifies the UE of the selected beam pair. The best beam can be updated every 10 ms (1 radio frame).

Since 2 DL sweeping slots are included in 1 radio frame as shown in Fig. 2.5, the maximum number of beam pairs that can be measured is 96 transmission beams (= 48 transmission beams Œ 2 DL sweeping slots) and 4 reception beams within 1 radio frame. The equipment used in the experiments has 64 candidate beams, so it can measure the quality of the beam pairs between 64 transmission beams and 4 reception beams within 1 radio frame. On the other hand, since only 4 reception beams can be measured in 1 radio frame, 16 radio frames, namely 160 ms, are required to measure all beam pairs in the experiments.

2.2.4 Impact of beam searching

Considering mobile communication systems, the impact of beam search time on receiving gain is evaluated. The impact of beam search depends on communication distance, user velocity, and beam width. This evaluation clarifies how much gain loss occurs in what kind of situation. Figure 2.8 shows the evaluation model. The state where the user obtains the maximum beam gain is taken as the starting state, and the gain loss just before the beam search time elapses is calculated. Here, the user moves from the BS on a horizontal road at velocity v, and the shortest distance from the BS to the road is defined as D. The beam search time is expressed as T_s. Figure 2.9 shows the gain loss with respect to the distance D, and Figure 2.10 shows the gain loss with respect to the beam search time. Here, the half width of the beam is 6 degrees, which is the same as the antenna beam used in the experiment. As the beam search time increases, the loss increases in the area near the BS. In addition, even if the user velocity v increases, the gain loss will increase unless the distance D is increased. Therefore, it is necessary to design the T_s according to the area size of the BS and find ways to shorten T_s when the number of beam candidates increases. A related study is described in Chapter 3. In the experimental verification described in this chapter, since the gain loss caused by T_s is designed to be less than 1 dB, the impact of the beam search is small.

2.3 Experimental configuration

The experiment configuration is described in this section. The experiment parameters, the experiment equipment, and the experiment environment are presented in detail.

2.3.1 Experiment parameters

The parameters for the experiment are given in Table 2.2. The carrier frequency range is from 39.5 GHz to 40.9 GHz, and the system bandwidth is 1.4 GHz using 7 Component Carriers (CCs) where each CC has a 200-MHz bandwidth. The waveform is filtered OFDM, and the subcarrier spacing is 120 kHz. The Polar code and Low-Density-Parity-Check (LDPC) code are applied to the control channel and data channel, respectively. The data signal is modulated with QPSK, 16QAM, and 64QAM. Reference signals such as a demodulation reference signal and CSI-RS are modulated with QPSK. We tested the performance using 3 types of transmission modes (TMs). TM #1 communicates using only vertical polarization.

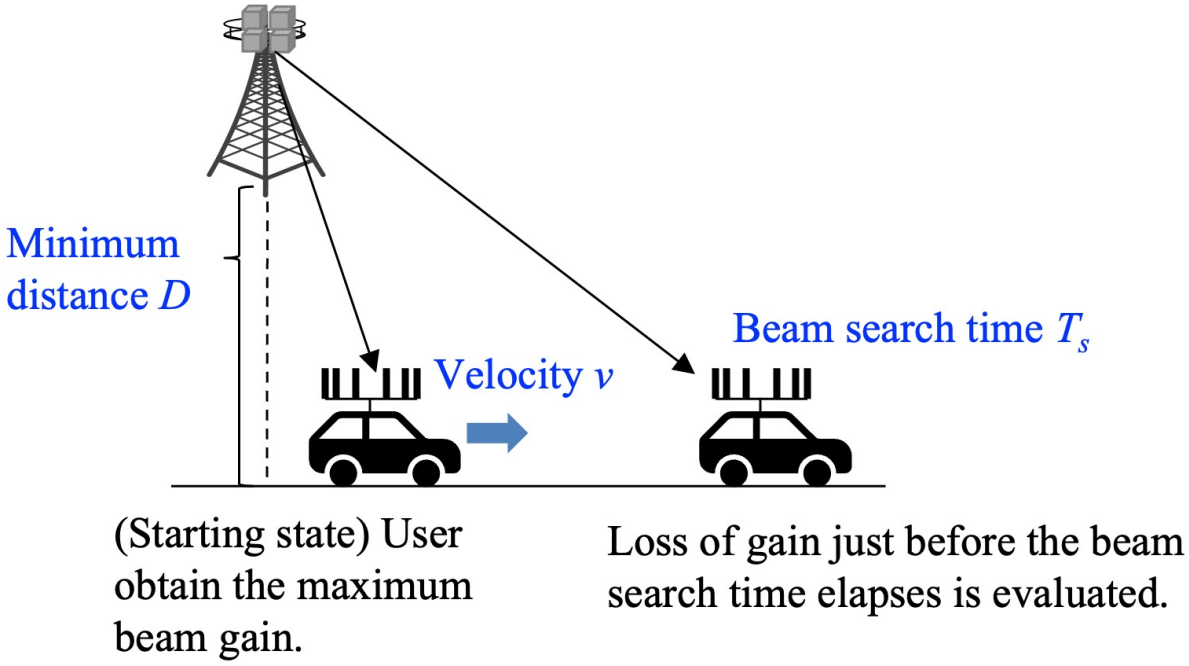

Figure 2.8 Model for evaluating the impact of beam searching

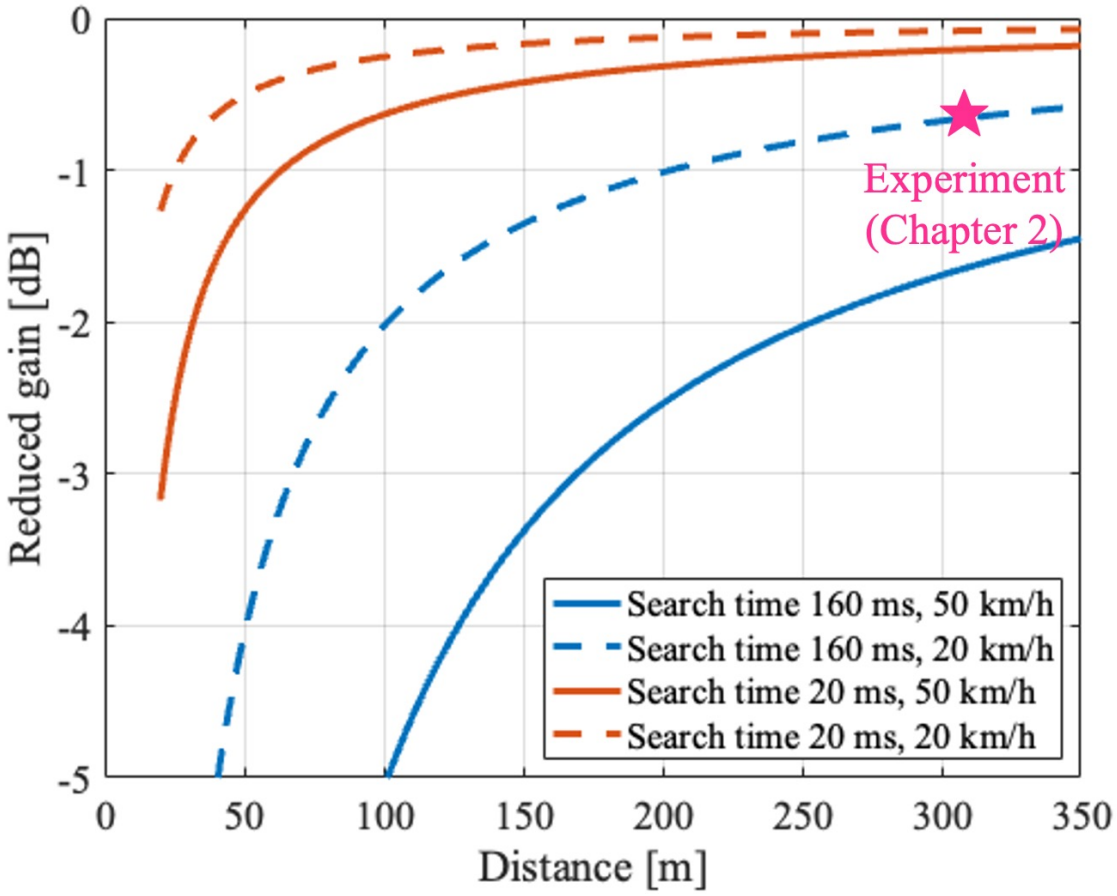

Figure 2.9 Relationship between gain loss and transmission distance

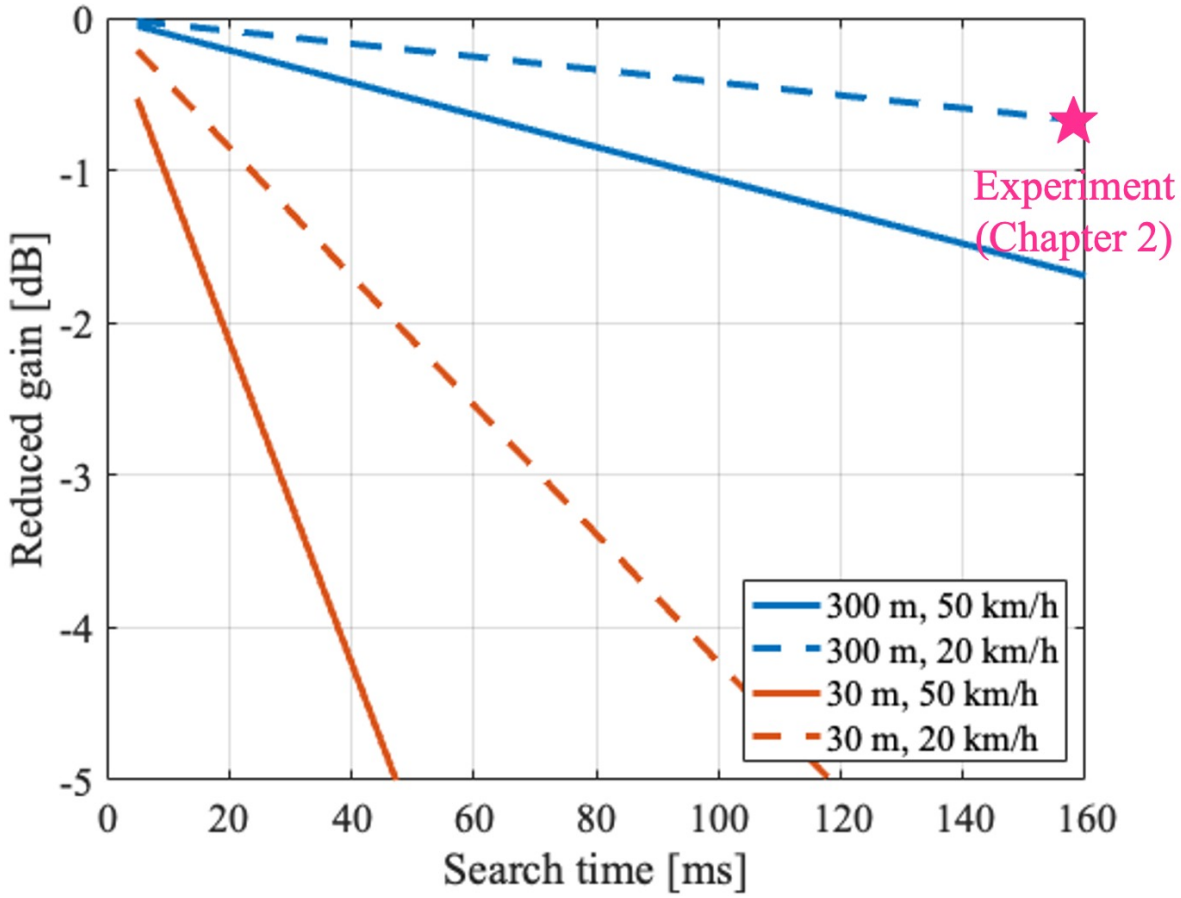

Figure 2.10 Relationship between gain loss and beam search time

Table 2.2 Experiment parameters

Parameter #	Value
Carrier frequency	39.5 - 40.9 GHz
System bandwidth	1.4 GHz
Component carrier bandwidth	200 MHz
Waveform	Filtered-OFDM
Subcarrier spacing	120 kHz
Number of subcarriers	1,656
Slot length	0.125 ms
OFDM symbols	14 symbols/slot
Cyclic prefix (CP) length	0.651 μs (1st, 8th OFDM symbols) 0.586 μs (Other OFDM symbols)
CP overhead	6.67 %
Guard period	70.8 μs
Channel coding	Polar code (Control channel) LDPC code (Data channel)
Transmission power	13 dBm/beam
Transmission mode (TM)	TM#1: 1 layer w/ single polarization TM#2: 1 layer w/ dual polarization TM#3: 2 layer w/ dual polarization
BS sector direction	North 0 deg.
BS antenna tilt	18.4 deg.

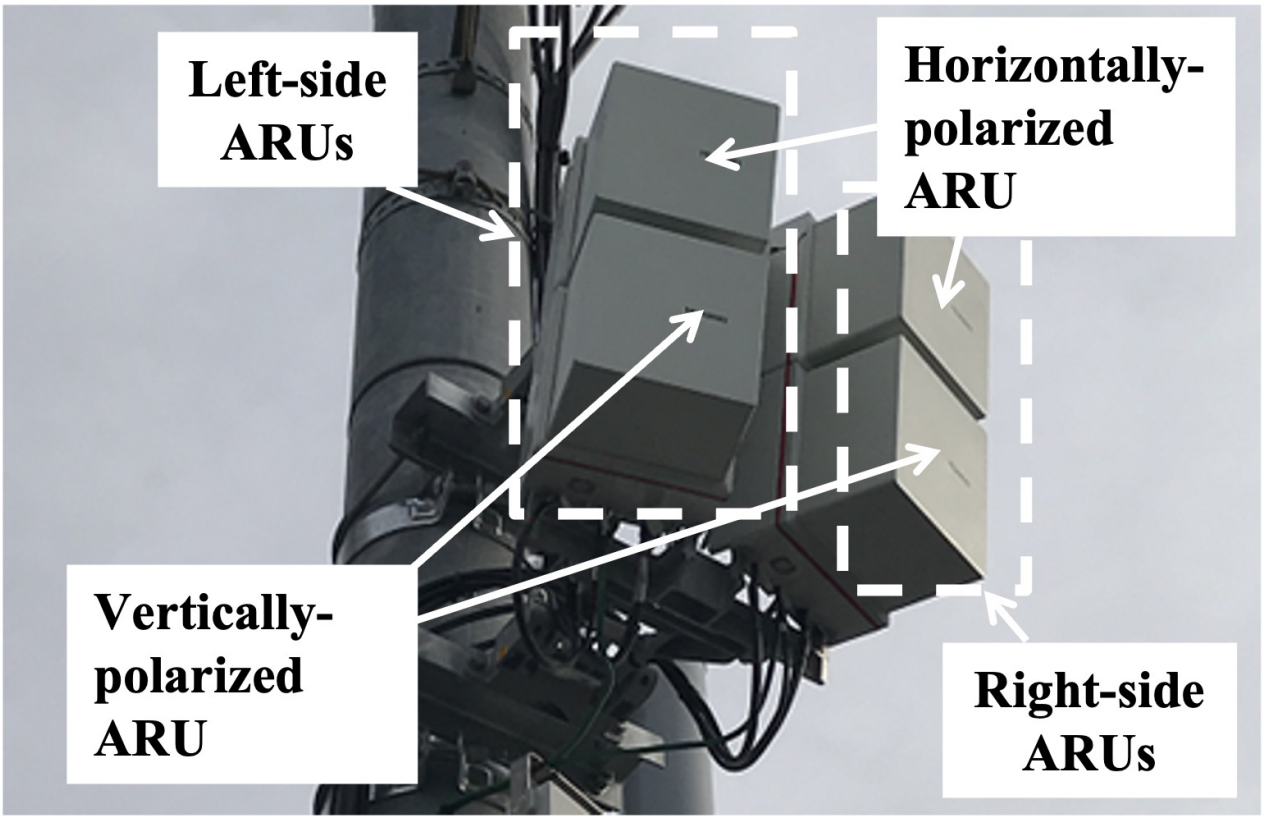

Figure 2.11 Base station

TM #2 uses horizontal and vertical polarizations but the number of MIMO layers is 1. Then, Space-Frequency Block Coding (SFBC) [22] is selected as the MIMO processing method. TM #3 also uses dual polarization and the number of MIMO layers is 2, which is different from TM #2. The processing method is Cyclic Delay Diversity (CDD) [23].

2.3.2 Experiment equipment

The testbed comprises 1 BS and up to 2 types of CPE, and is developed to confirm the coverage and mobility performance using mmWaves in the 39-GHz band. The BS and two types of CPE are shown in Fig. 2.11 and 2.12. Up to 4 ARUs can be used simultaneously at the BS as shown in Fig. 2.11. Each ARU contains a RF front-end and lens antenna. Each ARU can either be horizontally (H) polarized or vertically (V) polarized. An ARU consists of 4 RF channels. Each RF channel is in turn connected to a digital-analog converter and an analog-

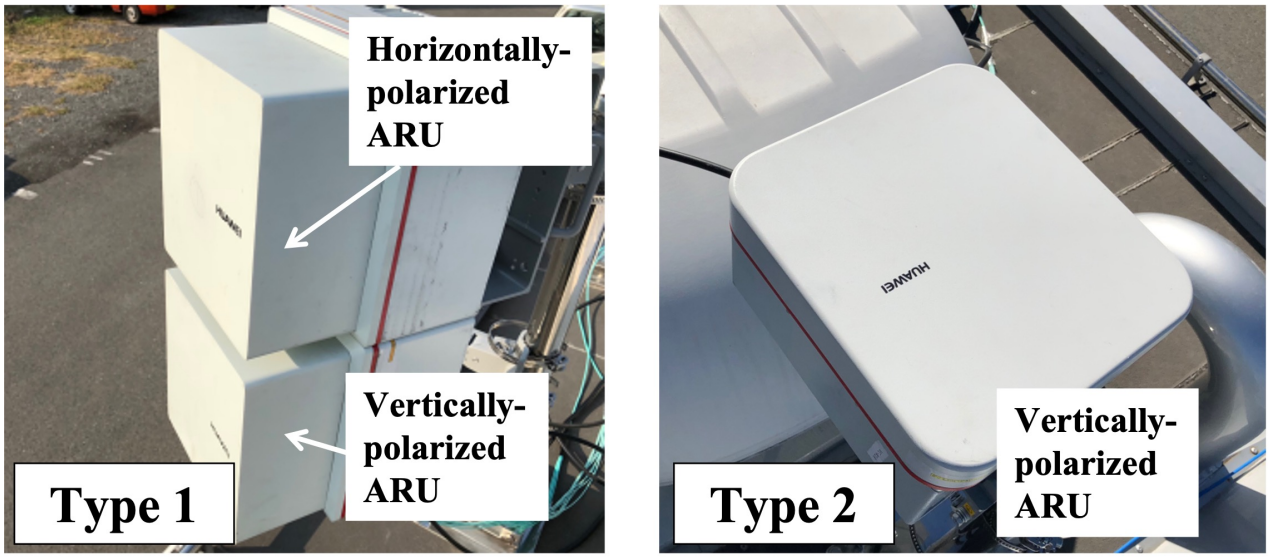

Figure 2.12 CPE Type 1 and Type 2

Table 2.3 Differences among BS, CPE Type 1 and CPE Type 2

Parameter	BS	CPE Type 1	CPE Type 2
Antenna type	Lens antenna		
Number of ARUs	4	2	1
Antenna gain	31 dBi		16 dBi
Polarization	Vertical / Horizontal		Vertical
Coverage per ARU	V: 40 deg. H: 40 deg.		V: 40 deg. H: 360 deg.
Number of beams	54		52

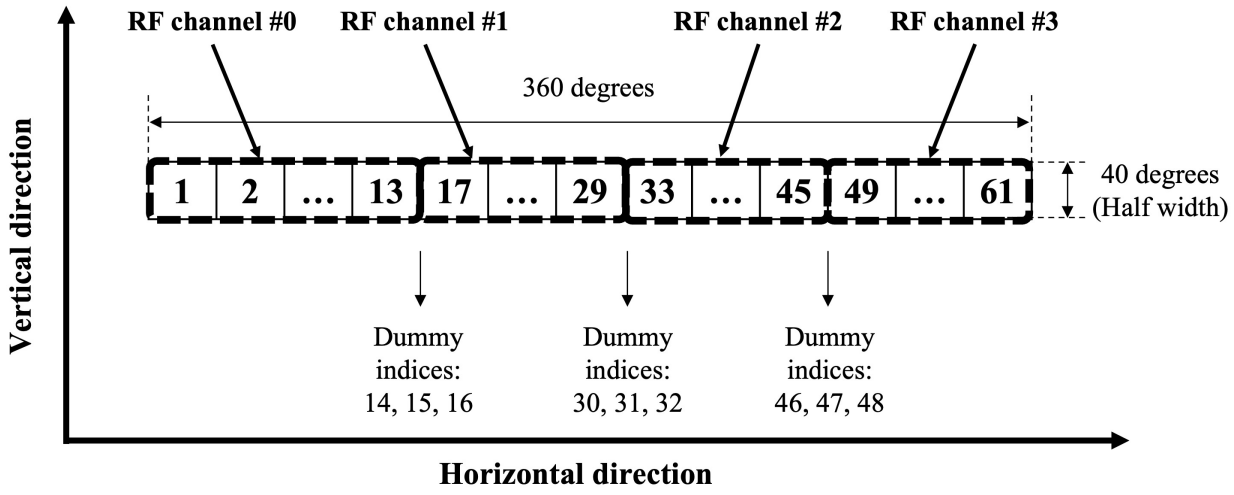

Figure 2.13 Mapping of beam indices (ARU for CPE Type 2)

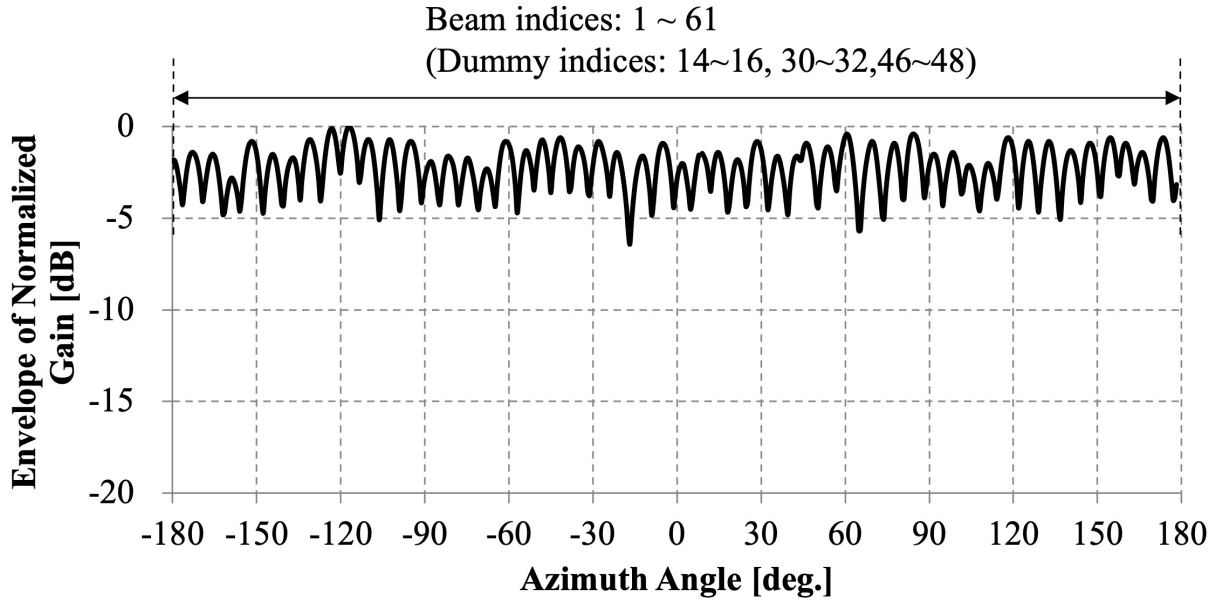

Figure 2.14 Beam pattern in azimuth (ARU for CPE Type 2)

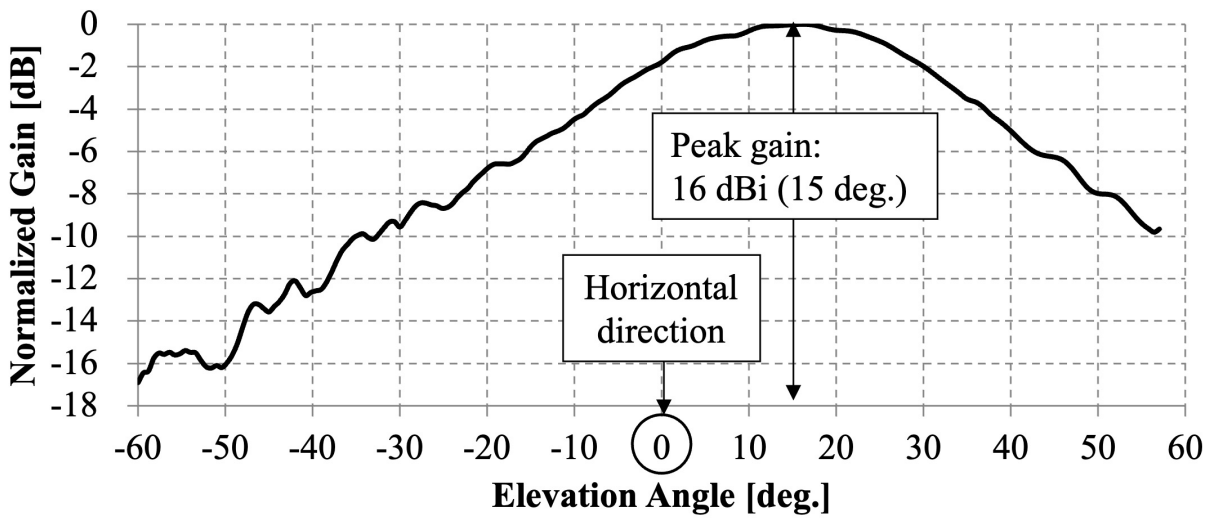

Figure 2.15 Beam pattern in elevation (ARU for CPE Type 2)

digital converter. As mentioned in Section 2.4, in order to find the best beam pair rapidly, each ARU uses 4 beams simultaneously in the beam searching and tracking process. On the other hand, only the best beam pair is used for the data transmission. The transmission power is 13 dBm per beam. Since the BS uses two ARUs with different polarizations in the same direction, it can support dual (V and H) polarization. Figure 2.12 shows the CPE used in the experiment. Two types of CPE with different types of antennas are used depending on the test scenario. CPE Type 1 comprises 2 ARUs with different polarizations and it supports dual polarization. However, since CPE Type 1 uses the same type of ARU as the BS, the coverage width is only 40 degrees in both V and H directions. CPE Type 2 shown in Fig. 2.12 uses another type of ARU and it can support the full range in the horizontal direction. However, since CPE Type 2 supports single (only V) polarization, it can only be applied to TM #1.

The differences among the BS, CPE Type 1, and CPE Type 2 are summarized in Table 2.3. CPE Type 1 has a high beamforming gain but a narrower beam sweeping range, and CPE Type 2 has a medium beamforming gain but a wider beam sweeping range, which is suitable for supporting mobility. Both the BS and CPE Type 1 have a beamforming gain of 31 dBi, while CPE Type 2 has a beamforming gain of 16 dBi. These beamforming gains

are designed to support long-range communications. For the ARU used for the BS and CPE Type 1, the mapping of beam indices and the beam pattern are already shown in Figs. 2.2, 2.3 and 2.4. For the ARU for CPE Type 2, the mapping of beam indices and the beam pattern is indicated in Figs. 2.13 and 2.14 and 2.15, respectively. The ARU for CPE Type 2 has 52 candidate beam patterns in the horizontal direction. In Fig. 2.15, the elevation angle of 0 degree means horizontal direction. All beams tilt upwards at 15 degrees for the vertical direction. Beam indices from #1 to #61 are allocated, but several beam indices are dummy and are not used. Differently from the ARU for the BS and CPE Type 1, one RF channel of the ARU for CPE Type 2 supports 14 beam patterns.

2.3.3 Experiment environment and configuration

The experiments are conducted in an urban area in Yokohama, Japan. The site is shown in Fig. 2.16. The BS is installed on the roof of a building. On the UE side, sets of CPE are established on the roof of the test vehicle as shown in Fig. 2.17. CPE Type 1 and Type 2 are installed in the front and back of the test vehicle, respectively. The BS and CPE heights are approximately 108 m and 3.5 m, respectively.

Measurements are conducted over measurement locations and the course is shown in Fig. 2.16, and measurement results are recorded every 1 second. Measurement locations A, B, C, D and E are LOS. The distances from the BS to each location are also shown in Fig. 2.16. The nearest location is location A and the distance is approximately 340 m, while the furthest location is location E at 1850 m. Only location F is NLOS, and buildings block the direct path from the BS to location F. At this location, a building (Building #1) exists behind the test vehicle. The distance is approximately 360 m from the BS site. The driving course for the mobility test is also shown in Fig. 2.16. The test course is basically LOS. At the end of the course, the test vehicle traverses between a building (Building #2) and a construction site. There is some construction equipment within the construction site. Fortunately, all measurements are conducted without rain.

2.4 Experiment results

The experimental results are presented in this section. Three kinds of experiments were conducted in the urban area of Yokohama, Japan. In the first experiment, we investigated long-distance performance in the 39-GHz band. The second experiment involved measuring

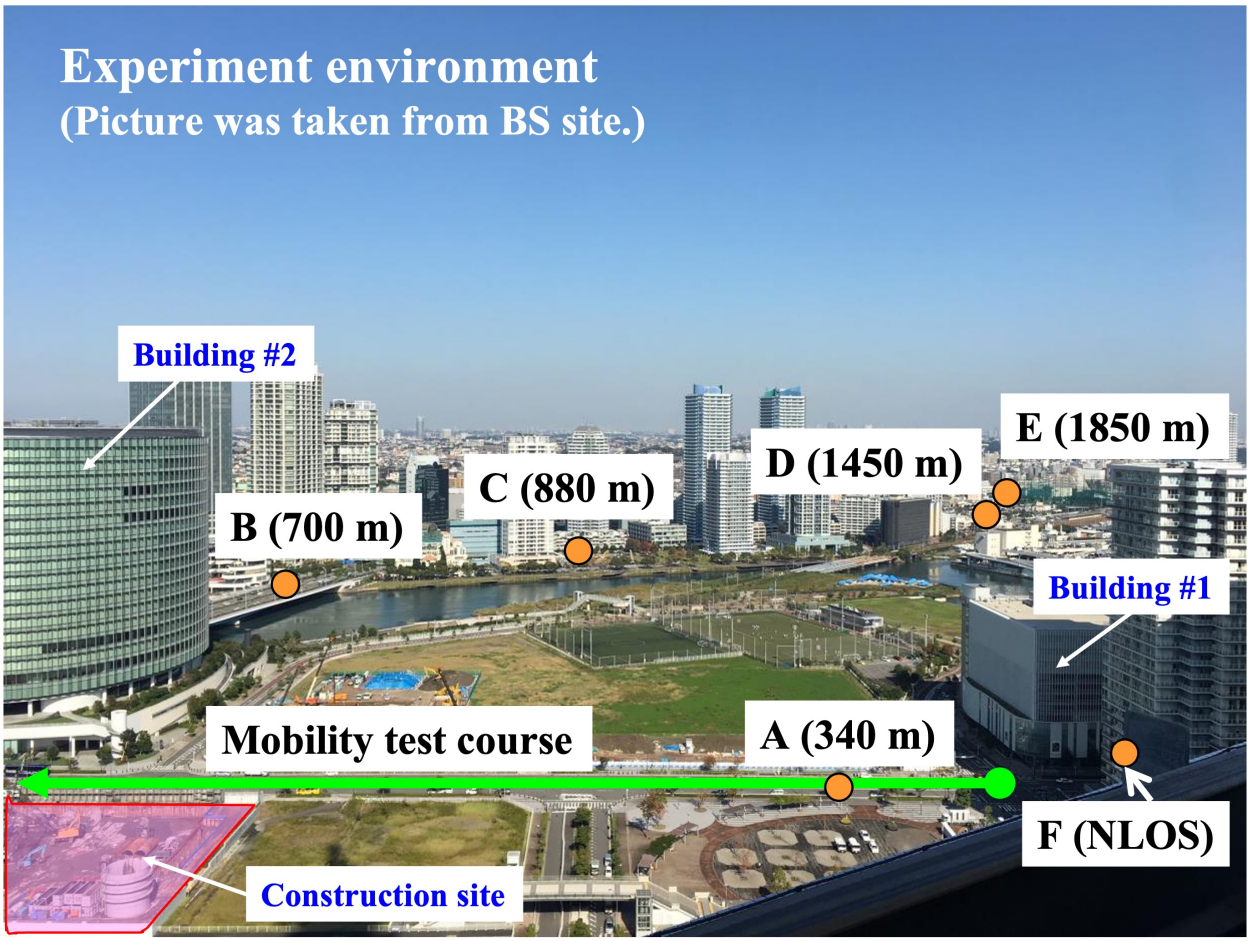

Figure 2.16 Experiment environment and measurement locations

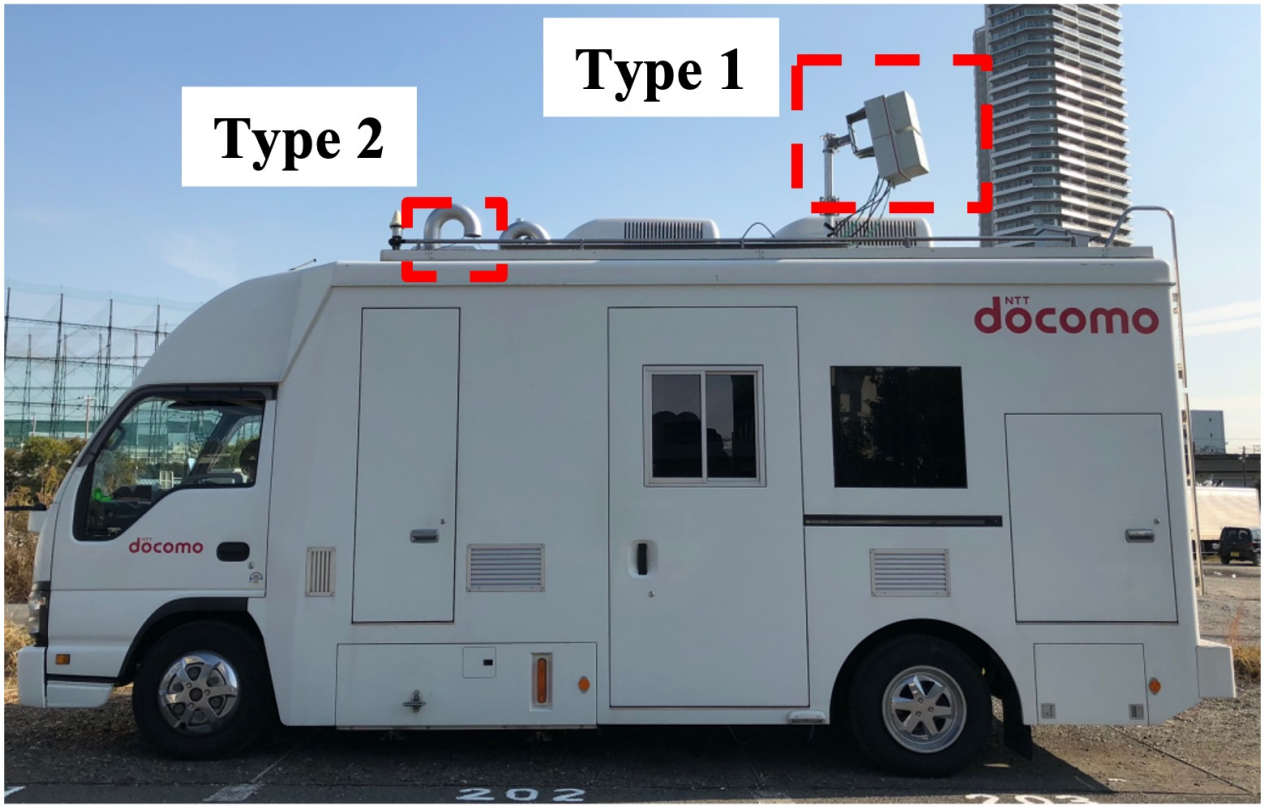

Figure 2.17 CPE installation on test vehicle (UE)

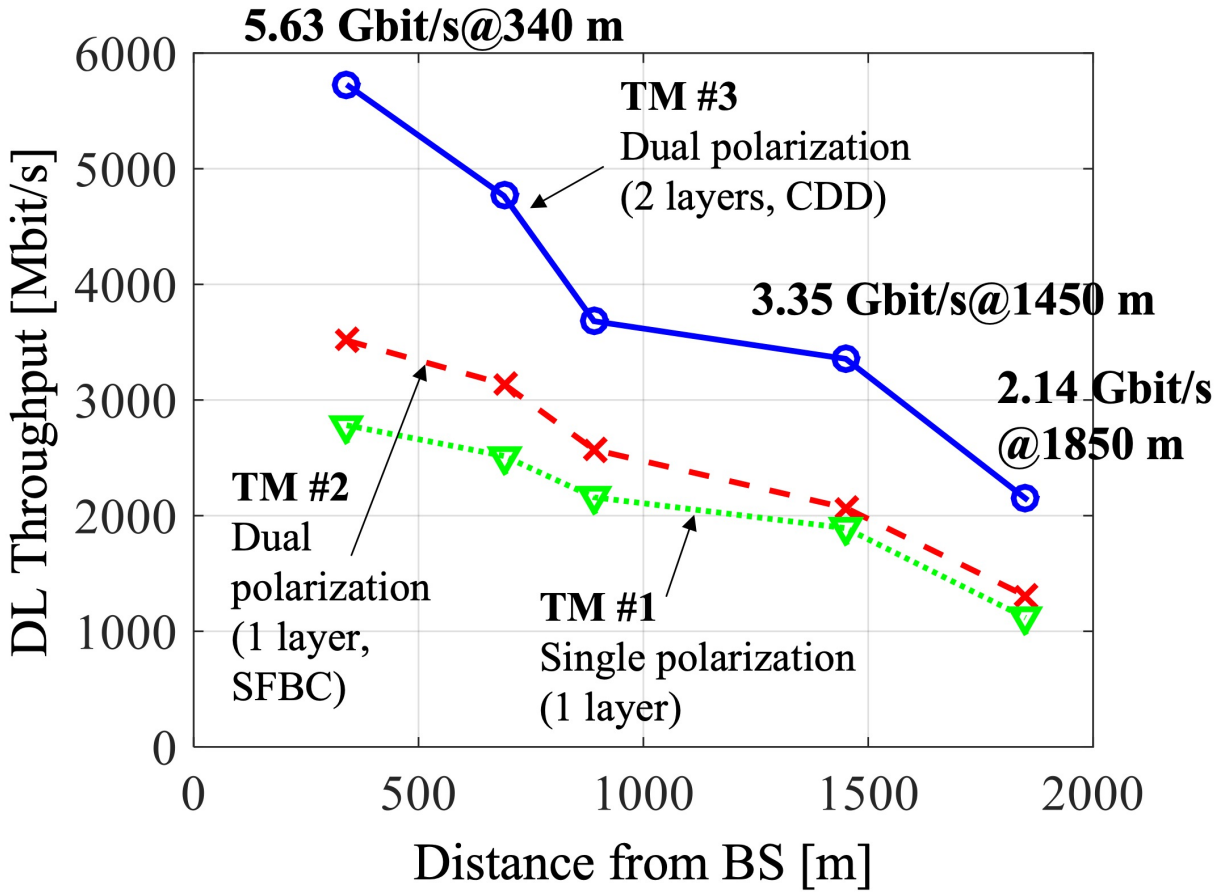

Figure 2.18 Downlink throughput at each location

the throughput at an NLOS location. In these two experiments, the UE is stationary. To evaluate the mobility performance in a large area, we conducted a mobility experiment as the third experiment.

2.4.1 Throughput performance at long distance

The objectives of these experiments are to investigate the throughput in the 39-GHz band at a long distance such as 1 km or more and to verify the throughput with pedestrian mobility at a long distance. These experiments are conducted using CPE Type 1.

Figure 2.18 shows the experimental results at different measurement locations with differ-

Table 2.4 Selected modulation and code rate R at each measurement location

	CC #0	CC #1	CC #2	CC #3	CC #4	CC #5	CC #6
A	64QAM (R=2/3)	64QAM (R=3/4)	64QAM (R=3/4)	64QAM (R=2/3)	64QAM (R=1/2)	16QAM (R=2/3)	16QAM (R=1/2)
B	64QAM (R=1/2)	64QAM (R=2/3)	64QAM (R=1/2)	16QAM (R=2/3)	16QAM (R=2/3)	16QAM (R=2/3)	QPSK (R=3/4)
C	16QAM (R=2/3)	64QAM (R=1/2)	16QAM (R=2/3)	16QAM (R=2/3)	16QAM (R=1/2)	QPSK (R=3/4)	QPSK (R=3/4)
D	16QAM (R=2/3)	16QAM (R=2/3)	16QAM (R=1/2)	16QAM (R=1/2)	16QAM (R=1/2)	QPSK (R=3/4)	QPSK (R=3/4)
E	QPSK (R=3/4)	QPSK (R=3/4)	QPSK (R=3/4)	QPSK (R=3/4)	QPSK (R=3/4)	QPSK (R=2/3)	QPSK (R=1/2)

ent distances from the BS site. At location A at the distance of 340 m, the throughput of 5.63 Gbit/s is achieved with TM #3 (as defined in Table 2.2). This result represents the maximum throughput in the experiment. At location D at 1450 km from the BS site, the throughput of 3.35 Gbit/s is achieved with 2-layer transmission (TM #3). Moreover, the throughput of 2.14 Gbit/s is achieved at the furthest point, location E, at 1850 m from the BS site. These results clearly show that we achieved our target of throughput exceeding 1 Gbit/s at over 1 km from the BS. Focusing on location B (700 m) and location C (880 m), the throughput sharply decreases compared to the other locations. The degradation is due to the change in the modulation and coding scheme. Table 2.4 shows the modulation and code rate mainly selected at each location and each CC. When comparing locations B and C, the modulation scheme is switched from 64QAM to 16QAM in CC #0 and #2, and it changes from 16QAM to QPSK in CC #5. Similarly, the throughput sharply decreases from location D (1450 m) to location E (1850 m). Also in this case, the modulation scheme is switched in several CCs. Figure 2.19 shows a comparison of the throughput estimated in advance and the measured throughput. For throughput estimation, the estimation formula of Equation 2.1 [27] and the MCS table specified in 5G were used. The required SNR was estimated from the evaluation results of SNR and BLER shown in the literature [26]. To estimate throughput, we assumed that EIRP of 41 dBm and noise figure of 9 dB. The 3GPP UMa model is applied [28]. The

Table 2.5 Varible in Equation 2.1 [27] and the values used for estimation

Variable	Explanation	Value for estimation
J	Number of component carriers (CCs)	7
$v_{Layers}^{(j)}$	Number of layers	1 or 2
$Q_m^{(j)}$	Modulation order in j-th CC	-
$f^{(j)}$	Scaling factor	1
R_{code}	Code rate	-
$N^{BW(j),\mu}$	Number of resource blocks	132
T_s^{μ}	Number of OFDM symbols per 1 ms	-
$OH^{(j)}$	Overhead	0.18
R_{DL}	DL ratio in TDD	0.7
R_{BLER}	Block error rate	0.1
μ	Index of OFDM subcarrier spacing	3 (120 kHz)

variables in Equation 2.1 and the values used for estimation are summarized in Table 2.5.

$$TP = 10^{-6} \sum_{j=1}^{J} \left(v_{Layers}^{(j)} Q_m^{(j)} f^{(j)} R_{code} \frac{N^{BW(j),\mu} 12}{T_s^{\mu}} (1 - OH^{(j)}) R_{DL} R_{BLER} \right) \tag{2.1}$$

Comparing the estimated value and the measured value, although the performance tend to be similar, it has an error. The error between the estimated value and the measured value is considered to be the received power difference between component carriers due to fading and RF performance, and the beam gain was not ideal.

At all the measurement locations under LOS conditions, TM #3 achieves at most double the throughput gain compared to the 1-layer transmission using single polarization (TM #1). This is because the V polarized signal of TM #1 and the V and H polarized signals of TM #3 are received with almost the same Signal-to-Interference-plus-Noise Ratio (SINR) as given in Table 2.6. The SINR was measured using a demodulation reference signal, and it includes interference between polarizations in TM #3. The throughput of the 1-layer transmission with dual polarization (TM #2) is higher than that for TM #1 due to the benefit from diversity. Using TM #3, the throughput is almost doubled compared to the TM #1 case for up to 1850 m from the BS site. This indicates that good isolation between the V and H polarizations is achieved over a wide area. Before the experiment, we measured the cross-polarization discrimination (XPD) factor in a chamber. In the pre-experiment, we transmitted

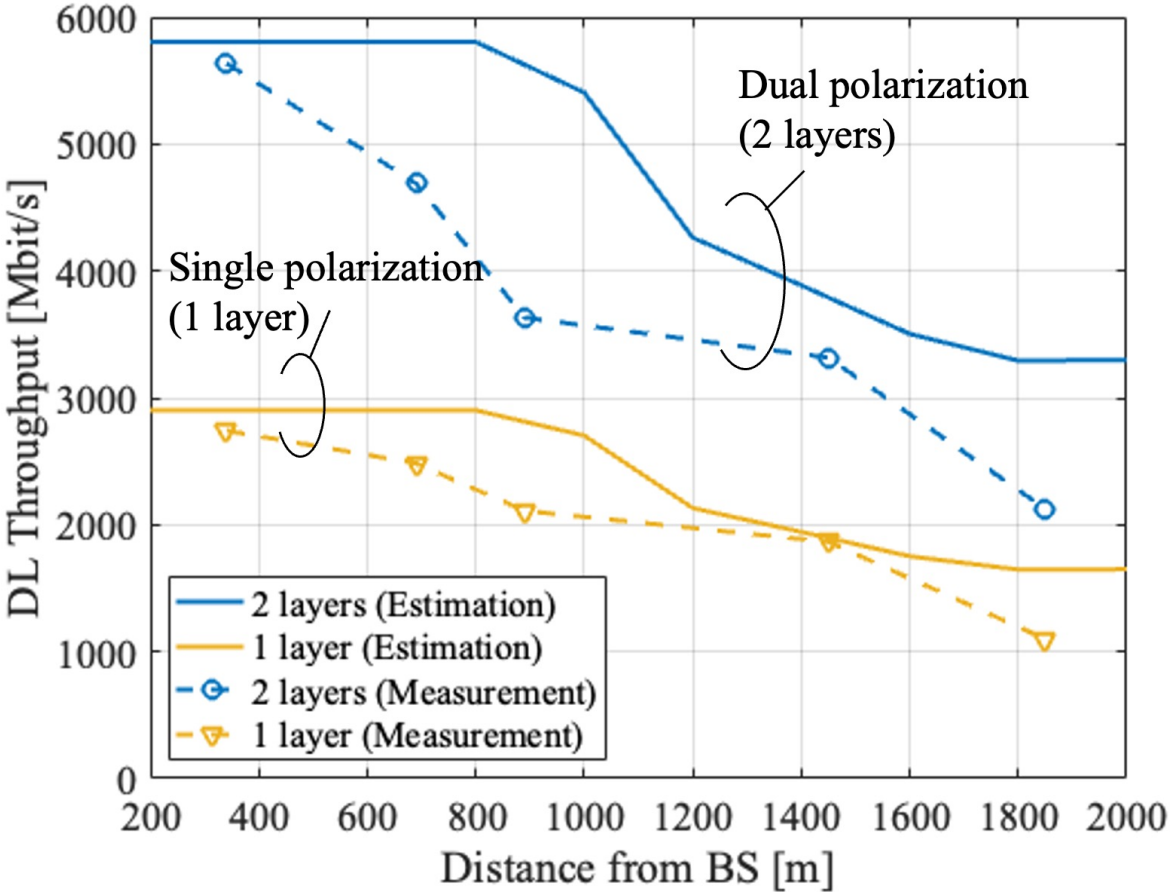

Figure 2.19 Comparison with the estimated throughput

Table 2.6 SINR of horizontal and vertical polarizations at each location

Location	TM #1	TM #2	
	SINR (V pol.)	SINR (H pol.)	SINR (V pol.)
A	19.7 dB	20.7 dB	19.4 dB
B	19.2 dB	18.4 dB	19.1 dB
C	17.5 dB	14.0 dB	17.1 dB
D	12.9 dB	12.9 dB	12.9 dB
E	7.1 dB	8.0 dB	7.6 dB

Table 2.7 DL throughput with pedestrian mobility at location D

TM	# of Layers	DL Throughput
#1	1	1.83 Gbit/s
#2	1	2.0 Gbit/s
#3	2	3.09 Gbit/s

an H-polarization signal and measured the received power on H-polarization (P_{HH}) and the received power on V-polarization (P_{VH}) on the receiver side. The XPD ($= P_{HH}$ P_{VH} [dB]) is approximately 30 dB, which is sufficient to limit the crosstalk between the 2 MIMO layers. Although the XPD normally decreases as the distance increases [24], we are able to retain sufficiently good XPD up to 1850 m in the experiments.

We also verified the throughput with pedestrian mobility at location D at 1450 m. The mobility speed is approximately 5 km/h. The driving course is the same for each test, and LOS conditions are secured during the measurement. CPE Type 1 is used in this experiment. The measurement results are summarized in Table 2.7. The DL throughput of 3.09 Gbit/s is achieved with pedestrian mobility at approximately 5 km/h.

2.4.2 Throughput performance at NLOS location

The mmWave bands not only have high path loss but also attenuation tends to increase due to blocking by obstacles, e.g., buildings and people. Generally speaking, it is difficult for mmWave systems to communicate in NLOS environments. Therefore, we investigated the throughput performance in the 39-GHz band at NLOS location F. Location F is relatively

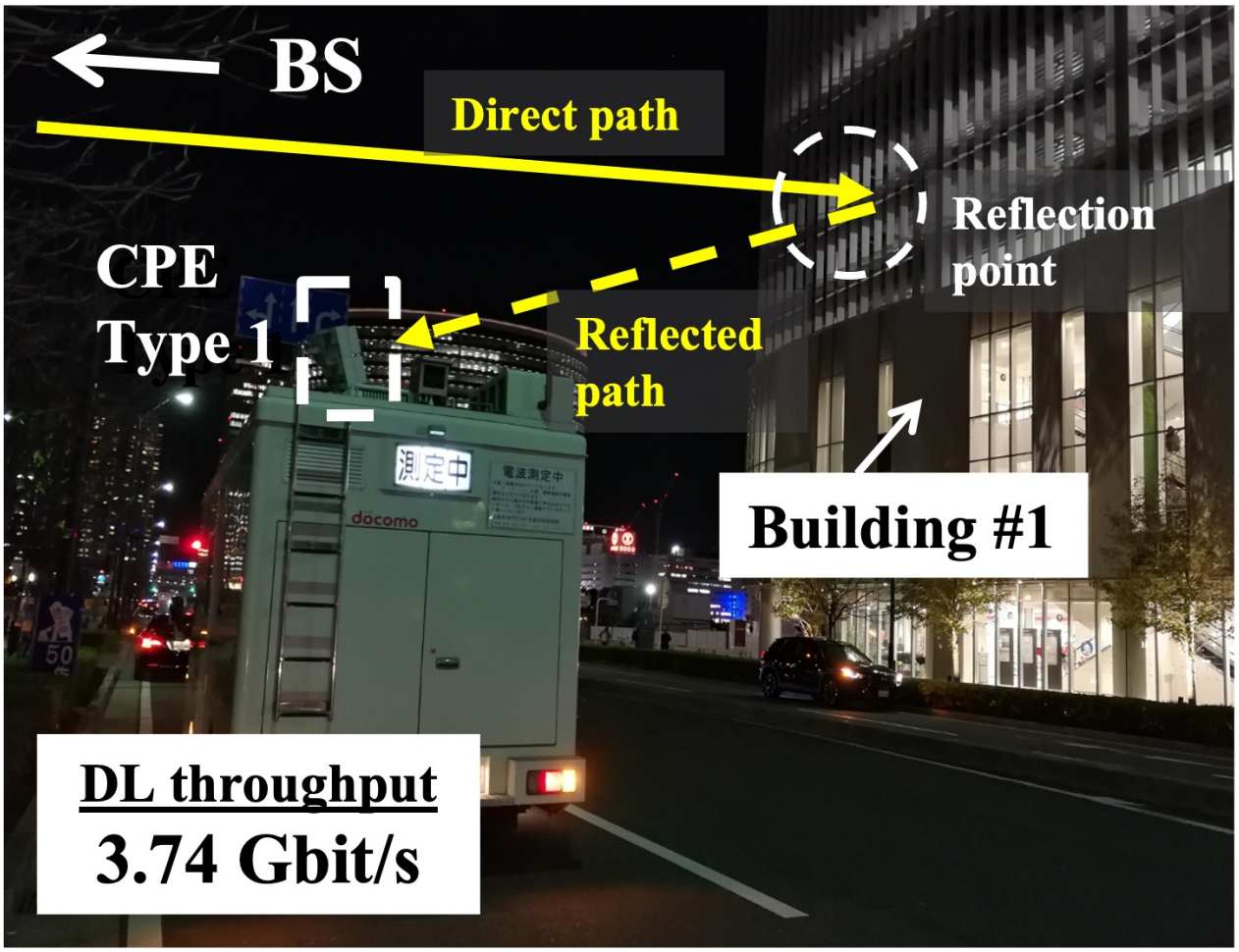

Figure 2.20 Measurements at NLOS location F (Reflected path from Building #1)

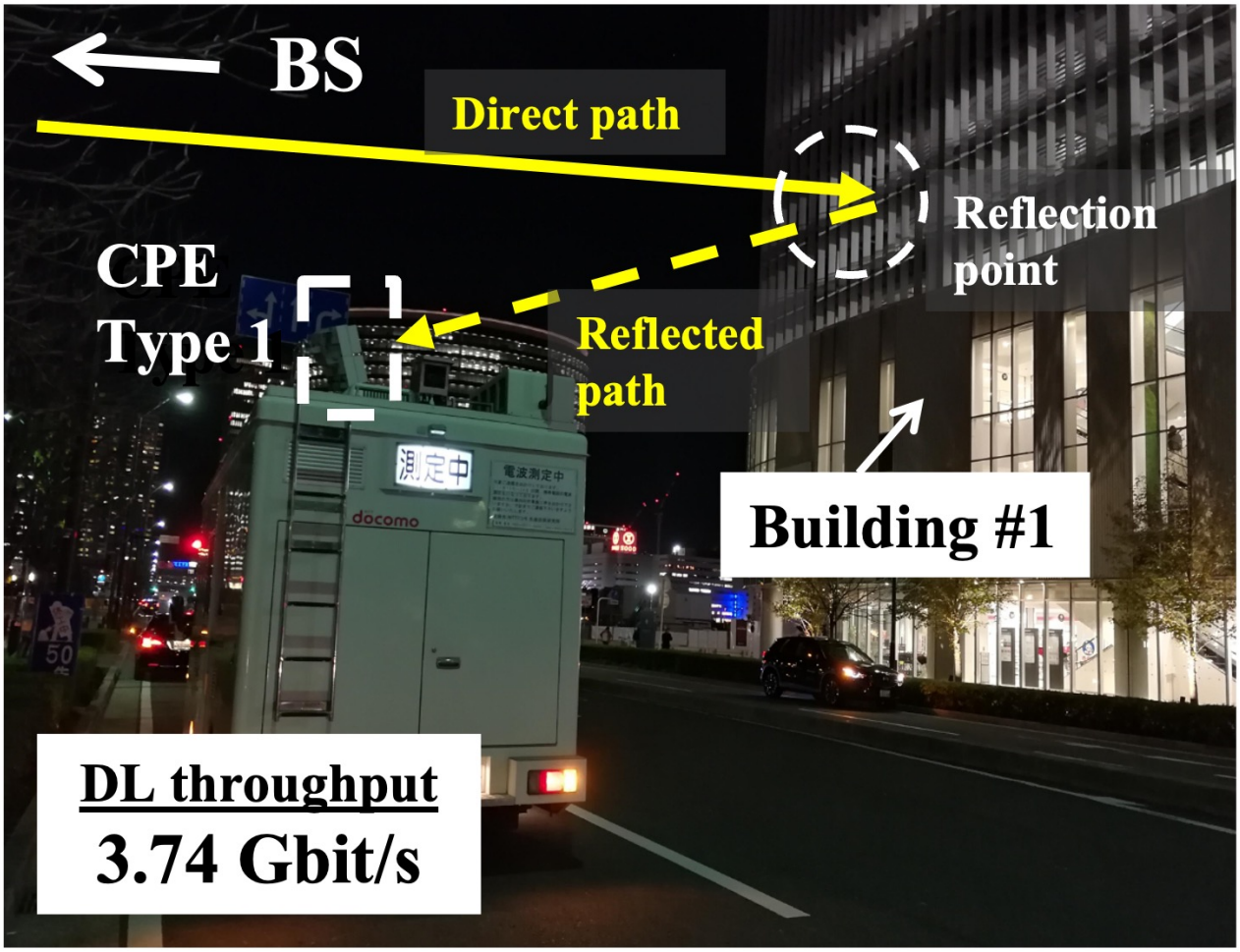

Figure 2.21 Measurements at NLOS location F (Reflected path from Building #2)

close to the BS, and the distance from the BS site is approximately 360 m.

Measurement results and scenarios are shown in Fig. 2.20 and 2.21. Although location F is NLOS, the maximum throughput of 3.74 Gbit/s is achieved as shown in Fig. 2.20, and we achieve throughput exceeding 1 Gbit/s in the NLOS location. Then, since CPE Type 1 is directed toward Building #1, it receives the reflected path from that building. On the other hand, CPE Type 1 receives other reflected paths at location F, as shown in Fig. 2.21. In this case, the throughput is approximately 425 Mbit/s, and is lower than the throughput in the case in Fig. 2.20. The difference between Figs. 2.20 and 2.21 is the direction that CPE Type 1 faces. In 2.21, CPE Type 1 is directed toward Building #2. Since Building #2 is approximately 330 m away from the test vehicle, the reflection point in the case of Fig. 2.21 is farther than that in the case in Fig. 2.20. Note that no throughput was obtained when CPE Type 1 was unable to receive the reflected waves shown in Figs. 2.20 and 2.21. The throughput difference between Figs. 2.20 and 2.21 is due to the difference in distance from the reflected point. Since the 39-GHz wave is scattered on the rough or non-flat surface of the building wall, it is not reflected to a specific direction but scattered to various directions. Therefore, if the reflected point is close, the receiver may be able to receive many scattered paths. On the other hand, if the reflected point is far away, the receiver is able to receive only a few scattered paths and the received power becomes lower.

Based on the above results, we confirmed the possibility of achieving high throughput even under NLOS conditions if a reflected path is received in the mmWave system. Actually, since the performance depends on whether or not there is a reflector around the UE and the distance from the reflection point, there are challenges in controlling the performance and to cover NLOS areas.

2.4.3 Wide area mobility

The objectives of these experiments are to investigate and verify the mobility performance and beam tracking within a single site (different sectors). In these experiments, CPE Type 2 is used. We tested 20-km/h mobility in the driving course shown in Fig. 2.16. We conducted a preliminary evaluation and confirmed that the coherency of the selected beam pair can be retained in the test scenario.

The results are shown in Fig. 2.22. We observe that the BS and UE beam index change as the UE position changes. As a result, DL throughput exceeding 1 Gbit/s is achieved even with mobility over a wide area, and the maximum throughput is 1.58 Gbit/s. When

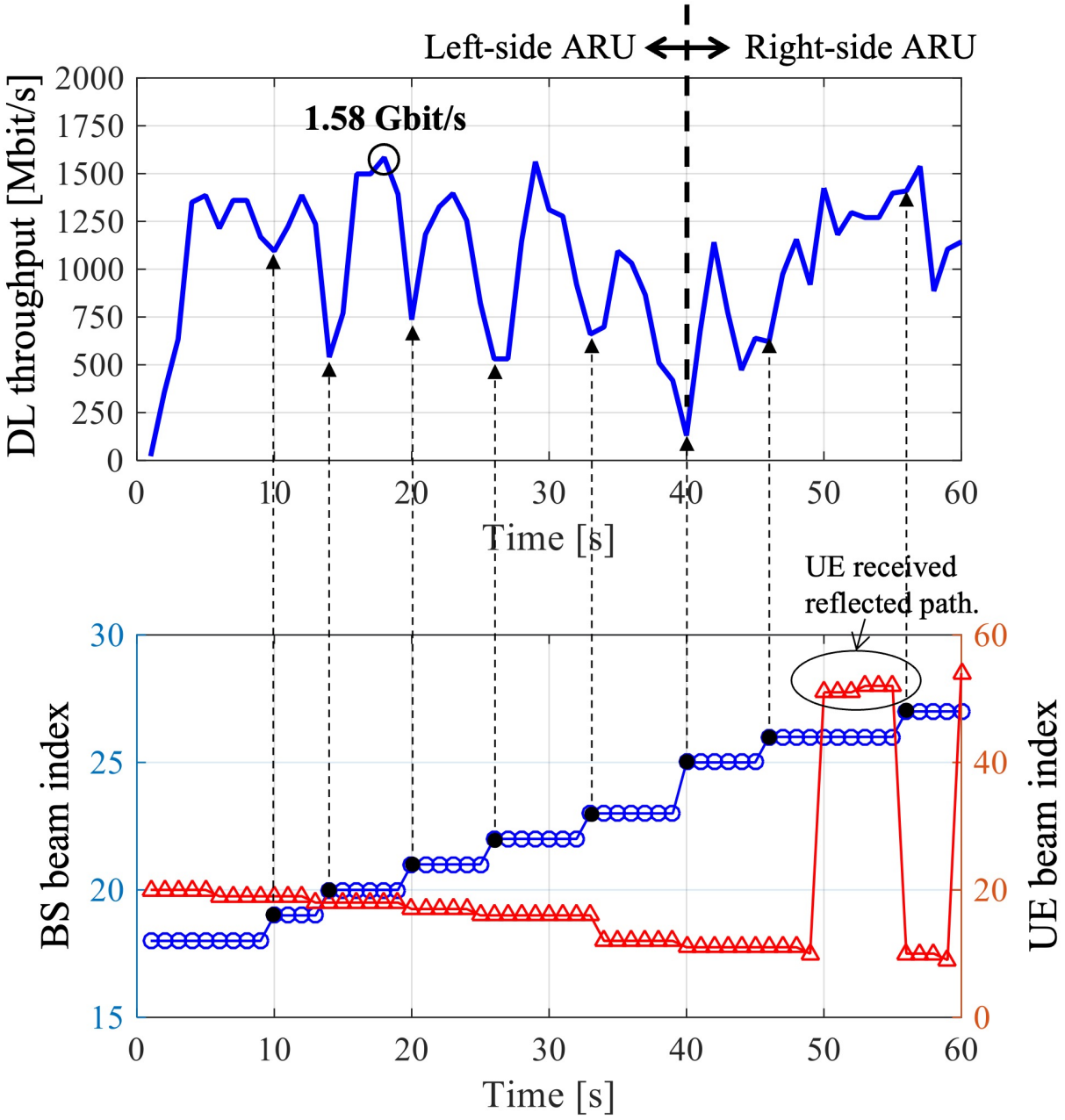

Figure 2.22 Downlink throughput, BS and UE beam index with 20-km/h mobility

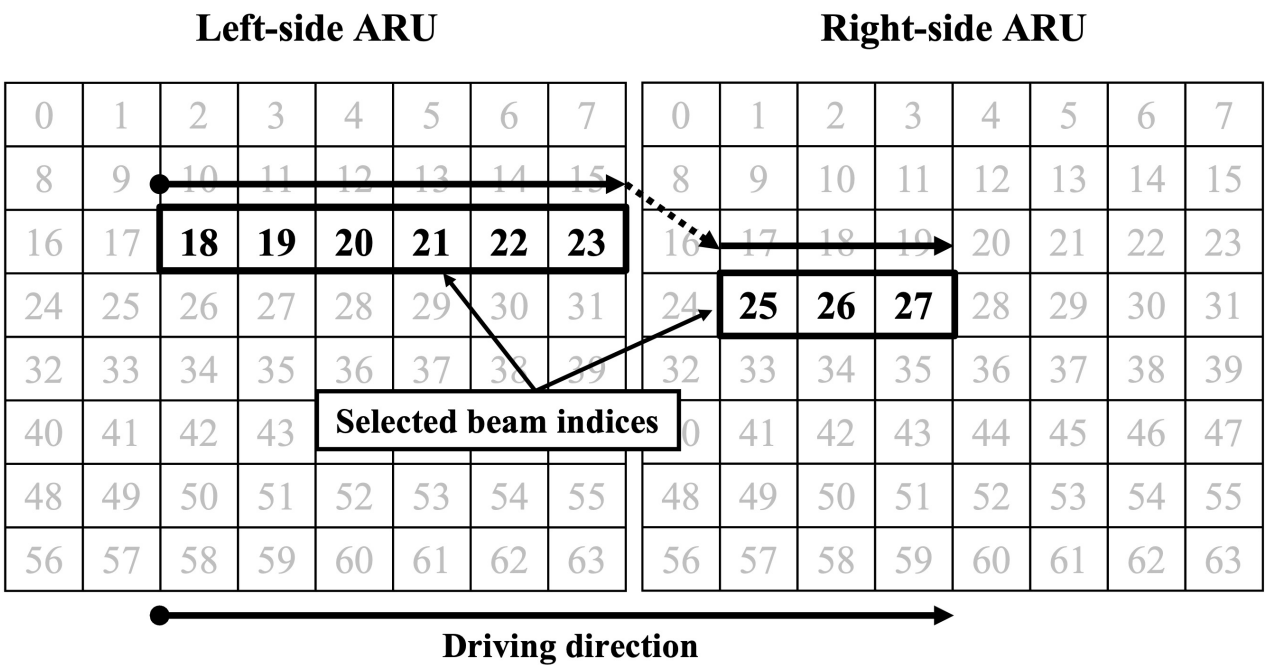

Figure 2.23 Selected beams at the BS

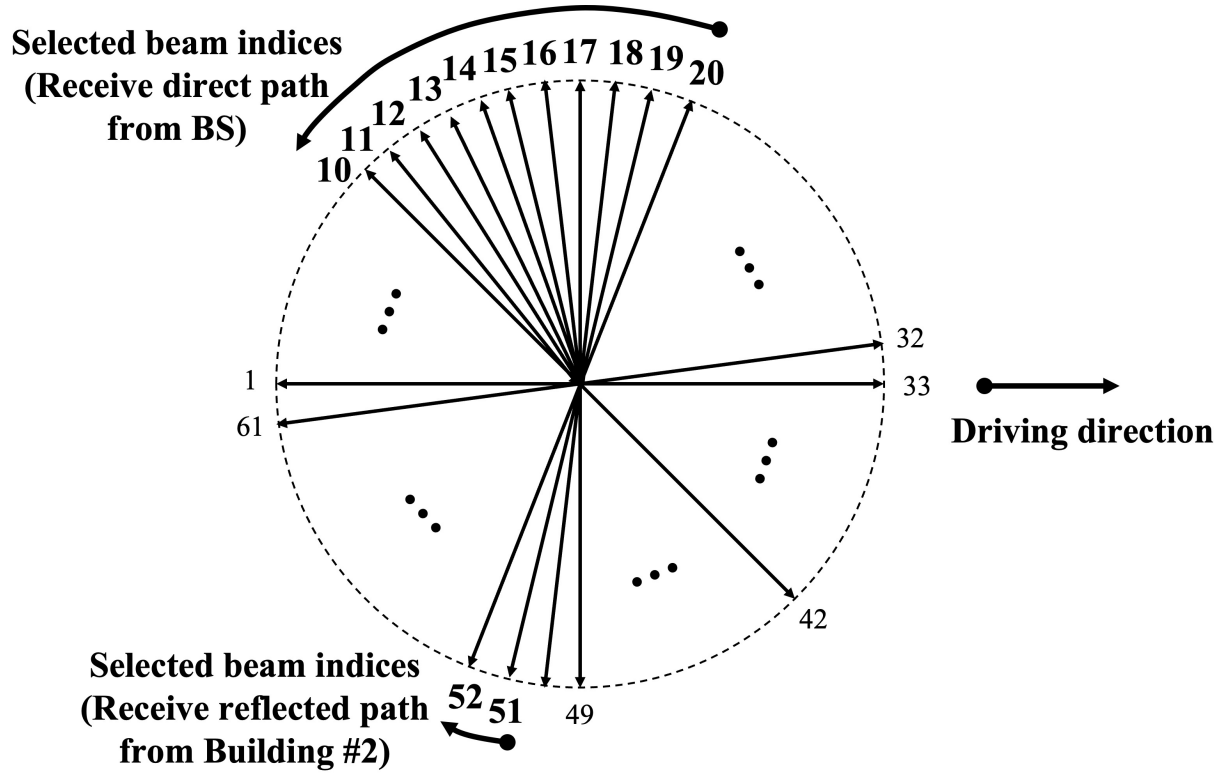

Figure 2.24 Selected beams at the UE

comparing the DL throughput and the BS beam index in Fig. 2.22, a different BS beam index is selected when the DL throughput sharply drops. After the BS beam index is changed, the DL throughput is recovered. Fig. 2.23 and 2.24 indicates selected beams at the BS and UE. From Fig. 2.23 and 2.24, we find that the beam index is sequentially selected according to the movement of the UE. Moreover, focusing on the UE beam index from 50 seconds to 55 seconds after the start of measurement in Fig. 2.22, beams in completely different directions are selected at the UE. We find that the UE receives a reflected path from Building #2 based on Figs. 2.16 and 2.24. At the end of the test course, the UE traverses between Building #2 and a construction site. Since there is some construction equipment between the BS and UE at the end of the course, the direct path from the BS is sometimes blocked by these machines. As a result, the power of the reflected path becomes higher than that of the direct path, and the UE selects different beams (the beam index #51 or #52). Based on the above observations, we conclude that the beam tracking is effectively conducted in the experiments.

On the other hand, large drops in the DL throughput are observed when the UE direction falls between two beams. It is due to the gap of beam gain shown in Fig. 2.3 and 2.4. Additionally, when beam switching occurs across multiple ARUs of the BS, a large drop in the throughput is observed. In order to reduce these degradations, it is necessary to improve the mmWave antenna and to develop a faster beam tracking scheme. These are also future challenges for actualizing mmWave systems.

2.5 Summary

This chapter presented experiments using the 39-GHz band to provide high data rates and long-range communications with mobility support. The experiments used a high beamforming gain antenna and beam-tracking technology to achieve throughput of 1 Gbit/s or more, and we achieved throughput of 3.35 Gbit/s and 2.14 Gbit/s at a transmission range of 1450 m and 1850 m, respectively. Moreover, the experimental results show high throughput can be obtained even in NLOS locations, and we achieved 3.74 Gbit/s at an NLOS location. Furthermore, with 20-km/h mobility we achieved throughput of 1.58 Gbit/s. However, in order to utilize mmWave for mobile communications, expanding the coverage to NLOS areas and improving the beam searching and tracking method are important challenges in the future. Additionally, although we were able to conduct measurements without rain in these experiments, it is known mmWave bands are affected by rain attenuation. Also in the 39-

GHz band, approximately 8-dB/km attenuation is caused by heavy rain (The rainfall rate is 25 mm/h) [25]. In the deployment process for wide-area coverage using 39 GHz, we must consider and investigate the effect of rain attenuation. Furthermore, assuming applications and services, comprehensive verification considering upper layers, e.g., the TCP/IP layer, is also important in the future.

Chapter 3

Massive analog-relay MIMO for achieving spatial-resource redundancy

3.1 Motivation

As mentioned in the previous chapter, to improve millimeter wave communication, spatial resource redundancy using beamforming and wireless relay technology is proposed. To realize spatial resource redundancy, it is necessary to distribute transmission points. There are several candidate solutions, as shown in Table 3.1. In Table 3.1, we assume a disturbed unit (DU) in a cellular system as a distributed antenna. Analog relay is a cost-effective and suitable solution for distributed deployment of a large number of transmission points. Analog relay has lower reception quality than distributed antennas. However, as will be described later, almost the same performance can be achieved under certain conditions. Therefore, we studied spatial resource redundancy using analog-relay solution. A repeater is known as an analog-relay solution. A large number of beamforming repeaters are deployed in space, and the communication paths are adaptively formed by beam control. Such a system has been proposed as massive analog-relay MIMO [38]. This chapter proposes a user-driven relay beamforming method for the massive analog-relay MIMO to improve mmWave communications. To control relay beamforming, a network-driven approach can be considered. This approach manages the relay beams from the network side. However, since the BSs and the relay nodes are remotely distributed, the control latency and overhead increase proportionately to the beam candidates and the number of RNs. To efficiently control multiple RNs, we propose the user-driven method. From the results shown in section 2, we can find that the selected

Table 3.1 Candidate solutions for spatial resource redundancy

	Distributed antenna	Digital relay	Analog relay	Reflector
Reception quality	High	Medium	Medium	Low
Latency	Short	Long	Short	Short
Cost	High	High	Medium	Low
Power consumption	High	High	Medium	Low
Hardware scale	Large	Large	Small	Small

analog beam corresponds to the user location. Therefore, we focus on a method that utilizes user location information. Assuming V2X applications, the proposed method employs side information, such as location information, which can be obtained from Cooperative Awareness Message (CAM) [39], for controlling the relay beam. The CAM is a kind of Intelligent Transport Systems (ITS) message, and UE can broadcast the message. For V2X applications, the concept of beam alignment between BS and vehicles using location information had been discussed in [40] and [41]. In [40], the location-based approach can significantly reduce the mmWave beam alignment overhead while having marginal performance degradation. However, these studies mainly focus on the initial beam search of the base station (BS) and do not cover beam operation of analog relay. Also, there are no specific proposals and evaluations on beam tracking at the RNs. In this paper, we propose an user driven beam searching and tracking method for a massive RNs with low overhead that obtain the benefits of massive relay MIMO.

The rest of this chapter is organized as follows. Section 3.2 discusses conditions under which the analog-relay system is effective. Section 3.3 describes and formulates the massive analog-relay MIMO. Section 3.4 proposes the user-driven relay-beam control method for massive RNs. Simulation evaluations are discussed in Section 3.5. Finally, Section 3.6 concludes this chapter.

3.2 Comparison between distributed antenna and analog relay

Before discussing the massive analog-relay MIMO, this section compares distributed-antenna systems and analog-relay systems and analyzes the conditions under which analog relay is

effective. Figure 3.1 shows the system model. Distance d_1 and d_2 show BS-RN distance and RN-UE distance, respectively. Radio communication systems have required received power P_{target} to achieve the maximum transmission rate. Considering the difference between the two systems, equation 3.1 shows the conditions under which the transmission rate of the analog-relay system are equivalent to those of the distributed-antenna system. Here, down link transmission is assumed. P_r and P_d are received power of analog-relay system and distributed-antenna system, respectively. The amplification gain of the analog relay node is expressed as β dB.

$$P_r = P_d + G_t - L_1 + \beta + F_r - \delta_n \geq P_{target} \tag{3.1}$$

δ_n is the difference between the noise power of the analog-relay system P'_n and the noise of the distributed-antenna system P_n, and is expressed as $\delta_n = P'_n - P_n$ dB. Equation 3.1 gives the following inequality.

$$\alpha = G_t + \beta + F_r \geq L_1(d_1) - P_{margin}(d_2) + \delta_n(d_2, \beta) = \alpha_{min} \tag{3.2}$$

Here, P_{margin} is defined as $P_{margin} = P_d - P_{target}$. P_{margin} may be calculated from the SNR difference instead of the received power difference. $\alpha = G_t + \beta + F_r$ is a design value, and if α is designed to satisfy Equation 3.2, the analog-relay system can achieve the same transmission rate as the distributed-antenna system.

To clarify the conditions under which analog relay is effective, we performed several evaluations using the conditional expression shown in Equation 3.2. Figure 3.2 shows the result of the design value α that the analog-relay system should satisfy. Table 3.2 shows the evaluation conditions. Path losses L_1 and L_2 are assumed to be free-space propagation losses.

From Figure 3.2, it can be observed that α_{min} increases as the distances d_1 and d_2 increase. To achieve large α_{min}, it is necessary to design large BS antenna gain G_t, relay receiving antenna gain F_r, and relay amplification gain β. As an example of realistic design values, if $G_t = 20$ dB, $F_r = 20$ dB, and $\beta = 40$ dB are assumed, α_{min} is 80 dB. Then, Figure 3.3 shows the area where the analog-relay system is also effective. When d_1 is 100 m, the maximum d_2 is approximately 70 m, and when d_1 is 200 m, the maximum d_2 is approximately 35 m. Hence, it is important to consider under what conditions the analog-relay system is applied. Massive analog-relay MIMO discussed in this chapter targets the NLOS area where d_1 is about 100 m. From Figure 3.3, the analog-relay system is effective in such region.

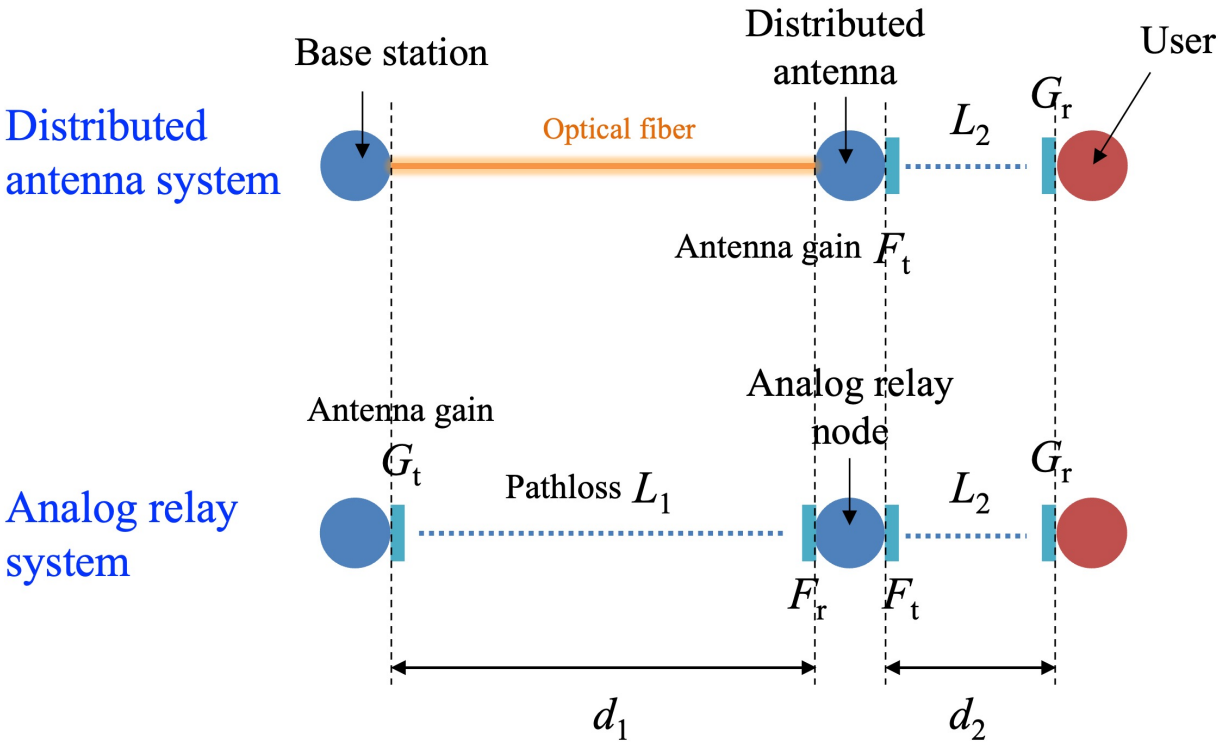

Figure 3.1 Comparison models of distributed-antenna system and analog-relay system

Table 3.2 Evaluation parameters

Parameter	Value
Center frequency	28 GHz
Bandwidth	100 MHz
Transmission power	30 dBm
Noise density	-174 dBm/Hz
Noise figure	5 dB
Relay transmission antenna gain F_t	20 dB
UE antenna gain G_r	5 dB
Target SNR	24.6 dB

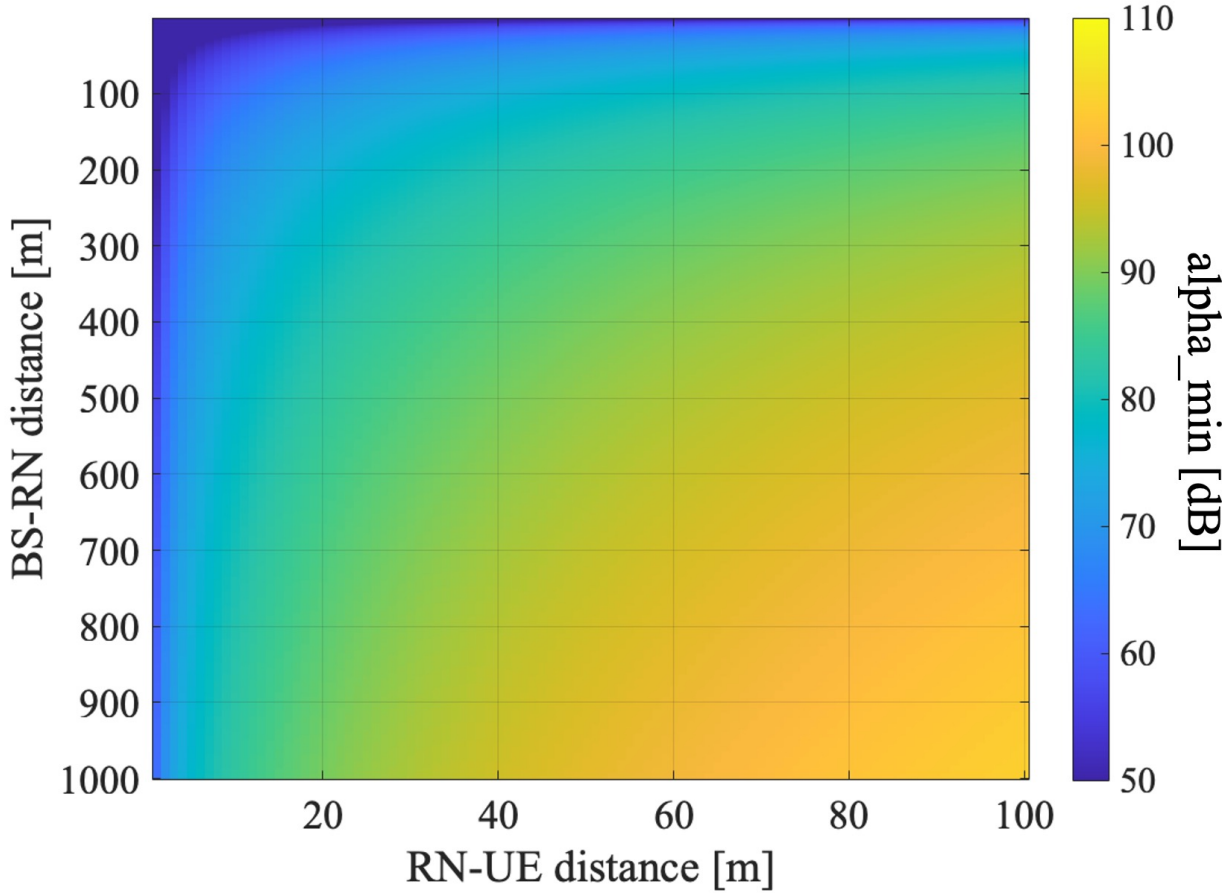

Figure 3.2 Minimum design value for analog-relay system with transmission rate equivalent to distributed-antenna system

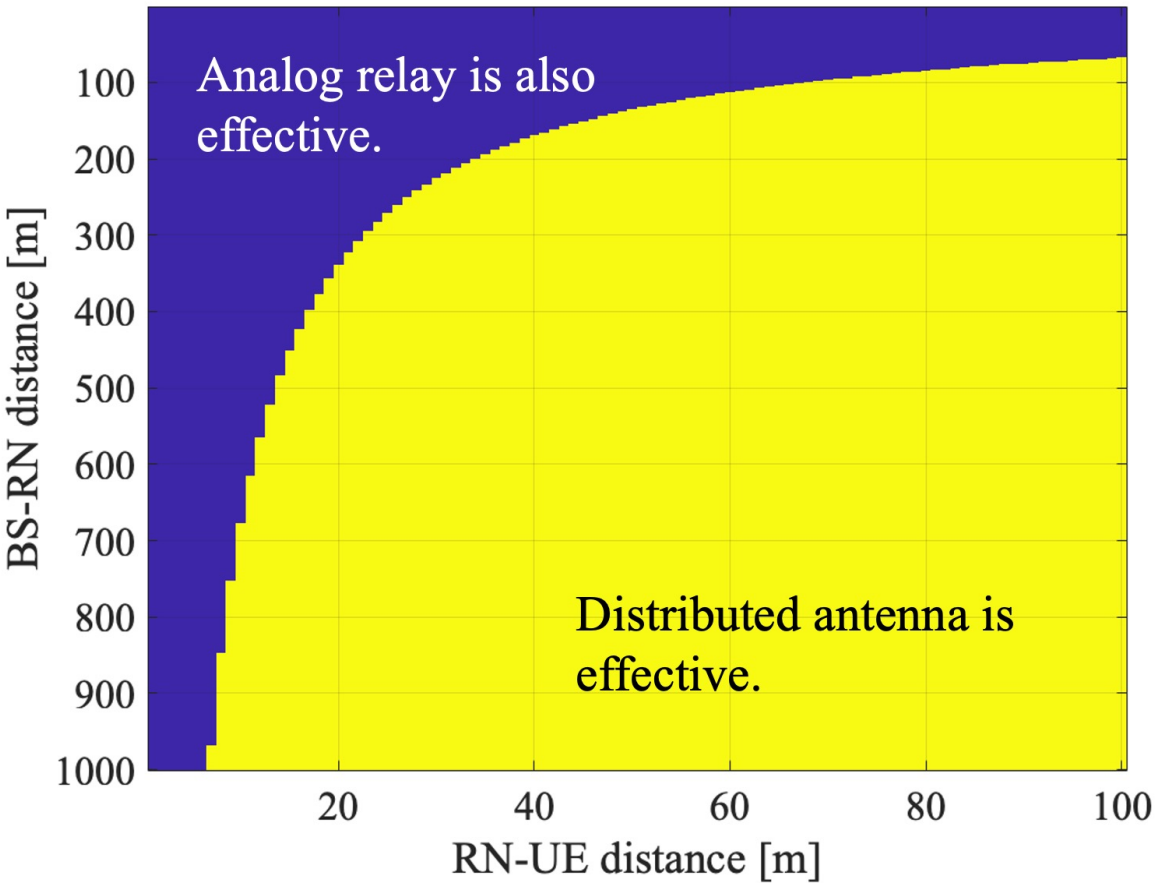

Figure 3.3 Region for analog-relay system with transmission rate equivalent to distributed-antenna system when α_{min} is 80 dB

3.3 Massive analog-relay MIMO

This section describes the massive analog-relay MIMO and formulates the channel newly generated by multiple RNs. Figure 3.4 shows the system configuration discussed in this paper. The configuration is composed of one BS with M_t antennas, K RNs and one UE with M_r antennas. Full-array hybrid beamforming [42] is assumed in both of BS and UE. Figure 3.5 illustrates the architecture of the analog RNs, such as a radio repeater, assumed in this study. Unlike DF relay, AF relay does not involve digital signal processing for mmWave signals and thus radio signals can be relayed with low latency. To compensate for attenuation of mmWave, massive analog-relay MIMO performs beamforming in analog RNs. Furthermore, since hardware cost is lower, it is possible to reduce the network cost when considering the distribution of massive RNs. Unlike conventional AF relay, massive analog-relay MIMO also performs beamforming in analog RNs to compensate for attenuation of mmWave. The RNs support analog beamforming only. In the analog beamforming, the same analog signal is fed to each antenna and then analog phase shifter to steer the signal. In the proposed method described in the next section, the analog RN consists of transceiver that acquires information to control its analog beam-forming. The transceiver is used to receive the CAM and control relay beam. Since the transceiver is assumed to utilize low frequency bands used by ITS, it is relatively in-expensive compared to the mmWave band transceiver.

The signal model of massive analog-relay MIMO is formulated. The weight matrices in analog domain are $\mathbf{V}_{\mathrm{a}} \in \mathbb{C}^{M_t \times N_s}$ in BS and $\mathbf{W}_{\mathrm{a}} \in \mathbb{C}^{M_r \times N_s}$ in UE. Then, N_s means the number of streams. The weight matrices in digital domain are $\mathbf{V}_{\mathrm{d}} \in \mathbb{C}^{N_s \times N_s}$ and $\mathbf{W}_{\mathrm{d}} \in \mathbb{C}^{N_s \times N_s}$ in the BS and the UE, respectively. When the channel between the BS and the UE is defined as $\mathbf{H} \in \mathbb{C}^{M_r \times M_t}$. Assuming DL transmission through this paper, the received signal $\mathbf{y} \in \mathbb{C}^{N_s \times 1}$ is represented as follow.

$$\begin{aligned} \mathbf{y} &= \mathbf{W}_{\mathrm{d}}^{\mathrm{H}} \mathbf{W}_{\mathrm{a}}^{\mathrm{H}} (\mathbf{H} \mathbf{V}_{\mathrm{a}} \mathbf{V}_{\mathrm{d}} \mathbf{x} + \mathbf{n}) \\ &= \mathbf{W}_{\mathrm{d}}^{\mathrm{H}} \mathbf{W}_{\mathrm{a}}^{\mathrm{H}} \mathbf{H} \mathbf{V}_{\mathrm{a}} \mathbf{V}_{\mathrm{d}} \mathbf{x} + \mathbf{W}_{\mathrm{d}}^{\mathrm{H}} \mathbf{W}_{\mathrm{a}}^{\mathrm{H}} \mathbf{n} \\ &= \mathbf{W}_{\mathrm{d}}^{\mathrm{H}} \tilde{\mathbf{H}} \mathbf{V}_{\mathrm{d}} \mathbf{x} + \mathbf{W}_{\mathrm{d}}^{\mathrm{H}} \tilde{\mathbf{n}} \end{aligned} \tag{3.3}$$

Then, $\mathbf{x} \in \mathbb{C}^{N_s \times 1}$ and $\mathbf{n} \in \mathbb{C}^{N_s \times 1}$ indicates transmitted signal and noise, respectively.

Next, channel representation in massive analog-relay MIMO is described. Transmit and receive analog beamforming weights in K RNs are $\mathbf{U}_r = \mathrm{diag}(\mathbf{u}_{r,k}) \in \mathbb{C}^{KL_r \times K}$ and $\mathbf{U}_t = \mathrm{diag}(\mathbf{u}_{t,k}) \in \mathbb{C}^{KL_t \times K}$, respectively. Then, the vector $\mathbf{u}_{t,k} \in \mathbb{C}^{K_t \times 1}$ and $\mathbf{u}_{r,k} \in \mathbb{C}^{K_r \times 1}$ mean analog weights in the k-th RN. Using the amplifier gain of the k-th RN g_k, the amplifier-gain

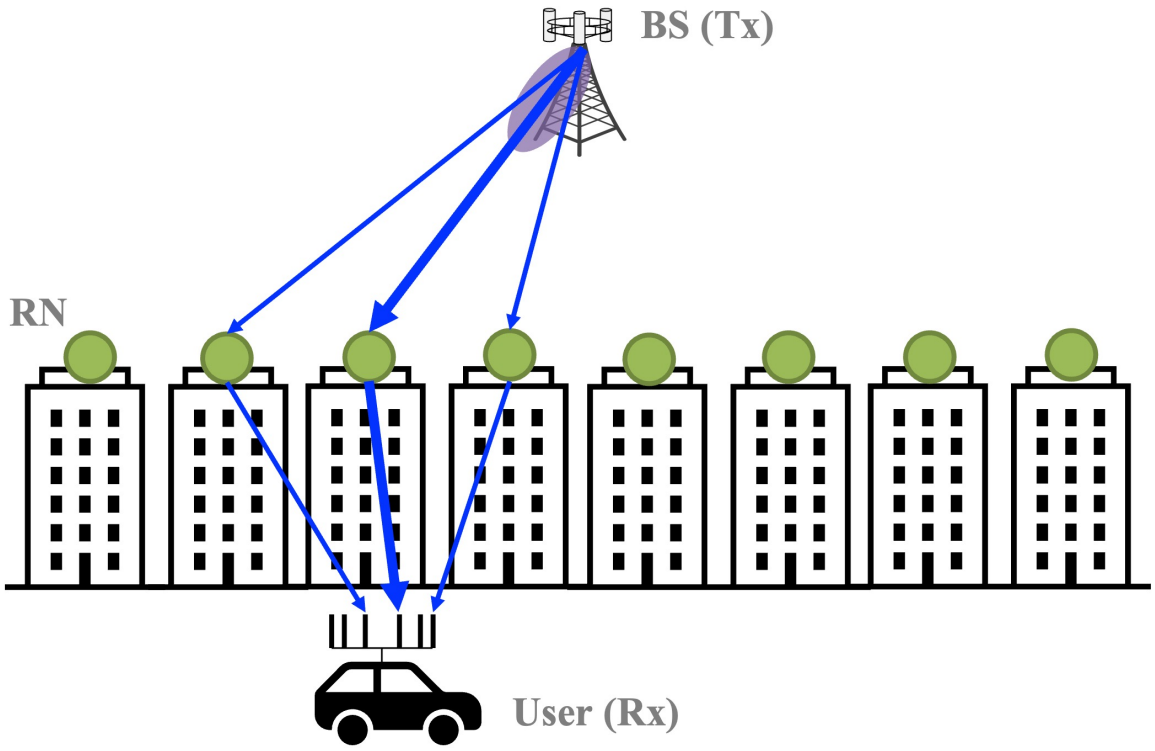

Figure 3.4 System model of the massive analog-relay MIMO in V2X applications

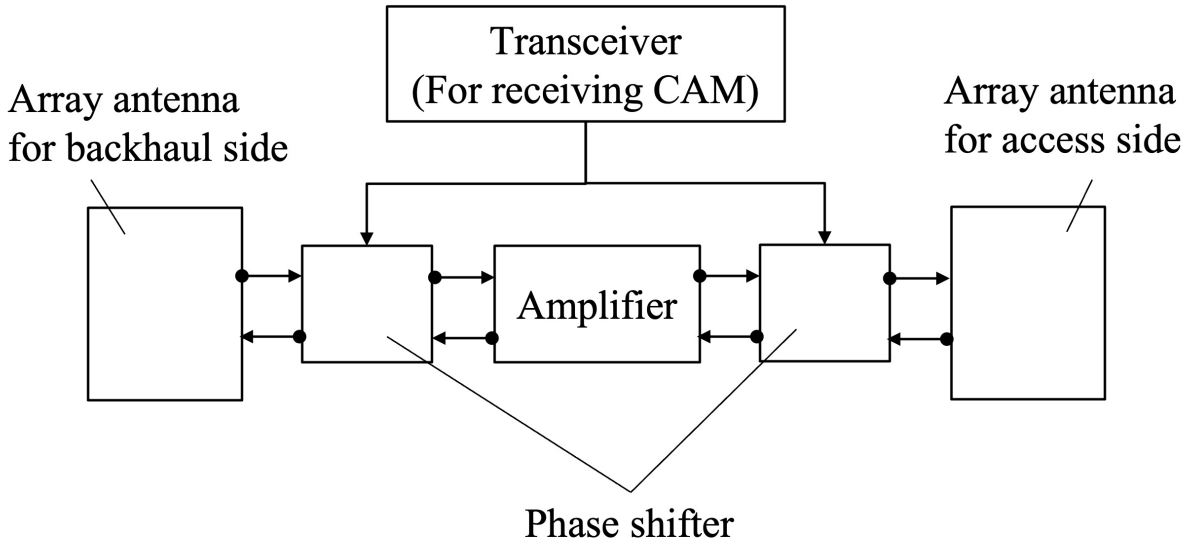

Figure 3.5 Architecture of the analog RN in massive analog-relay MIMO

matrix is defined as $\mathbf{G} = \mathrm{diag}(\sqrt{g_k}) \in \mathbb{C}^{K\times K}$. When a channel matrix between the BS and the RNs is $\mathbf{H}_1 \in \mathbb{C}^{KL_r\times M_t}$, a channel matrix between the RNs and the UE is $\mathbf{H}_2 \in \mathbb{C}^{M_r\times KL_t}$ and a channel matrix between the BS and the UE is $\mathbf{H}_0 \in \mathbb{C}^{M_r\times M_t}$, the channel matrix in the massive analog-relay MIMO system $\mathbf{H}$ is represented as follow.

$$\mathbf{H} = \mathbf{H}_0 + \mathbf{H}_2\mathbf{U}_\mathrm{t}\mathbf{G}\mathbf{U}_\mathrm{r}^\mathrm{H}\mathbf{H}_1 \tag{3.4}$$

Although the analog RN can improve received power, it causes additional noise. Here, if $\mathbf{n}_\mathrm{R} \in \mathbb{C}^{(K\times 1)}$ expresses noise added in the analog RNs, the noise vector $\mathbf{n}$ in Equation (3.3) is rewritten as follow.

$$\mathbf{n} = \mathbf{H}_2\mathbf{U}_\mathrm{t}\mathbf{G}\mathbf{n}_\mathrm{R} + \mathbf{n}' \tag{3.5}$$

Then, $\mathbf{n}'$ is noise in the UE. From above equations, the rate of massive analog-relay MIMO can be expressed as Equation (3.5). Here, it assumes Singular Value Decomposition (SVD) -MIMO and equal power allocation to each stream.

$$
\begin{aligned}
C &= \log_2 \det \left(\mathbf{I} + \frac{\left| \mathbf{W}_{\mathrm{d}}^{\mathrm{H}} \tilde{\mathbf{H}} \mathbf{V}_{\mathrm{d}} \right|^2 |\mathbf{x}|^2}{|\mathbf{W}_{\mathrm{d}}^{\mathrm{H}} \tilde{\mathbf{n}}|^2} \right) \\
&= \sum_{m=1}^{N_s} \log_2 \left(1 + \frac{\lambda_m P_x}{N_s P_n} \right)
\end{aligned}
\tag{3.6}
$$

Then, P_x and P_n are transmission power and noise power, respectively. λ_m means m-th singular value.

3.4 User-driven analog-relay beamforming

Massive analog-relay MIMO can improve a channel characteristic by adjusting U_t, U_r and G in Equations (3.4) and (3.5). This paper mainly focuses on the relay-beamforming matrix Ut that needs to be dynamically controlled as the UE moves. To track the UE, the RNs control analog beamforming. However, they have no signal-processing function supporting mmWave bands. Therefore, how to properly search analog beam in the RNs is one of the important issues. One of possible methods is exhaustive search, where BS and UE cooperate to measure the channel state or quality for all relay-beam candidates. After searching all channel qualities, the BS selects relay beams and notifies the RNs of the beam information. This method has the problem of increased overhead in proportion to the number of RNs due to the channel measurement and the notification. Since the massive analog-relay MIMO utilizes multiple RNs, the overhead is large. Therefore, such exploratory methods are not suitable.

To solve this issue, this paper proposes a user-driven relay-beamforming method. The proposed approach consists of two phases. Analog-beamforming weights of the RN called relay-beamforming weights are searched in the first phase. To decide the analog-beamforming weights while keeping few overheads, the proposed method utilizes location information. After finding the relay beamforming weights, beamforming weights of the BS and the UE are searched in the second phase. In this phase, the beamforming weights are calculated based on reference signal, such as CSI-RS. The second phase may occur any number of times before the relay-beamforming weight is updated.

There are concerns about the proposed method. One of the concerns is error of location estimation. It was difficult to apply such an approach because the position estimation

error is large in a typical positioning method such as the conventional Global Positioning System (GPS) and cellular positioning. However, recent positioning technologies, which are discussed in some standards such as 3GPP release 16 [43] and IEEE 802.11az [44], have centimeter-level accuracy. Additionally, V2X applications such as autonomous driving car require high-precision positioning. Therefore, V2X UE has a function that enables high-precision positioning such as Global Navigation Satellite System (GNSS) and Light Detection And Ranging (LiDAR) [45]. Considering the recent location estimation techniques in V2X applications, the concern about location estimation error can be solved. Another concern is the inability to support users in non-line-of-sight (NLOS) from RNs. As described later, the proposed method geometrically selects relay beams based on the estimated locations. In NLOS environments, since it is likely that the direct waves from the RN will no longer be dominant, the proposed method may be not suitable to select beams for users in NLOS. However, we assume that the proposed method will be applied to mmWave communications. The performance of mmWave communication is greatly degraded in NLOS environments. Considering mmWave communication is basically applied to Line-Of-Sight (LOS) communications, the proposed method is suitable under the assumption.

3.4.1 User-driven relay-beam selection

The user-driven relay-beam selection method involves two phases. The first phase consists of four steps to compute the beamforming weight of RNs. The second phase consists of one step that determines the beamforming weight of BS and UE. Figure 3.6 shows the control flow of the proposed method. The flow consists of five steps.

1. (Step 1) Relay-beam configuration on backhaul side: Assuming a static radio environment where the BS and the RNs are fixed, the same relay beam continues to be selected on the backhaul side. Therefore, it is sufficient to adjust the beam when installing the RN or after a long period. Even if the RN moves, the beam on the backhaul side can be determined in the same way as in Step 4 (it is necessary to replace the UE in Step 4 with BS.). Then, RN need to have location-estimation function to know the location of BS that it should connect to. The assumption of fixed RN is reasonable, since the RN rarely moves in actual deployment. Thus, the beam on the backhaul side is determined appropriately in advance.

2. (Step 2) UE location estimation: The relay beam on the access side needs to track the

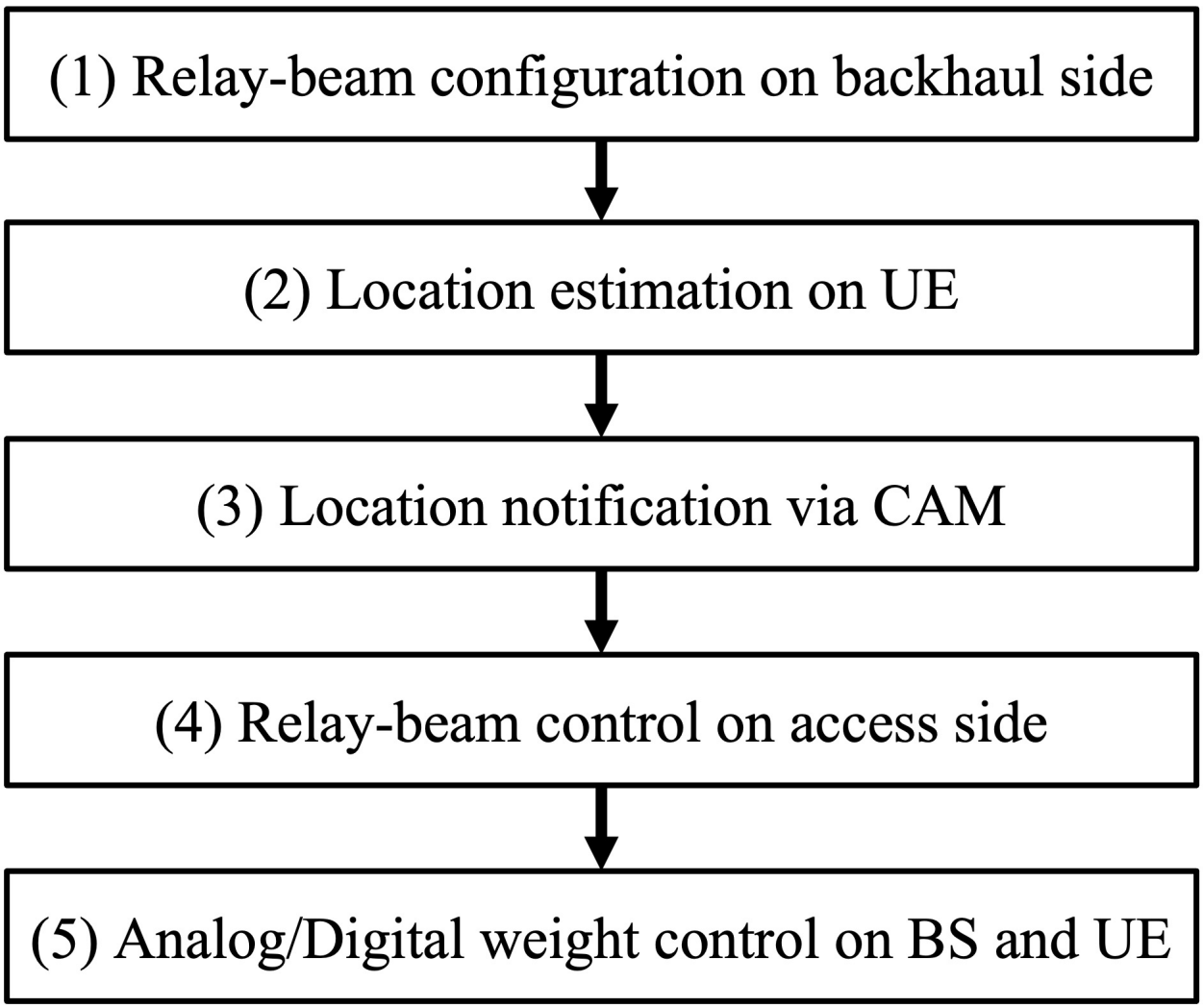

Figure 3.6 Control flow of the user-driven relay-beam selection

target UE. The proposed method controls the relay beam by utilizing location information. In the proposed method, utilizing high-precision positioning such as LiDAR is assumed on the UE. Note that it is assumed the location information of BS and each RN are obtained when equipment are installed. The estimated location $p_m = (x_m, y_m)$ includes the estimation error p_e and is presented as follow.

$$\mathbf{p}_m = \mathbf{p} + \mathbf{p}_e \tag{3.7}$$

Then, $\mathbf{p}$ is a true location of the UE.

3. (Step 3) Notification by CAM: The location information estimated in the step 3 needs to be notified to the RNs. To reduce the control overhead, we propose notification utilizing CAM in V2X. The CAM includes vehicle location, speed, acceleration, and direction. The CAM is transmitted from the UE via NR-V2X [46, 47]. The typical message size of the CAM is from 350 to 400 bytes. The transmission cycle of the CAM is from 100 to 1000 ms.

4. (Step 4) Relay-beam configuration on access side: After receiving location information from the UE, the RNs calculates the direction of analog beamforming that should be aimed at the UE. The direction is geometrically determined by using the UE and the RN location information according to the following formulas. For simplicity, a two-dimensional plane is assumed, and only azimuth angle is described.

$$\phi = \arctan\left(\frac{y_1 - y_0}{x_1 - x_0}\right) + \phi_0 \tag{3.8}$$

$$i \in \underset{0 \leq n \leq N, n \in \mathbb{N}}{\arg\min} \left(\left|\tilde{\phi}_n - \phi_0\right|\right) \tag{3.9}$$

Where coordinates (x_0, y_0) and (x_1, y_1) are RNs and UEs location, respectively. An angle ϕ_0 is UE-side antenna boresight of the RN. The RN can know (x_0, y_0) and ϕ_0 in advance. Based on ϕ calculated in Equation (3.8), the beam number i with the closest beam angle to ϕ is selected. In Equation (3.9), N is the number of UE-side beam candidates on the RN. The steps 1-4 described above belong to the the first phase of

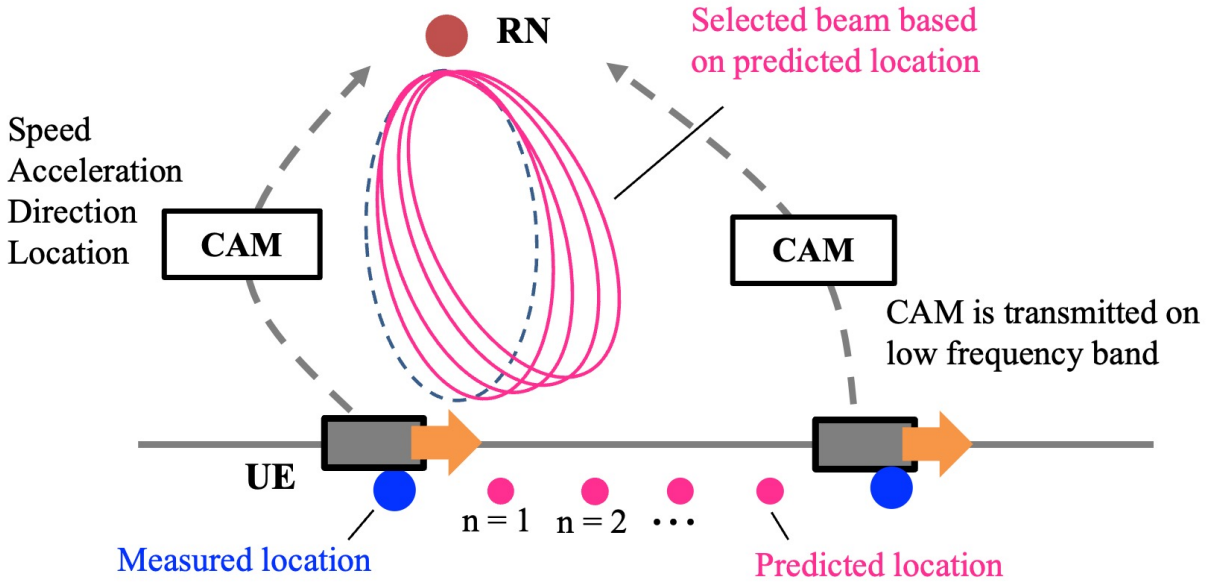

Figure 3.7 Relay-beam tracking utilizing UE location, speed, acceleration and direction contained in CAM

the proposed method which computes beamforming weight of RNs. Through the first phase, new coverage and paths are formed between the BS and the UE via the RNs. The final step computing beamforming weights of BS and UE in the second phase is explained below.

5. (Step 5) Analog and digital weight control on the BS and the UE: The final step, which is corresponding to the second phase of the proposed method, is processing at the BS and the UE. Since the processing can be applied independently from the relay-beam selection, the processing can be performed based on a procedure specified the standard such as 5G NR [48]. However, since massive analog-relay MIMO utilizes multiple beams, additional consideration is required to beam selection at the BS and the UE. To select multiple beams to maximize capacity, a sequential quasi-optimization procedure as in [38] is considered in this paper.

3.4.2 Relay-beam tracking

Beam tracking is also an important issue in analog relay beamforming. In many cases, the BS tracks the beam using RNs after the beam search. However, the analog RN cannot utilize RS because it has no signal processing for millimeter-wave bands. As mentioned above, since the transmission cycle of the CAM is relatively long, only the proposed beam search causes the location error due to the UE mobility and reduces the gain from massive RNs. Therefore, a relay-beam tracking method, which utilizes the UE information contained in the CAM, is proposed. The RN can acquire the UE's location $p_m(t_0)$, speed $v(t_0)$, acceleration $a(t_0)$ and direction $\tilde{d}(t_0)$ from the received CAM. Here, t0 means the time when these values are measured. From this information, it is possible to predict the location of the UE. The predicted location $\tilde{p}(t)$ can be calculated from Equation (3.10).

$$\tilde{\mathbf{p}}\left(t_0 + nt_p\right) = \mathbf{p}_m\left(t_0\right) + nt_0\left(v(t_0) + \frac{1}{2}a(t_0)nt_p\right)\hat{\mathbf{d}}(t_0), n \in \mathbb{Z}, n \geq 0 \tag{3.10}$$

Then, t_p is the prediction cycle. The UEs direction from the RN can be estimated from Equation (3.8) and (3.10), and the relay beam can be updated as below.

$$\phi = \arctan\left(\frac{\tilde{p}_y(t + nt_p) - y_0}{\tilde{p}_x(t + nt_p) - x_0}\right) + \phi_0 \tag{3.11}$$

3.4.3 Overhead analysis

The purpose of the proposed method is to reduce overhead in massive analog-relay MIMO. To focus on the relay-beam search in the step (4) described in the previous section, analog-beam search on the BS and the UE is ignored. It assumes they know the optimal beam for each RN. As a conventional method, we introduce a network-driven exhaustive search. Here, it is assumed that the beamforming settings on the RN is ideally performed using the control signal from the BS. Assuming sequential quasi-optimization procedure, the cumulative overhead time To is expressed as follows.

$$T_0 = T_{rs}L_{rn}\sum_{n=1}^{N_s}(K - n + 1) \tag{3.12}$$

Then, T_{rs} is a length of the reference signal for beam search, and N_s is the number of streams. L_{rn} is the number of beam candidates on the RN. The above formula expresses the

overhead when the reference signals are continuously transmitted. In practice, the reference signal is transmitted intermittently, so the control time takes longer. Next, the proposed user-driven beam search of relay nodes is discussed. Since the UE only broadcasts its self-estimated location information, the overhead time is given by the following equation.

$$T_0 = T_{msg} \tag{3.13}$$

Then, T_{msg} is length of a message including location information sent by the UE. From Equation (3.13), the proposed method has constant overhead regardless of the number of RNs around the UE, and it is an effective method for massive analog-relay MIMO that utilizes many RNs. In addition, all the overhead of the conventional method always occurs in mmWave bands where data communication is performed, while the overhead of the proposed method can alternatively be consumed in different frequency bands.

3.5 Simulation

3.5.1 Simulation configuration

The proposed method was evaluated by computer simulation. Figure 3.8 and 3.9 show the simulation model. BS and UE are deployed, and 12 RNs are placed between the BS and the UE. The RNs are placed at equal intervals on a straight line as shown in Figure 3.8. There is always LOS between the BS and the RNs, and between the RNs and the UE. On the other hand, there is always NLOS between the BS and the UE. It is assumed that the antenna boresight on the BS and RNs (UE side) are $+x$ direction, and the antenna boresight on the RNs (BS side) and the UE are $-x$ direction. Elevation angle of antenna tilt is set to zero in all nodes. Table 3.3 lists the simulation parameters. For the analog beam direction, rough beamforming with 15-degree increments and fine beamforming with 1-degree increments were evaluated. Rough beamforming is often used for initial access, but it is a factor of characteristic deterioration because the beam direction is not properly directed to the UE. In recent years, a phased array antenna module that can adjust the beam direction in 1-degree increment has also been developed [49], so we basically considered fine beamforming in the evaluations. The antenna polarization was single polarization. SVD-MIMO is applied as digital processing in the BS and the UE. We assume that the CSI can be estimated ideally.

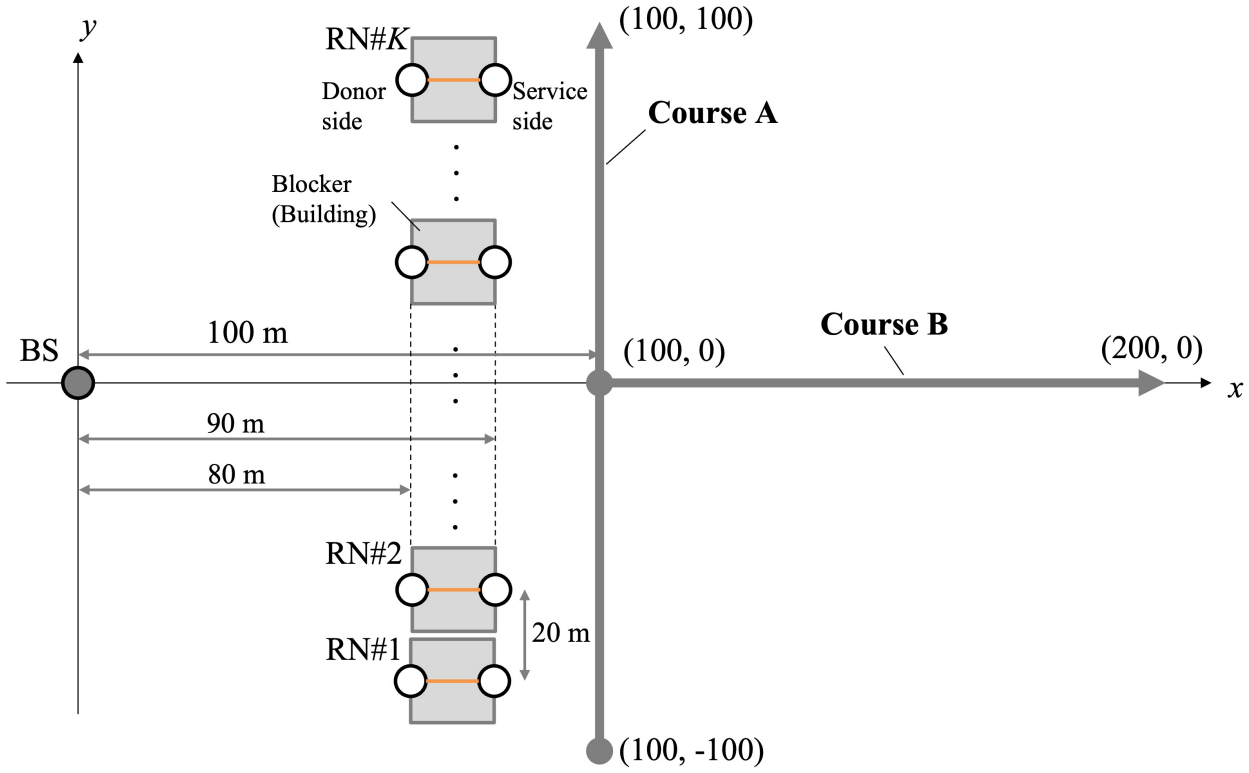

Figure 3.8 Simulation model (Top view)

Table 3.3 Simulation parameters

Parameter #	Value
Carrier frequency	28 GHz
Transmit power	30 dBm @ 100 MHz
Number of BS antennas	64 (V: 8, H: 8)
Number of BS beam candidates	64 (V: 8, H: 8)
Number of UE antennas	8 (V: 1, H: 8)
Number of UE beam candidates	8 (V: 1, H: 8)
Beam range	±60 deg. (Both V/H directions)
Antenna tilt	0 deg. (in all antennas)
Noise power density	-174 dBm/Hz
Noise figure in UE and RN	5 dBm/Hz
Number of RN antennas (Backhaul) L_r	64 (V: 8, H: 8)
Number of RN antennas (Access) L_t	128/64/32 (V: 8, H: 16/8/4)
Number of RNs	12
Amplifier gain	40 dB
Pathloss model	3GPP TR 36.910 (UMi)
Antenna array type	Planar linear array
Analog beam weight	Steering vector
MIMO signal processing	SVD

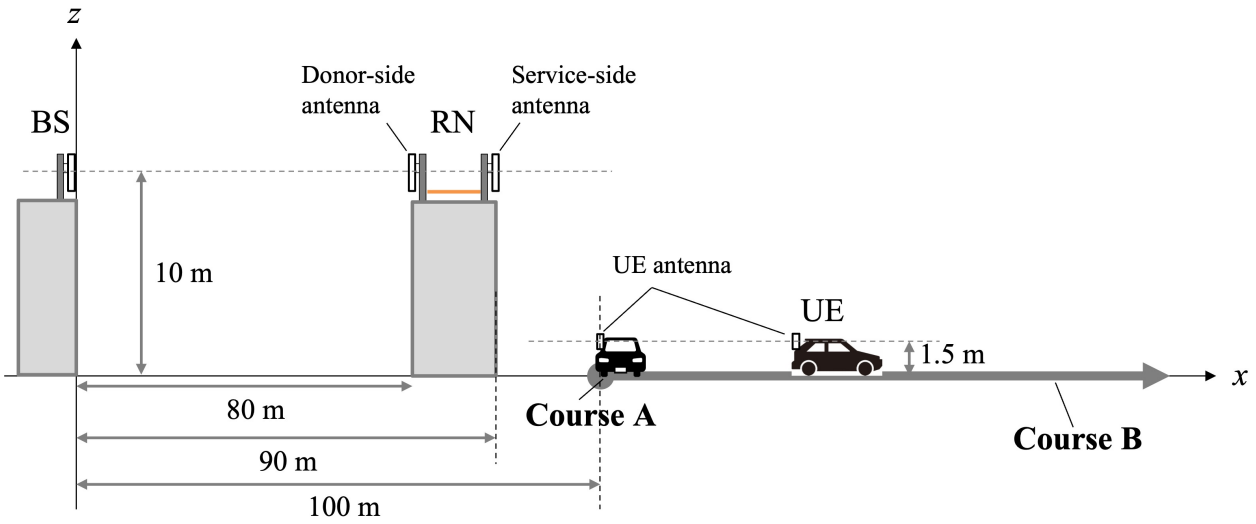

Figure 3.9 Simulation model (Side view)

3.5.2 Massive analog-relay MIMO with the user-driven relay beamforming

Figures 3.10 and 3.11 show the results of massive analog-relay MIMO with the proposed method. The results show that the proposed method can improve the rate in the massive analog-relay MIMO. Here, it is assumed that all RNs receive ideal location information from the UE. Also, the number of streams is fixed without rank adaptation, and the power is equally distributed to each stream. The average rate is calculated based on Equation (3.6), and the average value of 100 samples is plotted at each point.

Figure 3.10 is shown at UE coordinates $x = 100m$, $-100m \leq y \leq 100m$. The average rate is improved in the range where the RNs are installed (from -70 m to +70 m). The RNs extend coverage and improve overall performance. Comparing the 1-stream and the 4-stream transmission near the coordinates $(100, 0)$ of the UE, we can see that the improvement is about 72 % compared to the 1-stream case. The reason is improvement of spatial multiplexing by passing through multiple RNs. On the other hand, when y = -100 m or + 100 m, the benefits of spatial multiplexing are hardly obtained because the directions of arrival of each route that passes through each RN are close to each other. It can be solved by distributing more RNs. Figure 3.11 shows the characteristics when the terminal position is $100m \leq x \leq 200m$,

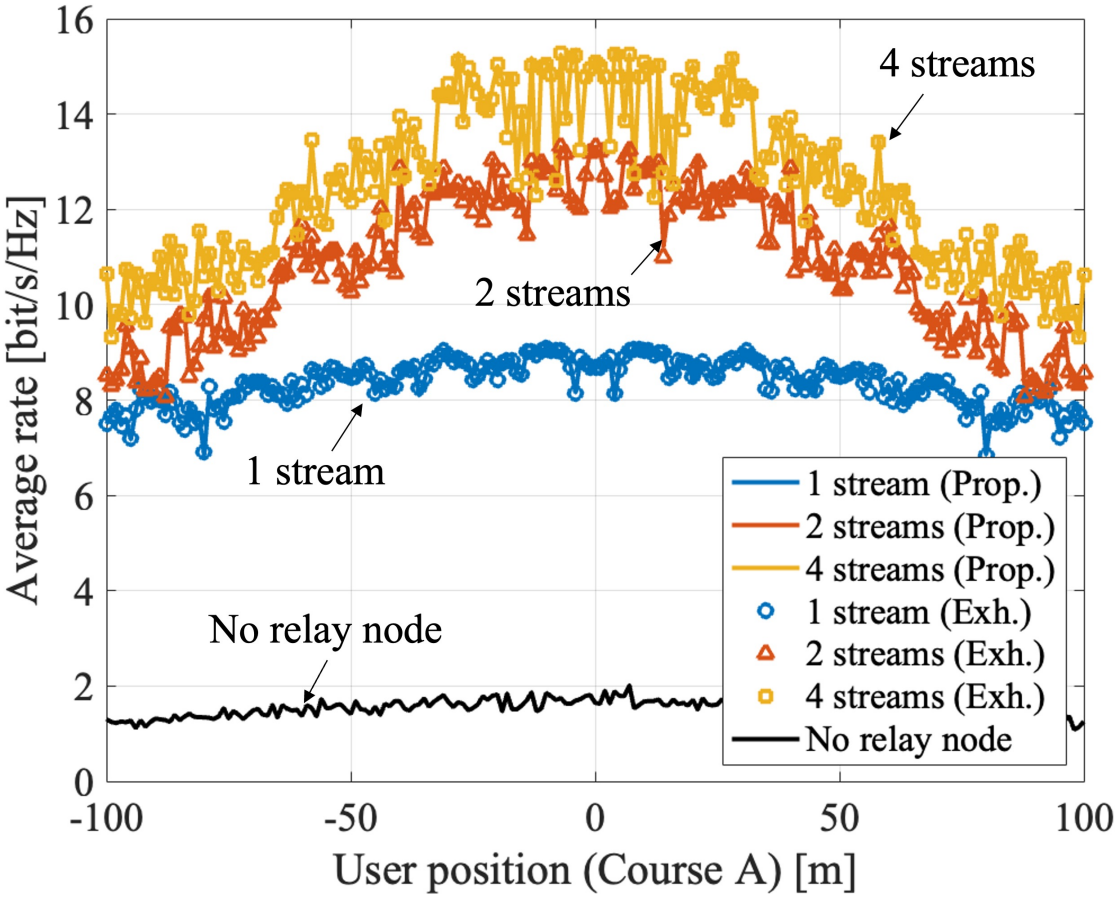

Figure 3.10 Average rate of massive relay MIMO with the user-driven relay beamforming in the course A

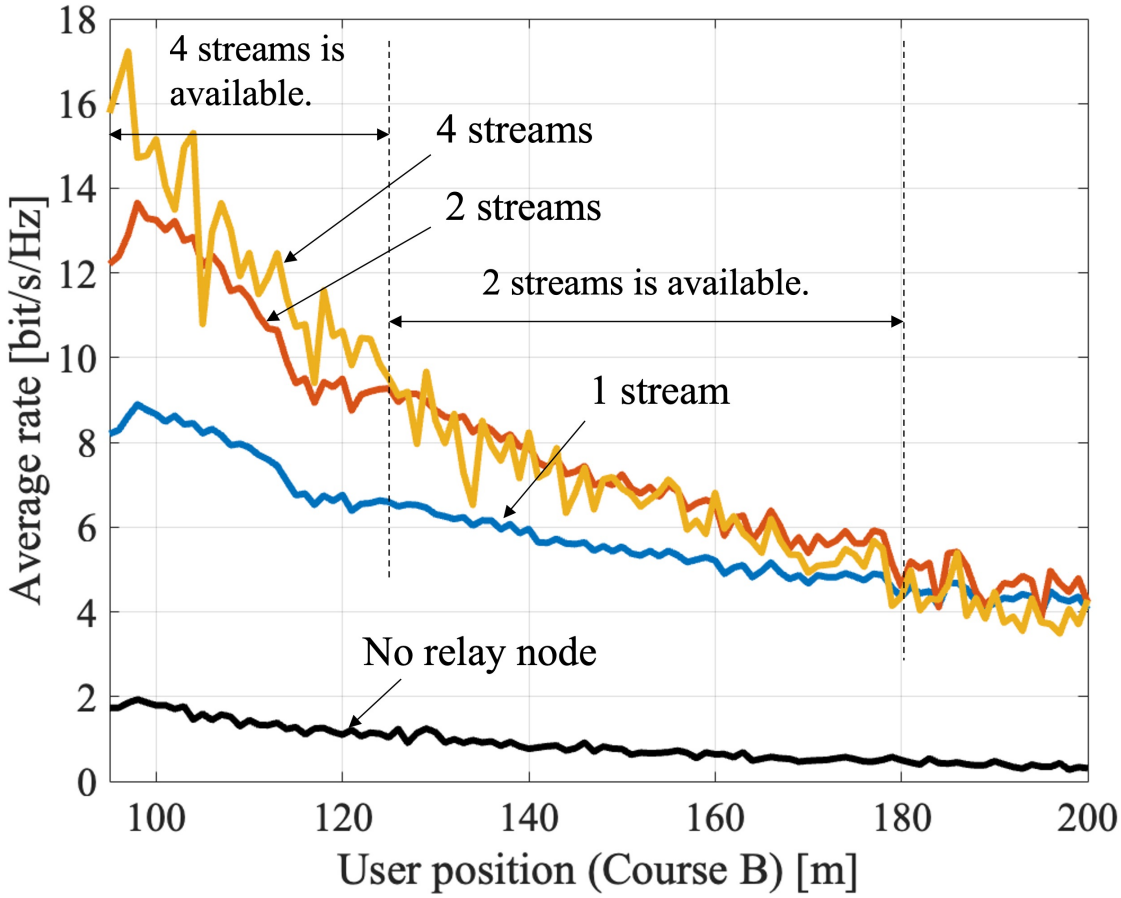

Figure 3.11 Average rate of massive relay MIMO with the user-driven relay beamforming in the course B

$y = 0m$. As in Figure 3.11, the shorter the distance between the UE and the RN, better the capacity. If V2X are assumed, the RN is expected to be installed in a roadside unit, so the distance between the relay node and the UE is about 5 to 20 m. Therefore, the benefits of massive relay MIMO can be fully obtained in V2X use cases.

We evaluated the overhead reduction by the proposed method using Equations (3.12) and (3.13). We considered a 5G NR reference signal with 120 kHz subcarrier spacing (including cyclic prefix), T_{rs} as 17.84 μs, and CAM transmission overhead (T_{msg}) as 1 ms. The estimated overhead is sufficient since the CAM size is less than 1000 bytes [50]. The cumulative overhead consumed to explore the relay beams is shown in Figure 3.12. In the exhaustive search, the overhead increases as the number of RNs. This is because the number of RNs is directly proportional to the number of beam candidates to search. In addition to that, the exhaustive search for fine beamforming is not realistic. On the other hand, the overhead of the proposed method is constant regardless of the number of RNs. Therefore, the proposed method can benefit the massive analog-relay MIMO while reducing overhead.

3.5.3 Impact of location error

Since the proposed method uses location information, the location error affects the rate. The location error is caused by UE positioning accuracy, control delay and control cycle. The UE positioning accuracy depends on the location estimation method. The control delay is the time interval between the location estimation by the UE to the beam setting by the RN. The control cycle is the update cycle of the UE location. If the control delay and cycle is short, the update of the position information is fast, and if it is long, the update of the position information is slow. The control delay and cycle are related to UE mobility. If the UE is fixed, no location error due to the control. However, location error plays a significant role if we consider UE with high mobility.

3.5.3.1 Impact of UE positioning accuracy

The impact of positioning accuracy on the proposed method is evaluated. Here, the positioning accuracy is defined as an average of the location estimation error $\|p_e\|$. It is assumed that the p_e follows a normal distribution with independent x- and y-coordinates. Then, the $\|p_e\| = \sqrt{x_e^2 + y_e^2}$ follows Rayleigh distribution. Therefore, the relationship between the positioning accuracy α and the standard deviation σ of p_e is given below.

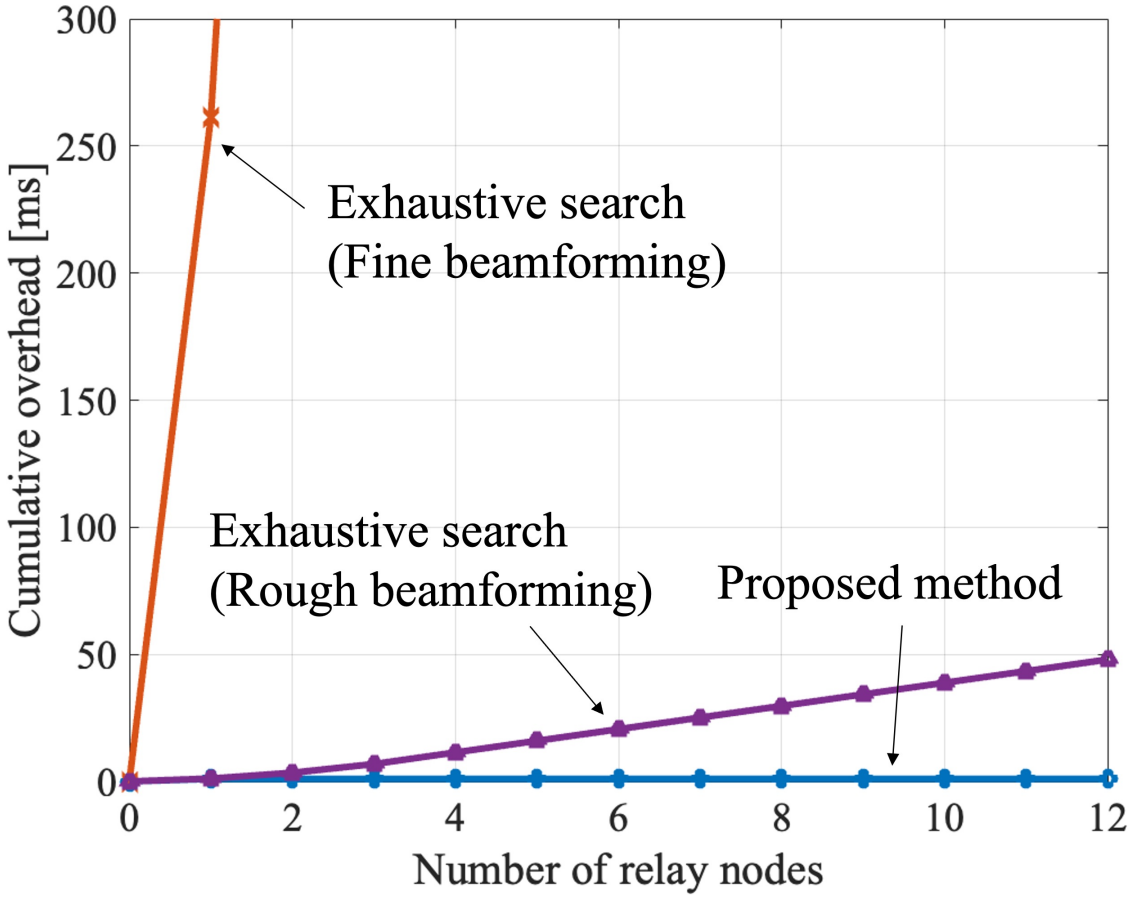

Figure 3.12 Cumulative overhead consumed to determine the relay beam on the RN access side

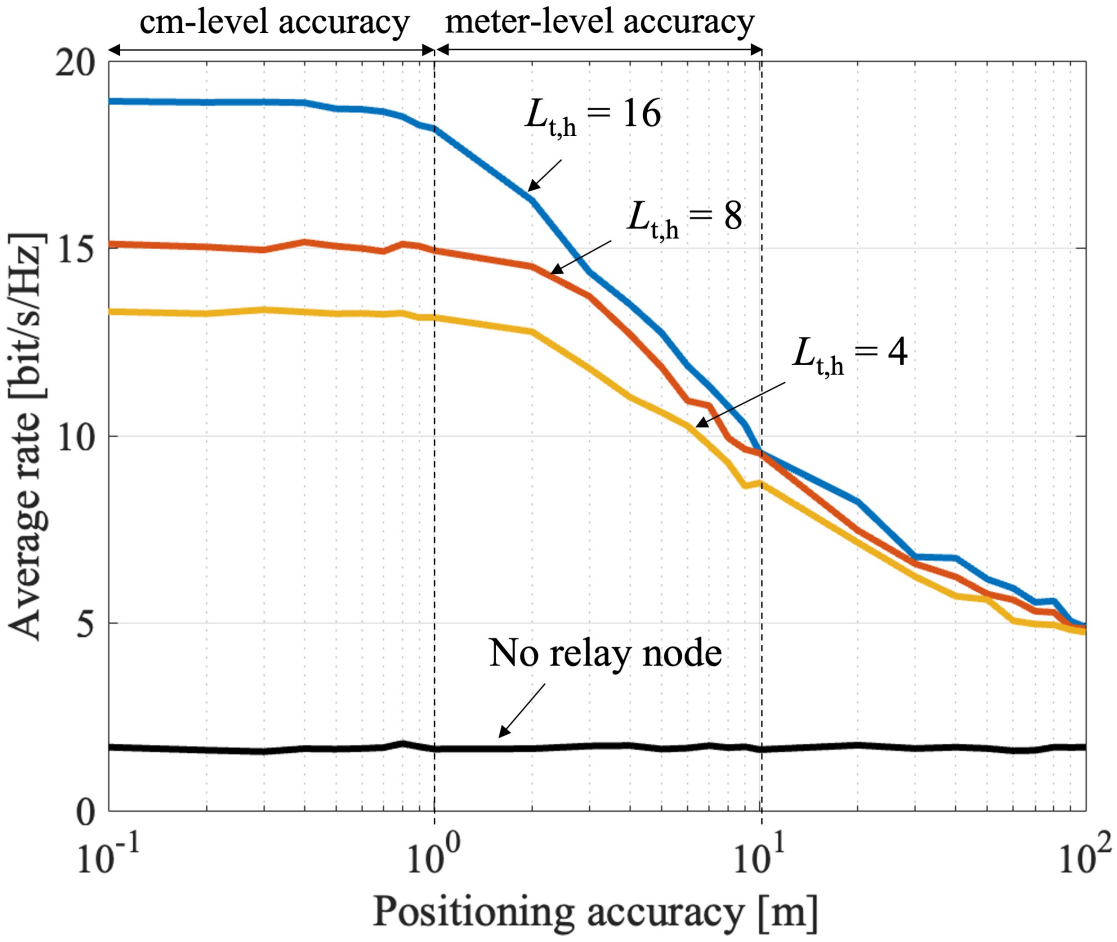

Figure 3.13 Impact of location estimation error on the UE with high-precision positioning

The impact of the positioning accuracy is shown in Figure 3.13. Here, the UE location is fixed and placed in $(100, 0)$. The number of streams is set to four. As the positioning accuracy gets worse, the average rate is also reduced. However, if the centimeter (cm)-level positioning accuracy is satisfied, the rate hardly drops. LiDAR can satisfy this condition because it has cm-level accuracy. The rate tends to drop at meter-level accuracy, however relatively high rates can be maintained. Therefore, even if GNSS is applied, the effect of the proposed method can be obtained.

To mitigate the impact of positioning accuracy, another approach is to broaden the beam width. Therefore, a comparison was made with different beam widths. The beam width was adjusted by changing the number of relay antennas (access side) in the horizontal direction $L_{t,h}$. When the RN has wider beam width, the impact of positioning accuracy is mitigated, however, the requirement for meter-level positioning accuracy remains. Furthermore, as the beam width becomes wider, the beam gain becomes small, so the overall rate is reduced. Therefore, it is desirable to combine the proposed method with a highly accurate positioning method. The results show that the proposed method works effectively by utilizing cm-level positioning methods such as LiDAR, which are expected to be available in future V2X terminals.

3.5.3.2 Impact of location error due to UE mobility

The effect of the proposed relay beam tracking is evaluated in this subsection. To focus on the control of the RN, the control latency for searching the beam of the BS and the UE is ignored. In the simulation, we assume that the UE estimated its location with no error at $(100, 0)$. Furthermore, the effect of wider beam width is also evaluated. The result is shown in Figure 3.14. Here, the UE speed and the beam control latency are v and T_c, respectively. Without the compensation of the mobility error, the rate decrease rapidly as vT_c becomes larger. As the beam width of the RN becomes narrower, the impact of the mobility error is relatively smaller. However, the overall rate is reduced due to the lower beam gain. The proposed method can suppress the rate degradation without reducing the beam gain. The RN can effectively track the beam by utilizing the information contained in the CAM.

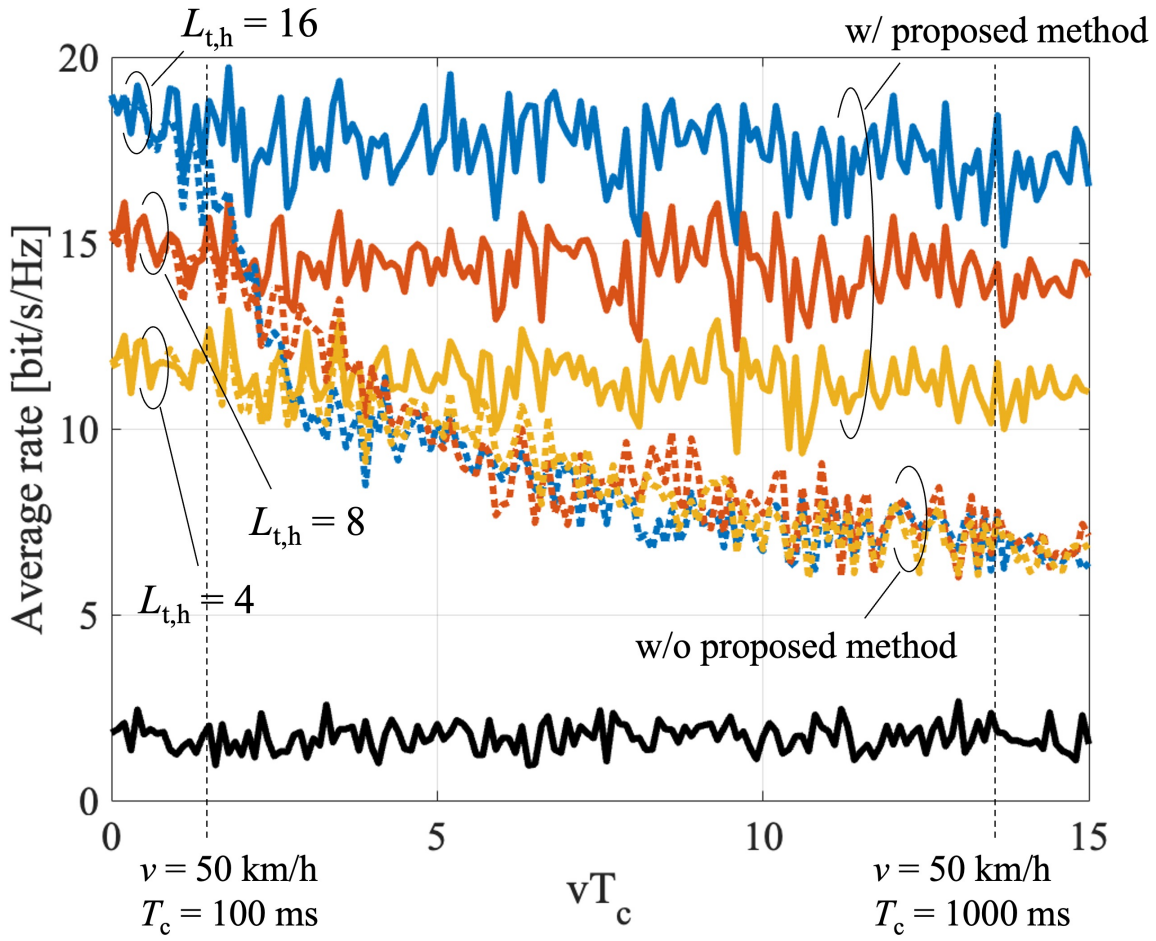

Figure 3.14 Average rate of the proposed relay-beam tracking

3.6 Summary

This chapter proposed a user-driven relay beamforming method of massive analog-relay MIMO for V2X applications. The proposed method enables relay beam search and tracking in analog relays and can reduce the overhead of beam control. To reduce the overhead, the RNs utilize UEs location, speed, velocity, acceleration, direction. The UE information is notified by using CAM. Simulations show that the proposed method can benefit from massive analog-relay MIMO and significantly reduce the overhead. One result indicates the massive analog-relay MIMO with the proposed method can improve the rate by about 72 % due to the multiplexing gain of 4-streams MIMO. Then, the overhead is CAM transmission only. The accuracy of the location information, the control period, and the effects of UE mobility are also evaluated. The result clarifies that it is desirable for the terminal to have cm-meter level positioning when applying the pro-posed method. Further, we show that the proposed relay beam tracking method works effectively for the impact of UE mobility and the cycle of UE location update.

Chapter 4

Frame structure for achieving time-resource redundancy

4.1 Motivation

Time-resource redundancy means signal retransmission in wireless communication systems. Retransmission can reliably send signals and improve reception quality. Different from spatial resource redundancy, time resource redundancy is suitable for improving reception quality even a little. In future radio access networks, it is desirable to realize URLLC in higher frequency bands. Therefore, the purpose of this study is to achieve URLLC requirements by making time resource redundancy. This chapter designs frame structure for time-resource redundancy and verifies the feasibility of URLLC based on field experimental trials.

The requirements for URLLC have been discussed by several organizations [52, 53, 54]. In the 3GPP, as a reliability requirement, the packet success probability of $1 - 10^5$ ($= 99.999\%$) with the user-plane latency of less than 1 ms, is defined [54]. The user-plane latency is a sum of the transmitter processing delay including frame alignment and possible queuing delay, transmission delay, and receiver processing delay [55]. Since the Transmission Time Interval (TTI) is set to 1.0 ms in LTE-Advanced, it is difficult to satisfy the latency requirement using the LTE-Advanced framework when the processing delay at a transmitter and receiver is taken into account. To satisfy the reliability requirement of URLLC, it is important to both shorten the processing delay and reduce the transmission time from the viewpoint of the air interface. To this end, a new frame structure has been discussed for NR in order to reduce the transmission time. Specifically, a mini slot based on the LTE-Advanced frame

structure [56,57] and a wider subcarrier spacing [58,59] with NR have been proposed as frame design for URLLC. The above-mentioned studies are concept-level proposals or estimations based on computer simulations.

In our trials, we first adopt new TDD frame structures including the subcarrier spacing of 30 kHz to verify the contribution to low latency (similar to the NR design under discussion in the 3GPP). Then, to verify ultra-reliability, another frame structure is applied. This second frame structure has the subcarrier spacing of 60 kHz and performs A/N-less retransmission. The performance of these frame structures is evaluated in a large-scale field trial, which aims to achieve a low user-plane latency of 0.5 ms and a high reliability of 99.999% packet success probability within 1 ms user-plane latency. The approach of frame design that shortens the delay while making the time resource redundancy can be applied regardless of the frequency band. The experiment was conducted using the 5 GHz band to avoid the hardware imperfection in the mmWave band equipment affecting the packet success rate.

The rest of this paper is organized as follows. In Section 4.2, we describe the definition and the requirements for URLLC. Sections 4.3 and 4.4 introduce the new frame structures and estimate the delays. Application of A/N-less retransmission is also described in Section 4.4. The trial environment is described in Section 4.5. The results of the field trial are presented in Section 4.6. In this section, we show the reliability, the packet success ratio, and the latency measured at several measurement locations. Finally, we conclude the paper in Section 4.8.

4.2 Definition and requirements

Toward 5G, the definition and requirements of Key Performance Indicators (KPIs) are discussed by the 3GPP in [54]. The definition and requirements for KPIs related to URLLC are described in this section.

4.2.1 User-plane latency

User-plane latency represents a one-way transmission delay between the transmitter and receiver. The 3GPP defines user-plane latency as the time it takes to deliver successfully an application layer packet/message from the radio protocol layer 2/3 Service Data Unit (SDU) ingress point to the radio protocol layer 2/3 SDU egress point via the radio interface in either the UL or DL directions, where neither device nor BS reception is restricted by discontinuous reception [54].

4.2.2 Reliability

The 3GPP defines reliability as the success probability of transmitting X bytes within a certain delay, which is the time it takes to deliver a small data packet from the radio protocol layer 2/3 SDU ingress point to the radio protocol layer 2/3 SDU egress point of the radio interface, at a certain channel quality. The packet success probability is defined as the ratio of the number of correctly received packets and total number of transmitted packets [54].

Given that there will be a variety of URLLC services in the future with different requirements, as a general target, the 3GPP sets the target reliability as achieving a success probability of $1 - 10^5$ ($= 99.999\%$) for the packet size of 32 bytes with a user-plane latency of less than 1 ms [54].

4.3 Frame structure in TDD LTE-Advanced

In the 3GPP LTE-Advanced specifications [62], OFDM is used as the DL multiplexing scheme. The subcarrier spacing is 15 kHz, and the OFDM symbol duration is 66.67 μs. The LTE frame structure for TDD is shown in Fig. 4.1. The LTE frame duration is 10 ms. The LTE frame is divided into 10 subframes, each of which is further divided into two slots. The subframe and slot durations are 1 ms and 0.5 ms, respectively. Each slot includes 6 or 7 OFDM symbols depending on the length of the cyclic prefix. Seven configurations with different ratios between the UL and DL subframes and different switching periods are specified in LTE-Advanced. Fig. 4.1 shows configuration #1 [63]. In resource allocation, a certain number of Physical Resource Blocks (PRBs) are allocated to a UE. In LTE-Advanced, since the minimum number of allocated PRBs is two per user, the minimum transmission time is 1 ms. Moreover, the sum of the BS and UE processing times, not including frame alignment, is estimated to be 2.5 ms [64]. Therefore, considering the BS and UE processing times, it is difficult to achieve the user-plane latency of 1 ms. Furthermore, we should consider retransmission used in this frame structure. As an indicator of latency with retransmission, the HARQ Round Trip Time (RTT) timer specifies the minimum number of subframes, which is expected by the UE, before a DL HARQ retransmission [63]. An example of the DL HARQ procedure is shown in Fig. 4.2. Considering the processing time and frame alignment time, the UE requires at least 4 ms as the interval between the DL transmission and the transmission of associated HARQ feedback. If the DL transmission is accomplished using subframe #0 as shown in Fig. 4.2, the UE can reply with the associated HARQ feedback using subframe #6 in the allocated UL channel.

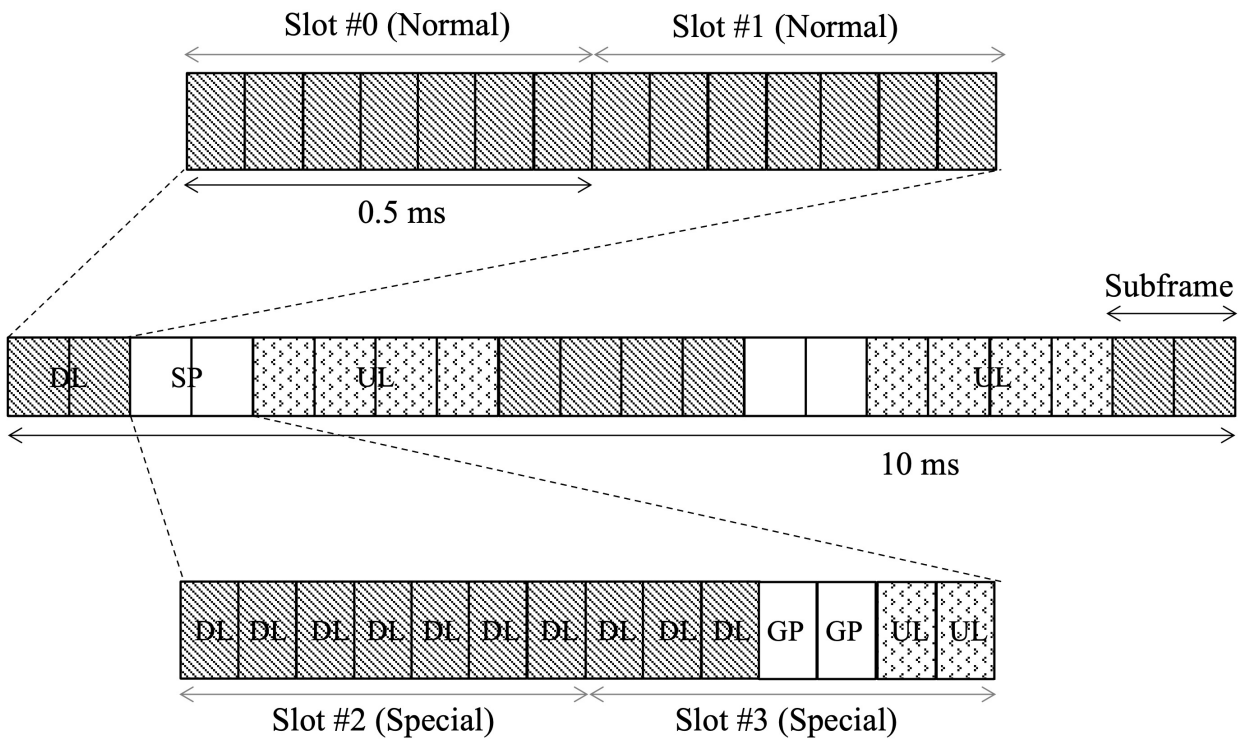

Figure 4.1 TDD LTE-Advanced frame structure

Therefore, the interval becomes 6 ms. The BS, which receives the HARQ feedback, also needs 4 ms to send the retransmission signal. In the case shown in Fig. 4.2, the BS can retransmit the DL signal in subframe #0 of the next frame. As a result, the HARQ RTT, which is specified as the minimum number of subframes before a DL HARQ retransmission, becomes 10 ms in this case. Therefore, with one retransmission, the user-plane latency becomes longer than 10 ms in many cases of the TDD LTE-Advanced frame structure.

4.4 Frame structure for time-resource redundancy

In this section, we describe two kinds of frame structures. The first one is a new frame structure, referred to as the type-I frame structure, to satisfy the URLLC requirement for a low user-plane latency of 0.5 ms. We then also study another frame structure, referred to as the type-II frame structure, to satisfy the URLLC requirement of high reliability, i.e., the

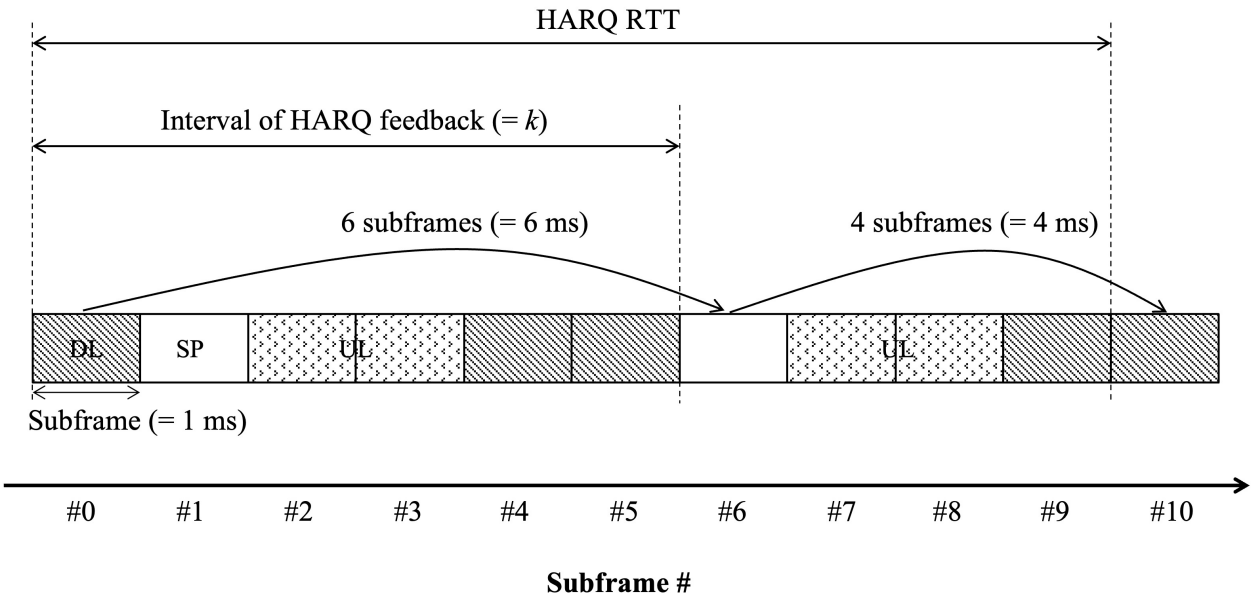

Figure 4.2 DL HARQ RTT and HARQ feedback timing for TDD

packet success probability of $1 - 10^5$ with a delay of less than 1 ms.

4.4.1 Frame structure for low-latency

We first focus on the frame structure used in the low-latency test. To achieve a user-plane latency of less than 0.5 ms, a shorter transmission time and shorter processing time are needed. As a result, the 3GPP has discussed and supported the 5G NR frame structure. A reduction in the transmission time can be achieved by employing fewer OFDM symbols and/or shorter OFDM symbol duration compared to LTE-Advanced. In this paper, we assume the latter approach. The frame structure for low latency is shown in Fig. 4.3. This structure has the same number of OFDM symbols with the frame structure of TDD LTE-Advanced; however, the subcarrier spacing is larger. The proposed frame structure for low latency has the subcarrier spacing of 30 kHz, and the OFDM symbol duration is 33.33 μs. The symbol duration is half that of LTE-Advanced. Thus, the transmission time becomes shorter for the same number of OFDM symbols.

In Table 4.1, we show the estimated processing time and transmission time described

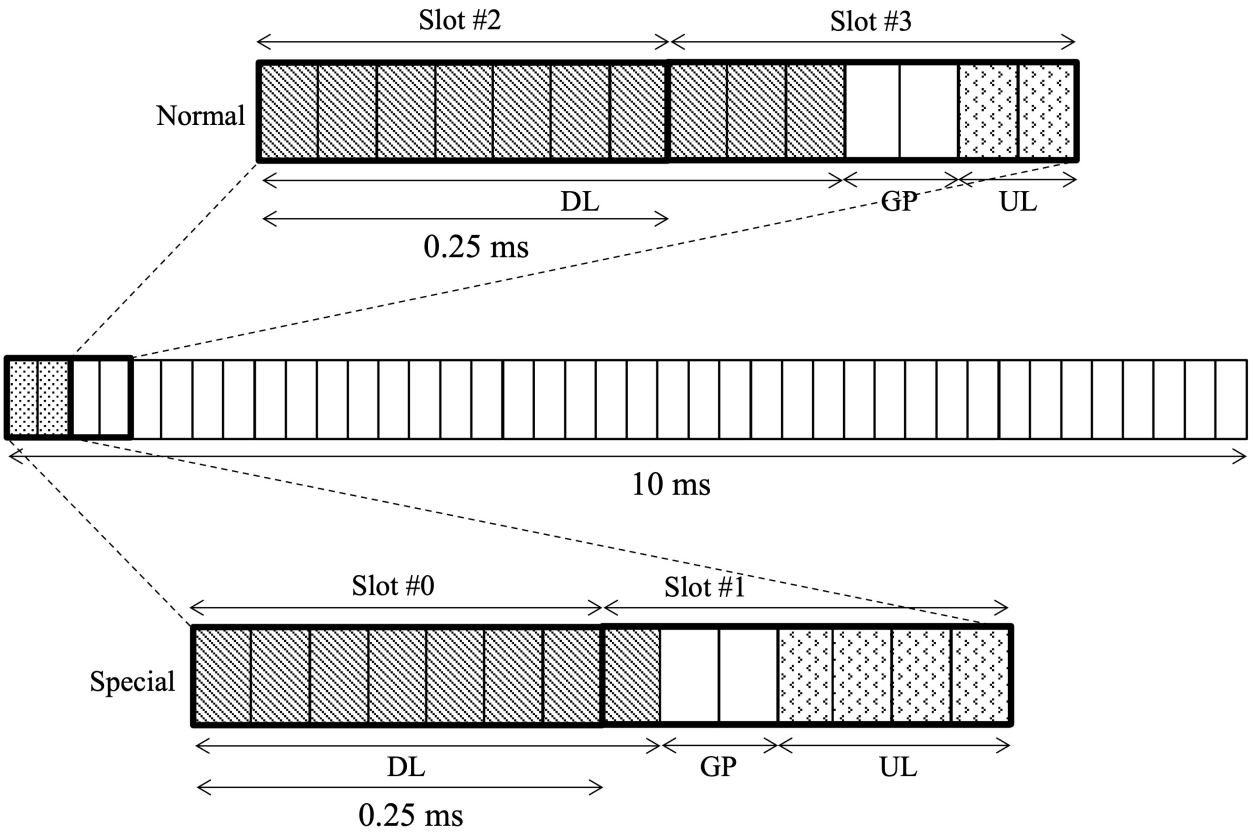

Figure 4.3 Type-I frame structure

Table 4.1 Delay estimation of type-I frame structure

	Delay Type	Typical value
a	BS DL processing time	230 μs
b	UE DL processing time	100 μs
t	Transmission time time (3 OFDM symbols)	100 μs
	User-plane latency (= a + b + t)	430 μs

in Section 4.6.1 using the type-I frame structure. The processing time is the average value obtained by measurement in our prototype test-bed. In the trials of the type-I frame structure, we use only the initial 3 OFDM symbols and a part of the carrier bandwidth to transmit data because we expect communications of control signals for low-latency services. Therefore, the transmission time becomes 100 μs (= 33.33 μs Œ 3 OFDM symbols). A user-plane latency of 0.5 ms or less is achieved by a shorter OFDM symbol duration and faster signal processing.

4.4.2 Frame structure for low-latency ultra-reliability

We discussed the frame structure to achieve 0.5 ms user-plane latency in the previous section. The frame structure can achieve low latency, however, it is not designed to satisfy the reliability requirement of 1-10^5 (99.999%) packet success probability within 1 ms user-plane latency. In this section, to satisfy the reliability requirement, we investigate a new frame structure that is different from the type-I frame structure. The new frame structure is called the type-II frame structure and is shown in Fig. 4.4.

In the new frame structure, we adopt a wider subcarrier spacing than the type-I frame structure in order to reduce further the transmission time to within 1 ms and allow for more time for repetition transmission to achieve higher reliability. Moreover, a larger numbers of transmitter and receiver antennas (8 at BS and 2 at UE) are used. Although a larger number of antennas needs longer processing time to decode the received signal, it can improve the packet success probability. The adopted subcarrier spacing is 60 kHz, and the OFDM symbol duration is 16.67 μs. The frame length is 10 ms and the frame is divided into 40 slots. The slot duration is 0.25 ms with 14 OFDM symbols including 6 DL symbols, 6 UL symbols, and a guard period (GP). The first two slots of each frame are combined in order to transmit additional signals, e.g., a synchronization signal in the DL slot and random access channel (RACH) preambles in the UL slot. The duration of this specially designed slot is 0.5 ms

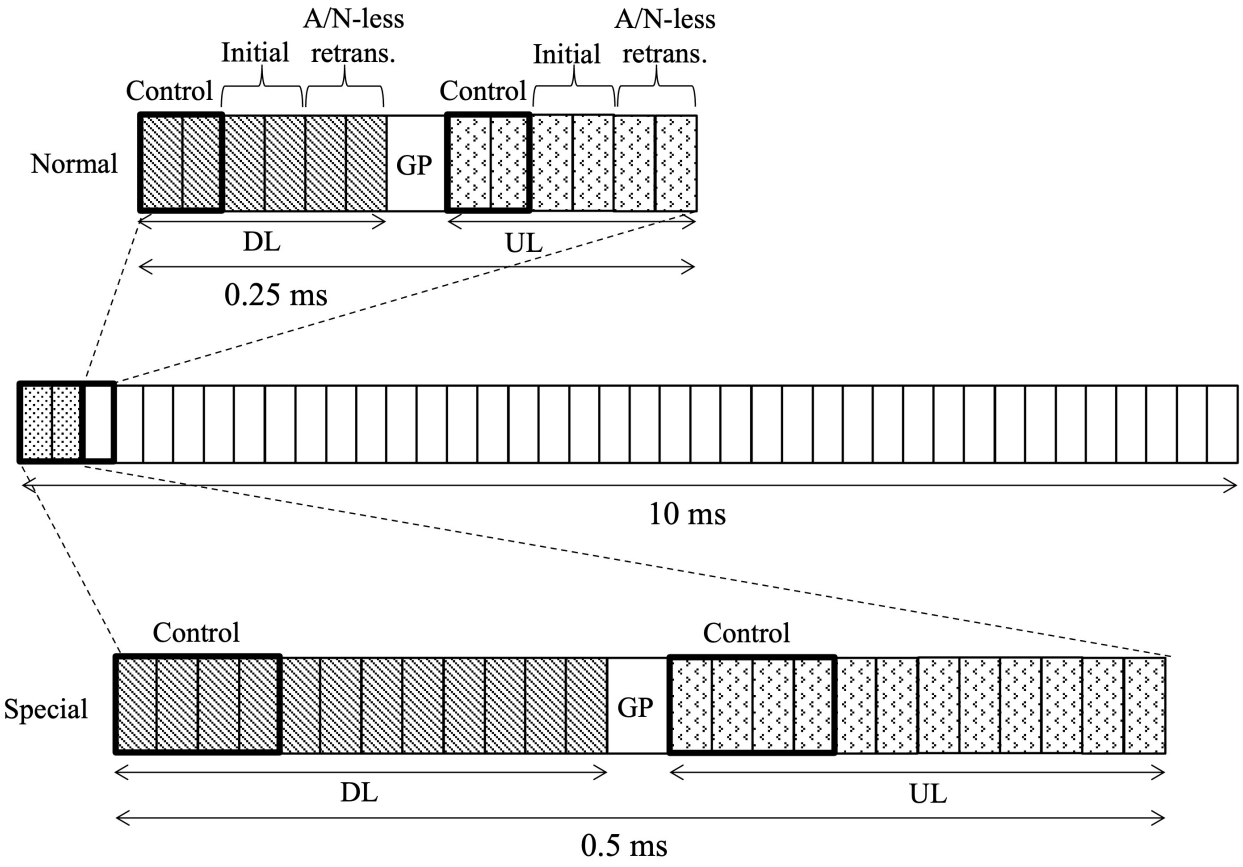

Figure 4.4 Type-II frame structure

Table 4.2 Delay estimation for type-II frame structure.

	Delay Type	Typical value
a	BS DL processing time	175 μs
b	UE DL processing time	240 μs
c	UE UL processing time	195 μs
d	BS UL processing time	305 μs
t	Transmission time time	110 μs

(special slot hereafter). Each slot is divided into a DL part and UL part. Furthermore, the frame structure adopts a self-contained structure and A/N-less retransmission method to reduce the latency imposed by retransmission. The self-contained structure includes all radio-related transmissions, such as the UL and DL control, data, and receiver feedback signals, within each single slot [63]. Since the structure can feedback an ACK or NACK signal using the next slot, it is possible to shorten the total transmission time including retransmission time. Thus, each slot of the new frame structure is divided into the DL and UL parts. On the other hand, A/N-less retransmission can improve reliability. In this method, the transmitter is pre-configured to send the same transmission signal multiple times irrespective of receiving the ACK or NACK feedback from the receiver [62]. Although the A/N-less retransmission reduces the resource utilization efficiency since the same signal is redundantly transmitted, it improves the packet success probability while achieving lower latency compared to A/N-based retransmission. In many URLLC applications, since priority is given to reliability over the data rate, A/N-less retransmission represents an attractive method for URLLC. In Table 4.2, we show the estimated processing time and transmission time described in Subsection 4.6.2 using the type-II frame structure. Since these processing times include the frame alignment time, these values actually fluctuate with time. In addition, there is a difference between the DL and UL processing times because the processing time increases with the number of receiver antennas. The transmission time is the sum of the symbol duration and the propagation delay.

The user-plane latency using the frame structure is estimated in Table 4.3 assuming no retransmission and a normal slot. The user-plane latency values shown in Table 4.3 are typical. Actually, these values depend on the waiting time before transmission. The user-plane latency in the DL and UL is 525 μs and 610 μs, respectively. If the special slot is used, the user-plane latency increases by 250 μs in both cases. Therefore, the user-plane latency

Table 4.3 User-plane latency for type-II frame structure

Latency	Typical value	Note
DL user-plane latency	525 μs	= a + t + b
UL user-plane latency	610 μs	= c + t + d

for the type-II frame structure is less than 1 ms and thus within the latency budget required for reliability. However, it does not satisfy the URLLC user-plane latency requirement of 0.5 ms. The processing time for the type-II frame structure is longer than that for the type-I frame structure due to two reasons. The first reason is the difference in the size of the PRB between the type-I and type-II frame structures. The type-II frame structure has a larger PRB. The number of PRBs for the PDSCH is 27.5 with 330 subcarriers, while the type-I frame structure has 14 PRBs with 168 subcarriers. The second reason is the difference in the number of antennas shown in the next section.

Table 4.4 summarizes the user-plane latency estimated in the DL and UL with one and multiple Transport Blocks (TBs). When a packet exceeds the TB size depending on the selected Modulation and Coding Scheme (MCS), the packet is divided into several TBs. Then, several slots are used to send the packet because one TB is transmitted using one DL or UL slot. As a result, the latency exceeds the estimated values in Table 4.3. In Table 4.4, a normal slot is assumed for transmission. Since the normal slot length is 250 μs, the user-plane latency increases by 250 μs for each additional TB. Also when the special slot is used, the user-plane latency increases by 250 μs from the value shown in Table 4.4, because the special slot length is 500 μs. Furthermore, A/N-based retransmission incurs longer latency than that given in Table 4.3. When A/N-based retransmission occurs, then the HARQ RTT, which is 750 μs in the normal slot, is added to the user-plane latency. From the above, we find that the user-plane latency can still be within 1 ms for up to two TBs without A/N-based retransmission. When a packet is divided into more than three TBs or A/N-based retransmission occurs, the user-plane latency exceeds 1 ms. Considering the special slot, up to only one TB can satisfy the requirement. If a packet is segmented, the user-plane latency exceeds 1 ms in this case.

Table 4.4 User-plane latency with packet segmentation and ACK/NACK-based retransmission

# of retrans.	# of TBs	DL user-plane latency	UL user-plane latency
0	1	525 μs	610 μs
0	2	775 μs	860 μs
0	3	1025 μs	1110 μs
1	1	1275 μs	1360 μs
1	2	1525 μs	1610 μs
1	3	1775 μs	1860 μs

4.5 Field experiments

The trial configuration is described in this section. The field experimental trial was conducted in an urban area in Yokohama, Japan.

4.5.1 Trial environment

Figure 4.5 is a picture of the trial environment. The picture was taken in the area where the BS was installed. We measured the performance at points A, B, and C. The Signal-to-Noise Ratio (SNR) is measured using a DeModulation Reference Signal (DMRS) that is transmitted using SFBC. Since the number of transmission antennas of the trial is different between the DL and UL, the difference in measured SNR between DL and UL depends on not only on transmit power but also on radio channels between transmitter and receiver antennas. With multiple transmission antennas used to transmit DMRS, the measured SNR at UE side includes an additional gain that depends on the channel condition and thus on the location of UE. In this trial setup, the maximum gain is 6 dB in DL and 0 dB in UL. Examples of the measured SNR are as described next. At point A, the distance between the BS and the UE (BS-UE distance) is approximately 330 m and the SNRs in the DL and UL are approximately 26 dB and 20 dB, respectively. At point B, the BS-UE distance is approximately 880 m and the DL and UL SNRs are approximately 11 dB and -2 dB, respectively. Only point C is NLOS. The BS-UE distance is approximately 350 m and the DL and UL SNRs are approximately 24 dB and 11 dB, respectively.

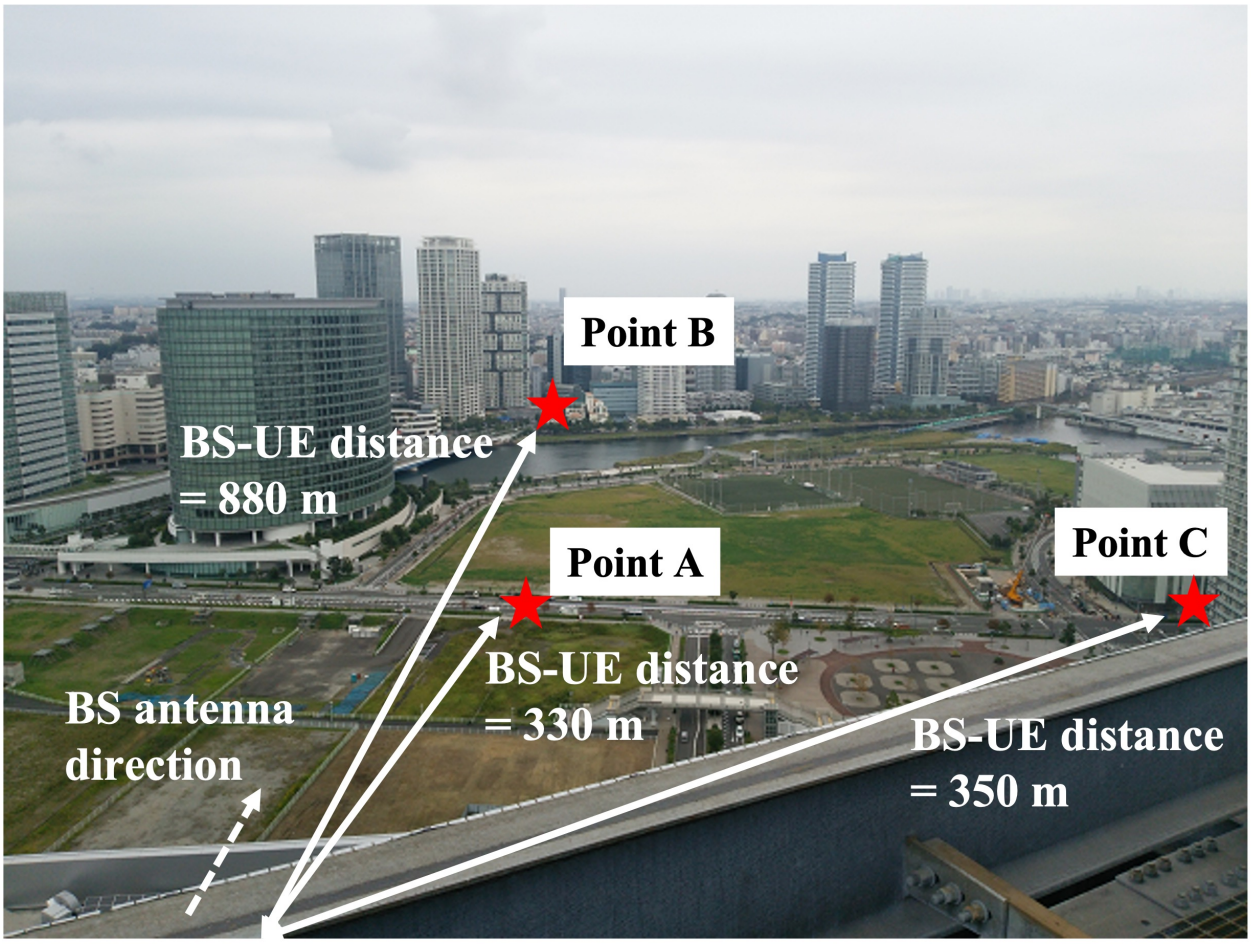

Figure 4.5 Trial environment and measurement locations

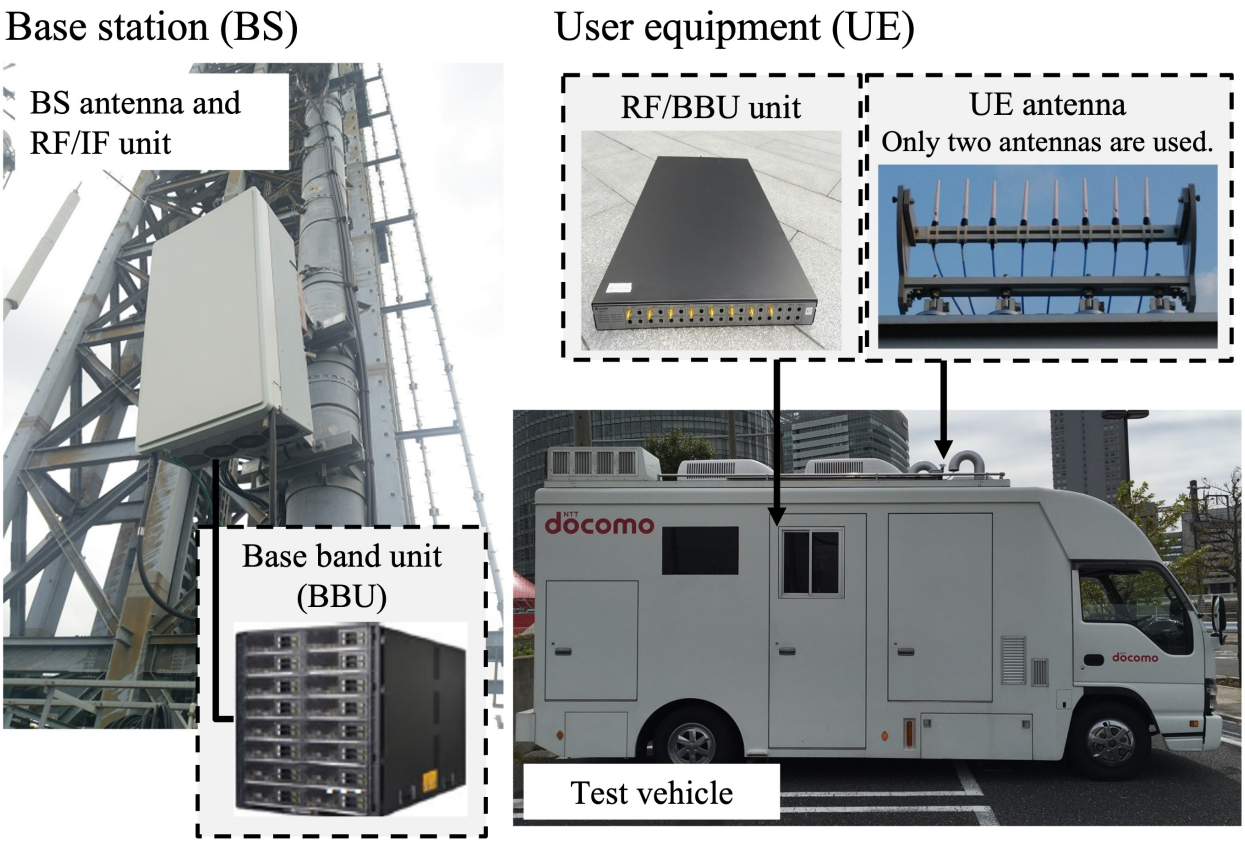

Figure 4.6 Experiment hardware.

4.5.2 Experiment hardware

Figure 4.6 shows the experiment hardware. On the BS side, the Radio Frequency Unit (RFU) and the inter-frequency unit are installed on the roof of a high-rise building, and the antenna height is approximately 108 m. The BaseBand Unit (BBU) is placed in an indoor facility and an optical fiber connects the RFU and BBU. On the UE side, the experiment hardware is installed in the test vehicle. The UE antenna is set on the roof of the test vehicle and the antenna height is approximately 3 m. We measured the performance with the vehicle stopped at each point.

The experiment hardware supports the TDD mode. The parameters for this trial are summarized in Table 4.5. The experiment hardware transmits and receives signals in the 4.5 GHz band and the carrier bandwidth is 19.86 MHz. Note that 5.04 MHz within the carrier

bandwidth is allocated to transmitting measurement signals in the test of the type-I frame structure. In this trial, the carrier frequency is 4.66 GHz and the subcarrier spacing is 30 kHz for the type-I frame structure and 60 kHz for the type-II frame structure. Throughout this trial, the signal is transmitted using SFBC. We applied a small number of antennas to reduce the processing time in the measurement of the type-I frame structure. Therefore, the BS uses only two antennas, and the UE uses one antenna for transmission and two antennas for reception. On the other hand, in the evaluation of reliability using the type-II frame structure, the numbers of antennas in the BS and UE are 8 and 2, respectively.

4.6 Results

The trial results are presented in this section. We evaluate the latency and the reliability when using the type-I and type-II frame structures. The performance of A/N-less retransmission is also evaluated in this trial. Then, the decoding rate and the reliability are calculated by transmitting 1 million TBs or packets in this trial.

4.6.1 User-plane latency performance using type-I frame structure

We investigate the user-plane latency performance with the type-I frame structure. In this test, we evaluate the user-plane latency and decoding probability, which is the probability that TBs are correctly received.

In this test, we use a fixed MCS at all test locations. MCS 9 represents QPSK and the coding rate is 0.44. MCS 16 represents 16QAM and the coding rate is 0.45. MCS 28 represents 64QAM and the coding rate is 0.73. The results are given in Tables 4.6 to 4.8.

A user-plane latency of less than 0.5 ms is achieved at all locations; however, the decoding probability of MCS 28 is very low at points B and C. This is because the SNR is not sufficient at these points. The measured latency is almost the same as the estimated value given in Table 4.1.

4.6.2 Reliability performance using type-II frame structure

Next we investigate the retransmission and reliability performance with the type-II frame structure.

Table 4.5 Experiment parameters

Parameter	Case of Type-I frame	Case of Type-II frame
Carrier frequency	4.66 GHz	4.66 GHz
Bandwidth	5.04 MHz	19.86 MHz
Subcarrier spacing	30 kHz	60 kHz
Slot length	7 symbols/slot	14 symbols/slot
Guard period	70.8 μs	31.25 μs
CP length	2.08 μs	1.56 μs
Waveform	f-OFDM	f-OFDM
FFT length	1024	512
# of subcarriers	168	330
Channel coding	Turbo code	Polar code
List size	N/A	8
MIMO mode	SFBC	SFBC
# of leyers	1	1
MCS	Fixed	AMC
Traffic	User defined	Periodic arrivals
# of BS antennas	2 Tx / 2 Rx	8 Tx / 8 Rx
# of UE antennas	1 Tx / 2 Rx	2 Tx / 2 Rx
BS sector direction	North 0 deg.	North 0 deg.
BS antenna tilt	16.4 deg.	16.4 deg.
UE cable loss	less than 1 dB	less than 1 dB
# of UEs	1	1

Table 4.6 U-plane latency performance at point A

MCS #	TB size	U-plane latency	Decoding ratio
9	296 bits	431 μs	100 %
16	600 bits	432 μs	100 %
28	1480 bits	470 μs	100 %

Table 4.7 U-plane latency performance at point B

MCS #	TB size	U-plane latency	Decoding ratio
9	296 bits	440 μs	100 %
16	600 bits	444 μs	100 %
28	1480 bits	512 μs	0.18 %

Table 4.8 U-plane latency performance at point C

MCS #	TB size	U-plane latency	Decoding ratio
9	296 bits	429 μs	100 %
16	600 bits	437 μs	100 %
28	1480 bits	No data	0 %

The reliability is defined as the ratio of the number of correctly received packets within a user-plane latency of less than 1 ms, while the packet success ratio is defined as the ratio of the number of correctly received packets without the constraint of a user-plane latency of below 1 ms. In this test, we basically used Adaptive Modulation and Coding (AMC), for which the algorithm is based on outer-loop link adaptation [65] and the target block error rate is 0.01%, at all test locations.

First, we evaluate the performance without HARQ, with A/N-less retransmission, referred to as mode-I retransmission, and with the combination of A/N-less and A/N-based retransmission, referred to as mode-II retransmission. Then, without HARQ means the transmission without HARQ feedback and retransmission. In the mode-II retransmission, two signals, which are the original signal and its repeated signal, are transmitted at first. If the receiver cannot correctly decode by combining these two received signals, it sends NACK feedback to the transmitter. Subsequently, the transmitter sends the original signal and its repeated signal again. Therefore, the total number of redundant signals is one and three in mode-I and mode-II, respectively. In this test, we calculate the decoding probability based on the number of successfully decoded TBs. Tables 4.9 and 4.10 give the measured performance in the DL and UL, respectively. Focusing on mode-II retransmission, the decoding probability is 100% in the DL and UL for all measurement locations. Mode-I retransmission also improves the decoding probability compared to that without retransmission. However, the improvement is small, and the decoding probability with mode-I retransmission is less than 99.999% at

Table 4.9 DL decoding packet radio with and without retransmission

Location	A	B	C
w/o HARQ	99.9998 %	99.9388 %	99.9899 %
Mode-I	99.9999 %	99.9906 %	99.9948 %
Mode-II	100 %	100 %	100 %

Table 4.10 UL decoding packet radio with and without retransmission

Location	A	B	C
w/o HARQ	99.9999 %	99.9589 %	99.9871 %
Mode-I	99.9999 %	99.9996 %	99.9921 %
Mode-II	100 %	100 %	100 %

points B and C. Thus, mode-I retransmission achieves low latency; however, the decoding probability cannot be improved sufficiently. One difference between mode-I and mode-II is the number of redundancy signals. Although the same two signals are received and combined in mode-I retransmission, the decoding probability is less than 99.999%. Therefore, more than three redundancy signals are required in order to obtain a SNR that can achieve a decoding probability of 99.999% or more at points B and C. Moreover, it is possible that the benefit of time diversity due to sending the same signal is small since the redundancy signal is transmitted continuously and the OFDM symbol is short in the new frame structure. Therefore, we observe that the transmission timing of the redundancy signal for A/N-less retransmission is important to improve the decoding probability.

Second, we evaluate the reliability using the type-II frame structure. IP packets are used for this trial and the tested packet sizes are 32, 50, 100, and 200 bytes. The reliability, the packet success ratio, and the average latency are measured at each location. Table 4.11 and Fig. 4.7 show the measured results at point A. The reliability of 99.999% is achieved in both the DL and UL. However, A/N-based retransmission occurs for a few packets because the reliability is not 100% despite 100% success ratio. Thus, we find that the reliability may be degraded by A/N-based retransmission even for high SNR locations.

Table 4.12 and Fig. 4.8 show the measured results at point B. The reliability is less than 99.999% in both the DL and UL. In the DL, since the reliability level is low regardless of the fact that there is almost no packet error, the DL user-plane latency exceeds 1 ms due to the

Table 4.11 Reliability and packet success rate at point A

Packet size [bytes]	DL (SNR = 26 dB)		UL (SNR = 20 dB)	
	Reliability	Success rate	Reliability	Success rate
32	100 %	100 %	99.9997 %	100 %
50	99.9995 %	100 %	100 %	100 %
100	99.9999 %	100 %	100 %	100 %
200	99.9997 %	100 %	99.9997 %	100 %

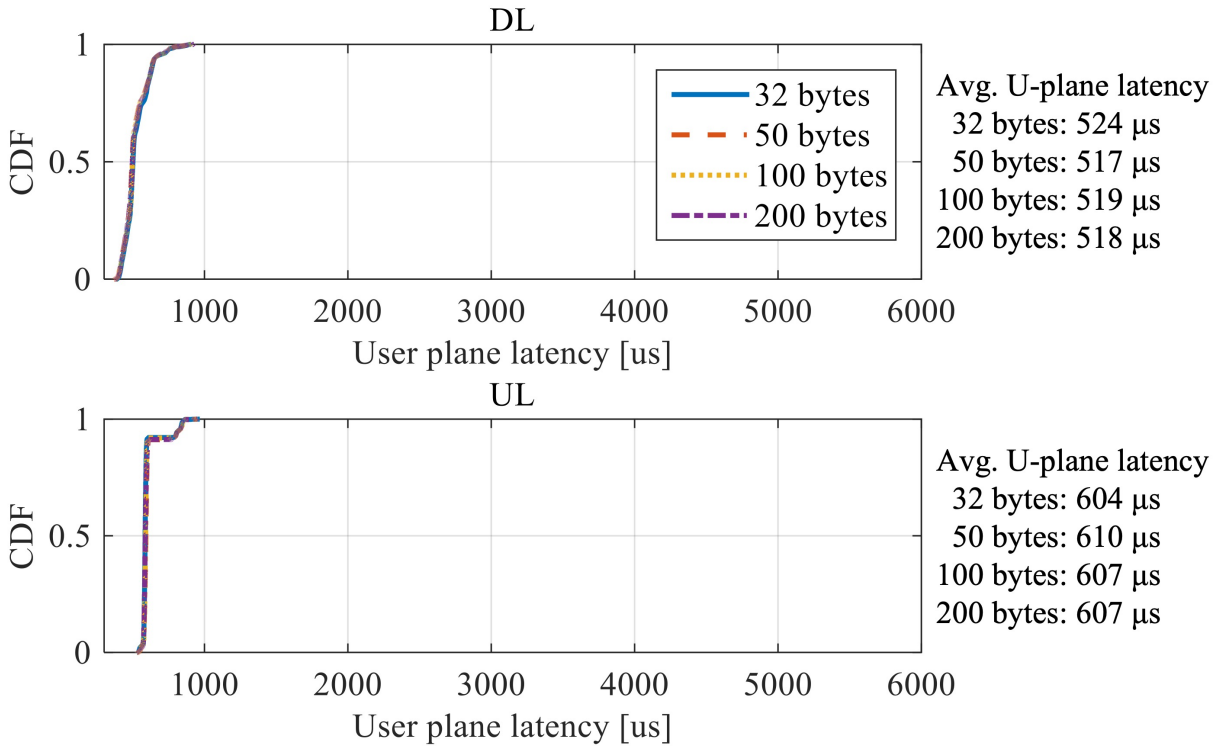

Figure 4.7 CDF of user-plane latency at point A

Table 4.12 Reliability and packet success rate at point B

Packet size [bytes]	DL (SNR = 11 dB)		UL (SNR = -2 dB)	
	Reliability	Success rate	Reliability	Success rate
32	99.9408 %	100 %	86.5136 %	100 %
50	99.9701 %	100 %	71.2481 %	100 %
100	99.9128 %	100 %	18.5628 %	100 %
200	99.9386 %	100 %	0 %	100 %

A/N-based retransmission similar to the case at point A. Focusing on 32 and 50 bytes in the DL, the A/N-based retransmission causes degradation. The average user-plane latency with a packet size larger than 100 bytes is longer than that for the other packet sizes in the DL. This is because the packet size is larger than the TB size, and one packet is divided into two or more TBs. In this case, the user-plane latency may also exceed 1 ms when using the special slot. In the UL, although the packet success ratio is 100%, a larger packet size decreases the reliability. In addition, the UL user-plane latency is longer than the estimated value and a larger packet size increases the latency. Thus, the A/N-based retransmission and the packet segmentation cause a longer delay at point B. Furthermore, since a newly generated packet will not be transmitted until the previous processing is completed, the waiting time becomes long under a low SNR. As a result, especially for 200 bytes, a longer delay is observed in the UL at point B.

Table 4.13 and Fig. 4.9 show the measured results at point C. The reliability of over 99.999% is achieved with packet sizes of 100 bytes and less in the DL. Since the user-plane latency with the 200-bytes packet is approximately 250 μs longer than that with other packet sizes and is shorter than the latency with the A/N-based retransmission, the 200-bytes packet is divided and is transmitted using two TBs in the DL. Despite achieving the packet success ratio of 100% for the packet size of 200 bytes, the reliability is less than 99.999% due to the use of the special slot. In the UL, 99.999% reliability cannot be achieved with all packet sizes. Since the packet success ratio is degraded, it is believed that the channel conditions are poor. Actually, we observe the existence of multiple paths at point C unlike other locations. These paths have almost the same power, and one path with approximately 1.3 μs is also observed. It is possible that the timing of the UL synchronization is delayed due to the strong delayed path. Since the CP length is 1.56 μs in our design, inter-symbol interference

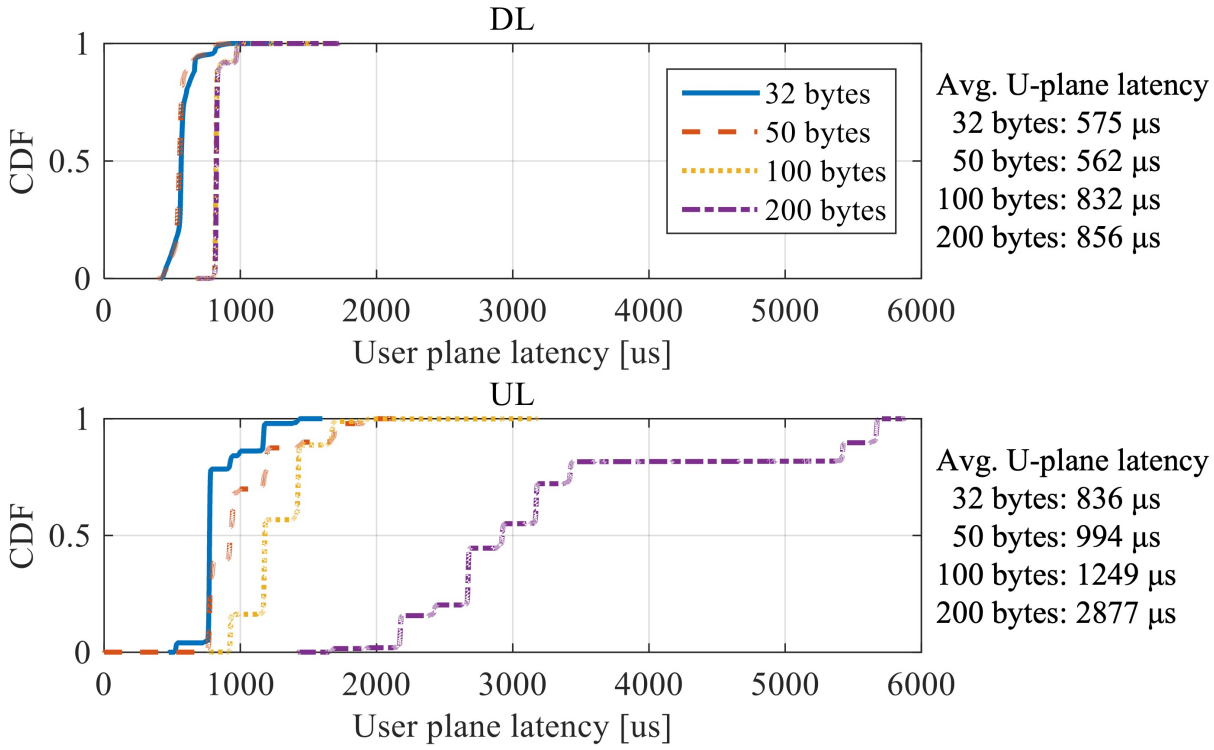

Figure 4.8 CDF of user-plane latency at point B

Table 4.13 Reliability and packet success rate at point C

Packet size [bytes]	DL (SNR = 24 dB)		UL (SNR = 11 dB)	
	Reliability	Success rate	Reliability	Success rate
32	99.9997 %	100 %	99.9830 %	99.9989 %
50	100 %	100 %	99.9751 %	99.9994 %
100	100 %	100 %	97.7684 %	99.9993 %
200	99.9970 %	100 %	52.2192 %	99.9986 %

can easily arise if the synchronization timing is delayed by 1.3 μs. As a result, the packet success ratio is degraded by the delayed path. Therefore, we conclude that retransmission is caused by instantaneous channel degradation or multipaths, which lead to deterioration in the reliability.

Finally, we describe the performance with a fixed MCS index and compare it to the performance with AMC. At point B, we measure the reliability, packet success ratio, and user-plane latency with a fixed MCS and a packet size of 32 bytes. The MCS index is 5 and 4 in the DL and UL, respectively. Both MCS 4 and MCS 5 show QPSK, and the coding rates are 0.25 and 0.32, respectively. The results are given in Table 4.14. The reliability with a fixed MCS is improved compared to that with AMC, and is 99.999% in both the DL and UL. The average DL MCS index is 10 when AMC is used, and the fixed MCS index is lower than the MCS index selected using AMC. Since a lower MCS generally achieves more robust transmissions, the number of retransmissions is reduced in this case. Therefore, the reliability is improved and the average user-plane latency is shortened in the DL. On the other hand, the reliability is improved in the UL although the fixed MCS index is higher than MCS 2 selected using AMC. Focusing on the average user-plane latency, the latency with a fixed MCS is lower than that with AMC. For the fixed MCS case, since the TB size of MCS 4 is much larger than the size of the 32-byte packet, there is no packet segmentation. For the AMC case, packet segmentation may occur according to the selected MCS. The number of packets with retransmission increases because the required SNR is not satisfied when a higher MCS is selected, while packet segmentation occurs because the size of the packet becomes larger than the TB size when a lower MCS is selected. Therefore, to improve reliability performance with AMC, it is important to design the AMC algorithm considering the balance between the success probability and packet segmentation.

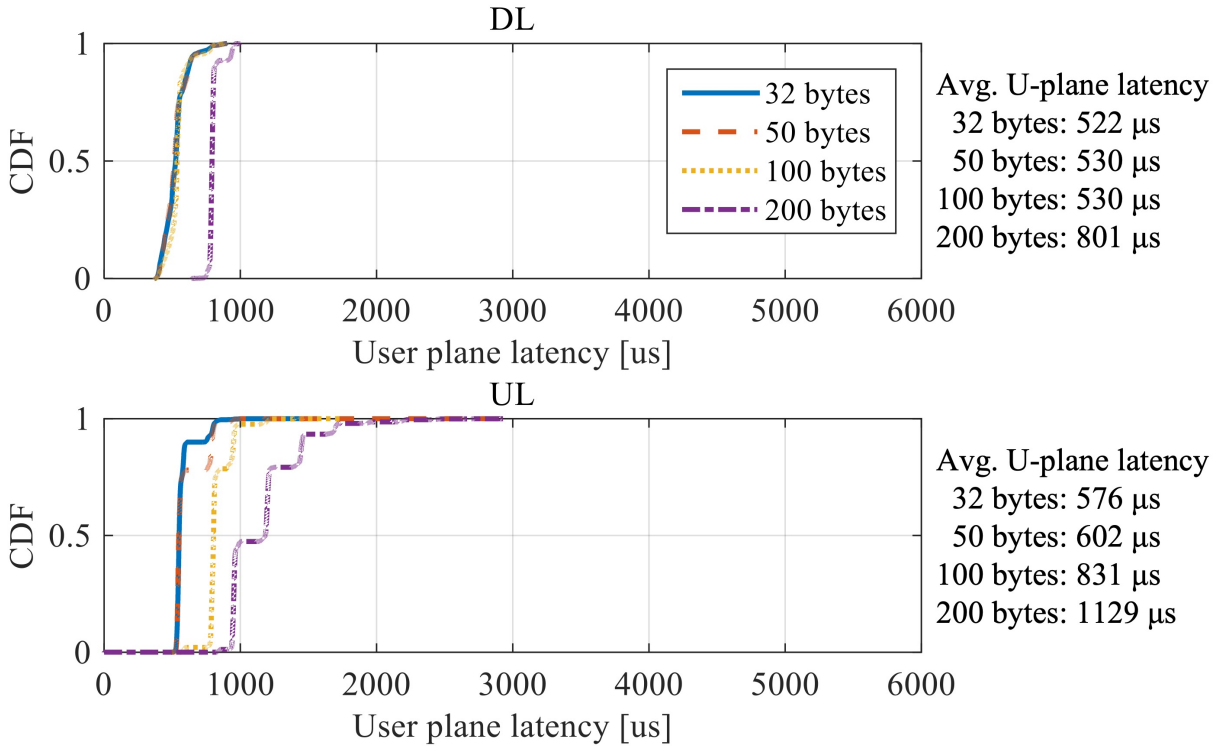

Figure 4.9 CDF of user-plane latency at point C

Table 4.14 Comparison of fixed MCS and AMC

	DL		UL	
	Fixed (MCS 5)	AMC	Fixed (MCS 4)	AMC
Reliability	99.9998 %	99.9408 %	99.9995 %	86.5136 %
Success rate	100 %	100 %	100 %	100 %
U-plane latency	543 μs	578 μs	546 μs	836 μs

4.7 Extensibility of the proposed frame structure

We discuss the extensibility to different OFDM subcarrier spacings and different frequency bands for the frame structure (Type-II) proposed for high reliability. The proposed frame structure transmits the same signals within the period when the channel fluctuation is small, and improves the reception gain. Whether or not similar effects can be expected for different subcarrier spacings and different frequencies can be evaluated from the following viewpoints.

- A certain amount of data can be transmitted within a required delay time (depending on OFDM subcarrier spacing)
- The required delay time is within the period in which the channel does not fluctuate (coherent time) (depending on frequency band)

4.7.1 Scalability for different OFDM subcarrier spacing

To evaluate whether a certain amount of data can be transmitted within a required delay time at different OFDM subcarrier spacings, the evaluation function f shown in Equations 4.1 is defined.

$$f = \frac{N}{M} \geq 1 \tag{4.1}$$

Here, N is the number of slots that can be transmitted within the required delay time, and M is the number of slots required for transmission of a certain amount of data, which can be expressed as Equation 4.2 and 4.3, respectively.

$$N = \left\lfloor \frac{T_d}{L_{slot,\mu}} \right\rfloor \tag{4.2}$$

$$M = \left\lceil \frac{N_b \Delta f(\mu)}{B N_{sym} Q R} \right\rceil \tag{4.3}$$

Then, T_d and $L_{slot,\mu}$ are a required delay time and a slot length with OFDM subcarrier spacing index $\mu(= 0, 1, 2, 3, 4)$. The OFDM subcarrier spacing $\Delta f(\mu)$ is expressed as $\Delta f(\mu) = 15 \times 2^{\mu}$. In Equation 4.3, N_b, B, N_sym are the number of transmitted bit per packet, transmission bandwidth and the number of OFDM symbols for data transmission, respectively. Q and R indicate modulation order and code rate, respectively. If the evaluation function f is less

Table 4.15 Evaluation parameters for the scalability of the proposed frame structure

Parameter	Value
Required delay time T_d	0.5 ms
Transmitted bits per packet N_b	1600 bits
Transmission bandwidth B	19820 kHz
Number of OFDM symbols for data transmission N_{sym}	2
$Q \times R$	4

than 1, it means that all data cannot be sent within T_d. If f is greater than 1, it can be said that the proposed frame structure can be applied to the OFDM subcarrier spacing. Figure 4.10 shows the evaluation results based on Equation 4.1-4.3. Table 4.15 shows the evaluation parameters. Here, the T_d is set to a value obtained by subtracting the DL signal processing delay of 0.5 ms shown in Table 4.2 from the URLLC required delay of 1 ms. From Figure 4.10, it can be said that the proposed frame structure can be applied if the OFDM subcarrier spacing is 30 kHz or more. However, considering that the signal processing delay has delay jitter, it may be suitable for OFDM subcarrier spacing of 60 kHz or more.

4.7.2 Scalability for different frequency band

From the viewpoint of frequency, it is a condition to apply the proposed frame structure that the required delay time is within the coherent time. It is known that the coherent time T_c can be expressed by the following equation [66].

$$T_c \approx \sqrt{\frac{9}{16\pi}}\frac{1}{f_m} = \sqrt{\frac{9}{16\pi}}\frac{c}{v f_c} \geq T_d \tag{4.4}$$

Then, f_m is the maximum Doppler spread which can be expressed using light speed c, user velocity v and center frequency f_c. If T_c exceeds the required delay time T_d, the radio channel does not fluctuate greatly while the proposed frame structure can be transmitted within T_d. Then, the reception gain can be obtained by retransmission. Since the proposed frame structure assumes that the radio channel does not fluctuate during retransmission, the effect of the proposed frame structure is not guaranteed if this condition is not met. Figure 4.11 shows the region that satisfies the condition $T_c \geq T_d$. As the user velocity and the center frequency increase, it may be difficult to satisfy the condition. If the millimeter-wave band is

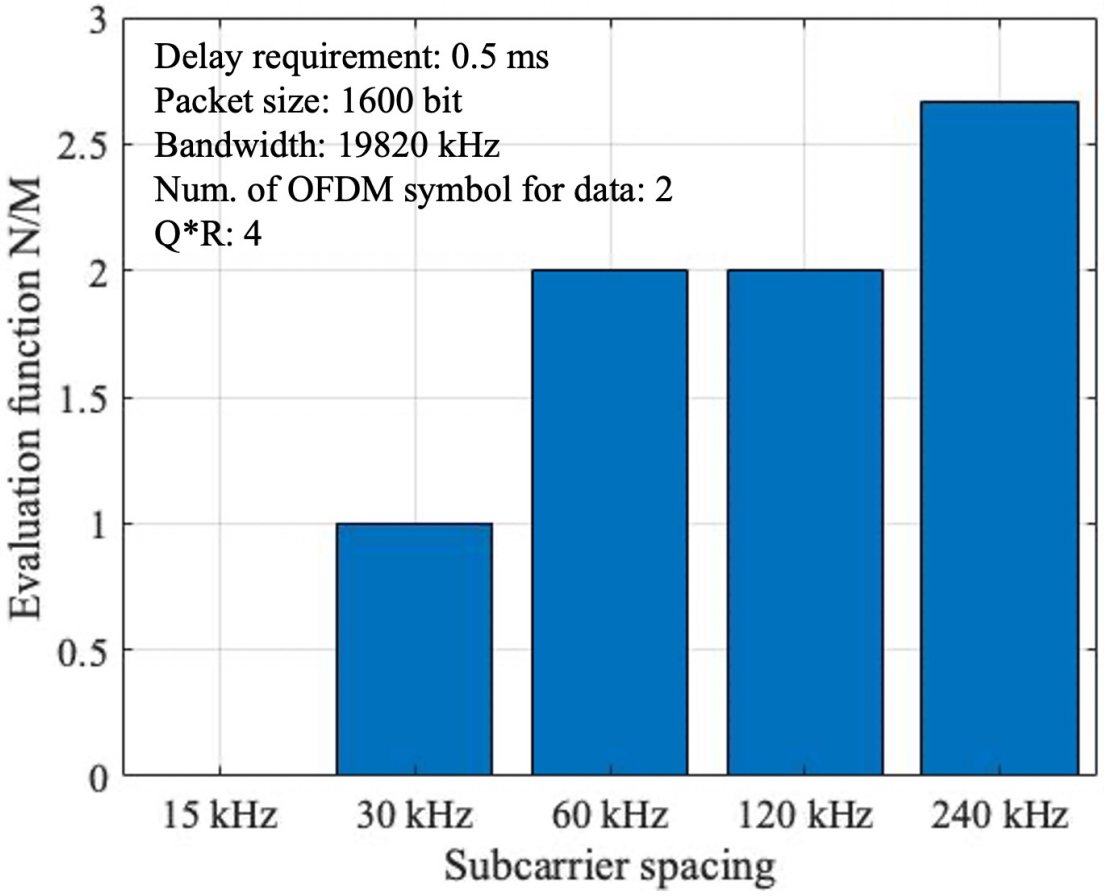

Figure 4.10 OFDM subcarrier spacing that can extend the proposed frame structure

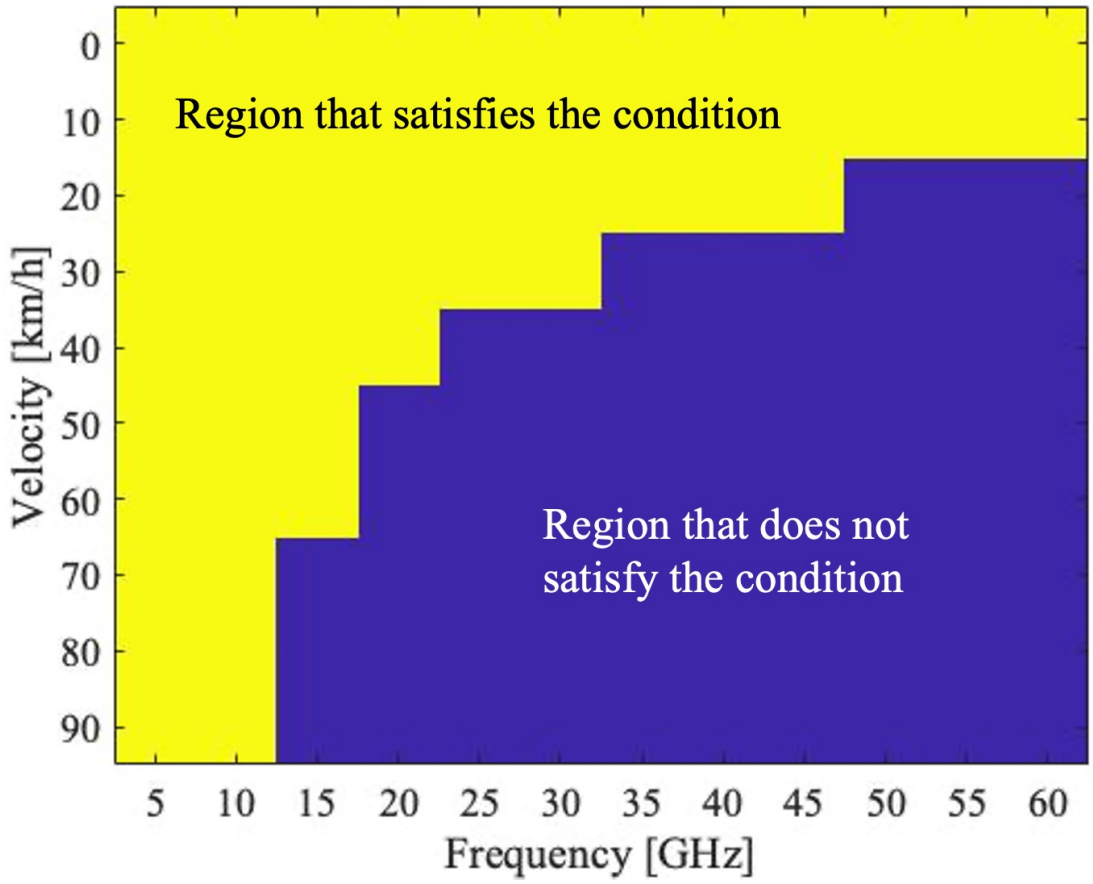

Figure 4.11 Frequency that can extend the proposed frame structure

used, it satisfies the condition when the user velocity is slow. However, further investigation is required when considering application to high-speed mobility.

4.8 Summary

This chapter presented frame structures for time resource redundancy and field trials to verify the feasibility of URLLC in a real environment. To meet the user-plane latency and the reliability requirements defined by the 3GPP for URLLC, a new radio interface with a new frame structure including a wider subcarrier spacing, and A/N-less retransmission was used. The field trial demonstrated the user-plane latency of less than 0.5 ms using the type-I

frame structure (30-kHz subcarrier spacing). Moreover, the reliability of 99.999% is achieved with up to the packet size of 200 bytes using the type-II frame structure (60-kHz subcarrier spacing). With the packet size of 32 bytes, the reliability of 99.999% is achieved even at low SNR and NLOS locations. Meanwhile, the trial also showed that it is important to overcome multipaths and improve AMC for URLLC in order to maintain reliability over a wide area. In this experiment, although a 5GHz system was used, the frame structure with redundant time resources can be applied regardless of the frequency band. The region clarified by the experiment is shown in Figure 4.12. In the mmWave band, wider OFDM subcarrier spacing can be applied, so multiple same signals can be transmitted within 1 ms. Therefore, the effect of this approach in the mmWave band can also be expected.

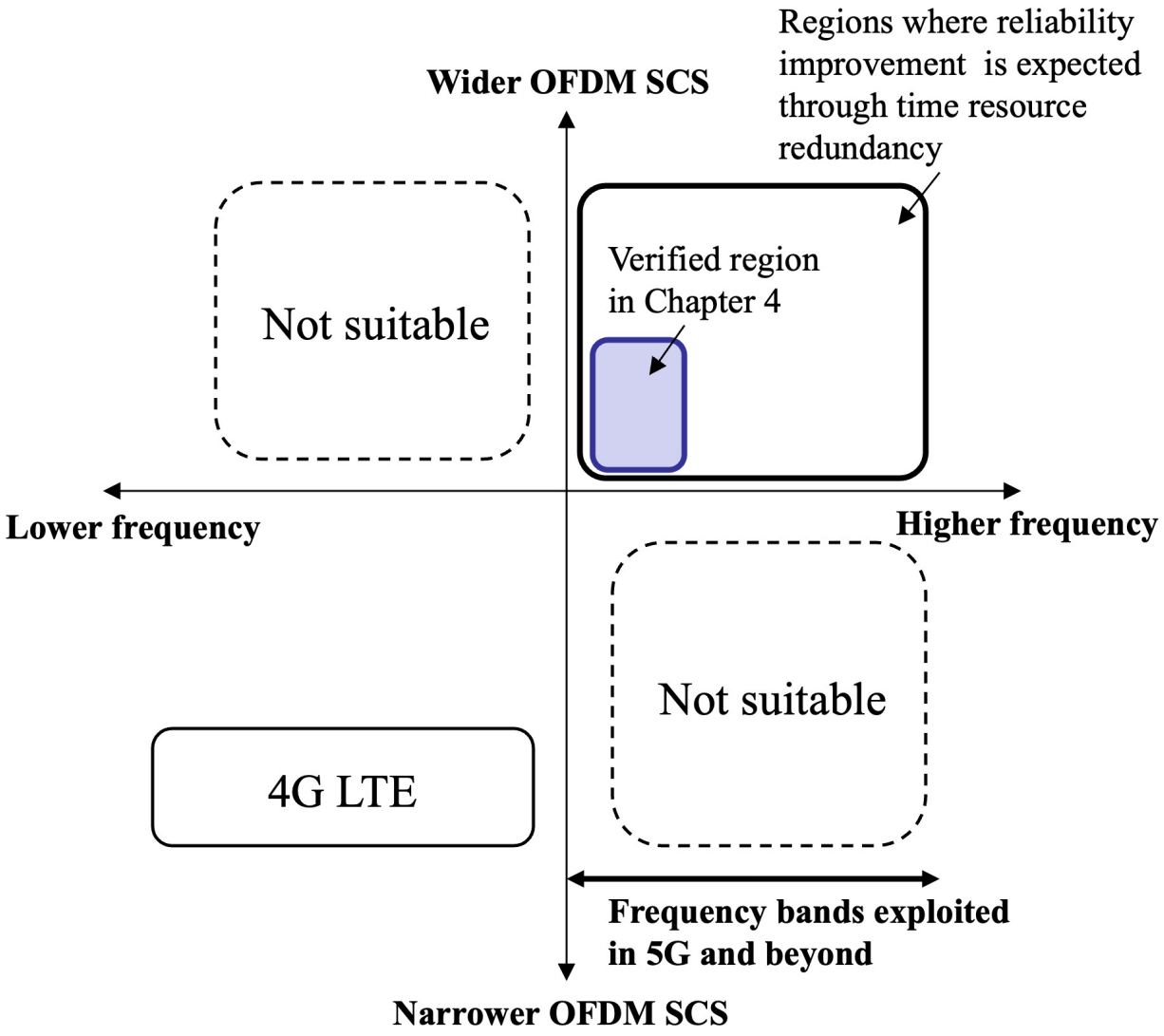

Figure 4.12 The region clarified by the experiment

Chapter 5

Conclusion

5.1 Summary

This chapter concludes this thesis. In this study, we investigated the application of millimeter wave to mobile communications. The thesis has clarified the potential and issues of millimeter waves, and studied an approach for resource redundancy that utilizes the abundant resources of mmWave.

Chapter 2 presented a system design for 39-GHz bands and experiments using the system to provide high data rates and long-range communications with mobility support. The experiments used a high beamforming gain antenna and beam-tracking technology to achieve throughput of 1 Gbit/s or more, and we achieved throughput of 3.35 Gbit/s and 2.14 Gbit/s at a transmission range of 1450 m and 1850 m, respectively. Moreover, the experimental results show high throughput can be obtained even in NLOS locations, and we achieved 3.74 Gbit/s at an NLOS location. Furthermore, with 20-km/h mobility we achieved throughput of 1.58 Gbit/s. However, in order to utilize mmWave for mobile communications, expanding the coverage to NLOS areas and improving the beam searching and tracking method are important challenges in the future. Additionally, although we were able to conduct measurements without rain in these experiments, it is known mmWave bands are affected by rain attenuation. Also in the 39-GHz band, approximately 8-dB/km attenuation is caused by heavy rain (The rainfall rate is 25 mm/h) [25]. In the deployment process for wide-area coverage using 39 GHz, we must consider and investigate the effect of rain attenuation. Furthermore, assuming applications and services, comprehensive verification considering upper layers, e.g., the TCP/IP layer, is also important in the future.

Chapter 3 proposed a user-driven relay beamforming method of massive analog-relay MIMO as spatial-resource redundancy. The proposed method enables relay beam search and tracking in analog relays and can reduce the overhead of beam control. To reduce the overhead, the RNs utilize UEs location, speed, velocity, acceleration, direction. The UE information is notified by using CAM. Simulations show that the proposed method can benefit from massive analog-relay MIMO and significantly reduce the overhead. One result indicates the massive analog-relay MIMO with the proposed method can improve the rate by about 72 % due to the multiplexing gain of 4-streams MIMO. Then, the overhead is CAM transmission only. The accuracy of the location information, the control period, and the effects of UE mobility are also evaluated. The result clarifies that it is desirable for the terminal to have cm-meter level positioning when applying the pro-posed method. Further, we show that the proposed relay beam tracking method works effectively for the impact of UE mobility and the cycle of UE location update.

Chapter 4 presented frame structure for time resource redundancy and field trials to verify the feasibility of URLLC in a real environment. To meet the user-plane latency and the reliability requirements defined by the 3GPP for URLLC, a new radio interface with a new frame structure including a wider subcarrier spacing, and A/N-less retransmission was used. The field trial demonstrated the user-plane latency of less than 0.5 ms using the type-I frame structure (30-kHz subcarrier spacing). Moreover, the reliability of 99.999% is achieved with up to the packet size of 200 bytes using the type-II frame structure (60-kHz subcarrier spacing). With the packet size of 32 bytes, the reliability of 99.999% is achieved even at low SNR and NLOS locations. Meanwhile, the trial also showed that it is important to overcome multipaths and improve AMC for URLLC in order to maintain reliability over a wide area. In this experiment, although a 5GHz system was used, the frame structure with redundant time resources can be applied regardless of the frequency band. In the mmWave band, wider OFDM subcarrier spacing can be applied, so multiple same signals can be transmitted within 1 ms. Therefore, the effect of this approach in the mmWave band can also be expected. The experiments for mmWave bands is the future work.

5.2 Suggestion for future research directions

This section explains the future several research directions related to the work presented in this thesis.

5.2.1 Further reliability improvement in environments with frequent changes

A certain effect was confirmed by retransmission (Time-resource redundancy) in Chapter 4. However, further reliability improvements are required for applications in the millimeter-wave bands with high-speed mobility and in environments with frequent changes. Combining multiple resources redundancy is one of the approaches to improve reliability.

5.2.2 Redundancy control of radio resources according to the environments and user requirements

As shown in this thesis, radio resource redundancy can improve the performance of the millimeter-wave bands. However, the redundancy leads to a decrease in communication efficiency, so the improvement of system efficiency is also important aspect. In mobile communication systems, it is extremely difficult to achieve both system efficiency and reliability. Therefore, it is important to understand the user's requirements and the communication environments, and to be able to appropriately control the balance between the efficiency and reliability for further utilization of the millimeter wave bands.

5.2.3 Experimental verification

In this thesis, spatial and time resources was separately studied. However, both methods can be combined. It is also important for the popularization of millimeter waves to demonstrate this together with other future research.

Appendix I

List of Publications

I.1 Journal papers

1. M. Iwabuchi, A. Benjebbour, Y. Kishiyama, G. Ren, C. Tang, T. Tian, L. Gu, Y. Cui, and T. Takada, 5G Experimental Trials for Ultra-Reliable and Low Latency Communications Using New Frame Structure, IEICE transaction on communications, Vol. E102-B, No. 2, pp.381-390, Feb., 2019.

2. M. Iwabuchi, A. Benjebbour, Y. Kishiyama, G. Ren, C. Tang, T. Tian, L. Gu, Y. Cui, and T. Takada, Outdoor Experiments on Long-Range and Mobile Communications Using 39-GHz Band for 5G and Beyond, IEICE transaction on communications, Vol. E102-B, No. 8, pp. 1437-1446, Aug., 2019.

3. K. Sakaguchi, T. Yoneda, M. Iwabuchi, and T. Murakami, Mmwave massive analog-relay MIMO, ITU J-FET,Vol. 2, Issue 6, pp. 43-55, 2021.

4. M. Iwabuchi, Y. Ramamoorthi, and K. Sakaguchi, User-driven relay beamforming in massive analog relay MIMO, https://doi.org/10.3390/s23021034, MDPI Sensors, 23(2), 1034; Jan. 2023.

I.2 Journal papers not related to this thesis (including co-authored)

1. M. Iwabuchi, K. Sakaguchi, and K. Araki, "Study on multi-channel receiver based on polyphase filter bank", IEICE transactions on communications, Vol. J91-B, No. 11, pp.1393-1400, Nov. 2008.

2. A. Kishida, M. Iwabuchi, T. Shintaku, T. Onizawa, T. Sakata, T. Hiraguri, and K. Nishimori, User-Oriented QoS Control Method Based on CSMA/CA for IEEE802.11 Wireless LAN System, IEICE transaction on communications, Vol. E96-B, No. 2, pp.419-429, Feb. 2013.

3. A. Kishida, M. Iwabuchi, T. Shintaku, T. Onizawa, and T. Sakata, "Frame Collision Reduction Method Employing Adaptive Transmission Control for IEEE802.11 Wireless LAN System", IEICE transaction on communications, Vol. E97-B, No. 9, pp.1790-1799, Sept. 2014.

4. T. Onizawa, H. Shibayama, M. Iwabuchi, A. Kishida, M. Umeuchi, and T. Sakata, A New Simple Packet Combining Scheme Employing Maximum Likelihood Detection for MIMO-OFDM Transmission in Relay Channels, IEICE transaction on communications, Vol. E97-B, No. 5, pp.1094-1102, May 2014.

5. T. Shintaku, M. Iwabuchi, T. Onizawa, and T. Sakata, "Experimental Evaluation of a Grouping QoS Control Scheme for Wireless Equipment in IEEE802.11 Wireless LAN Stations", IEICE transaction on communications, Vol. J99-B, No. 8, pp.602-611, Aug. 2016.

6. P. Guan, D. Wu, T. Tian, J. Zhou, X. Zhang, L. Gu, A. Benjebbour, M. Iwabuchi, and Y. Kishiyama, 5G Field Trials-OFDM-based Waveforms and Mixed Numerologies, IEEE Journal on Selected Area in Communications, Vol. 35, Issue: 6, pp.1234-1243, June 2017.

7. M. Arai, M. Iwabuchi, K. Sakaguchi, and K. Araki, Optimal Design Method of MIMO Antenna Directivities and Corresponding Current Distributions by Using Spherical Mode Expansion, IEICE transaction on communications, Vol. E100-B, No. 10, pp.1891-1903, Oct. 2017.

8. R. Ohmiya, T. Murakami, M. Nishino, Y. Ramamoorthi, M. Iwabuchi, T. Ogawa, and Y. Takatori, "Massive distributed IRS aided wireless communication with ON/OFF selection", ITU J-FET, Vol. 2, Issue 6, pp.83-92, 2021.

9. Y. Ramamoorthi, R. Ohmiya, M. Iwabuchi, T. Ogawa, and Y. Takatori, "Resource Allocation and Sharing Methodologies When Reconfigurable Intelligent Surfaces Meet Multiple Base Stations", MPDI sensors, July 2022.

10. Y. Ramamoorthi, M. Iwabuchi, T. Murakami, T. Ogawa, and Y. Takatori. "Resource Allocation for Reconfigurable Intelligent Surface Assisted Dual Connectivity", MPDI sensors, August 2022.

11. H. Hashida, Yuichi Kawamoto, N. Kato, M. Iwabuchi, and T. Murakami, "Mobility-Aware User Association Strategy for IRS-Aided mm-Wave Multibeam Transmission Towards 6G", IEEE Journal on Selected Areas in Communications, Vol. 40, Issue 5, 2022.

I.3 International conferences

1. M. Iwabuchi, A. Benjebbour, Y. Kishiyama, G. Ren, C. Tang, T. Tian, L. Gu, T. Takada, and T. Kashima, "5G Field Experimental Trials on URLLC Using New Frame Structure", 2017 IEEE Globecom Workshops.

2. M. Iwabuchi, A. Benjebbour, Y. Kishiyama, G. Ren, C. Tang, T. Tian, L. Gu, T. Takada, and Y. Cui, "Evaluation of Coverage and Mobility for URLLC via Outdoor Experimental Trials", 2018 IEEE 87th Vehicular Technology Conference (VTC Spring) workshops.

3. A. Benjebbour, M. Iwabuchi, Y. Kishiyama, W. Guangjian, L. Gu, Y. Cui, and T. Takada, "Outdoor Experimental Trials of Long Range Mobile Communications Using 39 GHz", 2018 IEEE 87th Vehicular Technology Conference (VTC Spring).

I.4 International conferences not related to this thesis (including co-authored)

1. M. Iwabuchi, K. Sakaguchi, and K. Araki, "Study on multi-channel receiver based on polyphase filter bank", 2008 2nd International Conference on Signal Processing and Communication Systems, 2008.

2. M. Arai, M. Iwabuchi, K. Sakaguchi, and K. Araki, "Optimization of diversity antenna directivities based on spherical mode expansion", 2010 Asia-Pacific Microwave Conference, 2010.

3. M. Iwabuchi, A. Kishida, T. Shintaku, T. Onizawa, and T. Sakata, "Cooperative back-off control scheme for point-to-point simultaneous transmission using capture effect", 2014 Asia-Pacific Microwave Conference, 2014.

4. T. Shintaku, A. Kishida, M. Iwabuchi, T. Onizawa, and T. Sakata, "Experimental evaluation of a grouping method employing network allocation vector based on IEEE802.11 wireless LAN", 2014 Asia-Pacific Microwave Conference, 2014.

5. M. Iwabuchi, A. Benjebbour, Y. Kishiyama, D. Wu, T. Tian, L. Gu, Y. Cui, and T. Kashima, "5G Field Experimental Trial on Frequency Domain Multiplexing of Mixed Numerology", 2017 IEEE 85th Vehicular Technology Conference (VTC Spring) workshops.

6. L. Gu, T. Tian, Y. Dou, G. Ren, M. Iwabuchi, J. Tsuboi, and Y. Kishiyama, "Millimeter Wave Multi-Hop Mobility and Trial Activities", 2018 Asia-Pacific Microwave Conference, 2018.

7. T. Tian, Y. Dou, G. Ren, L. Gu, J. Chen, Y. Cui, T. Takada, M. Iwabuchi, J. Tsuboi, and Y. Kishiyama, "Field Trial on Millimeter Wave Integrated Access and Backhaul", 2019 IEEE 89th Vehicular Technology Conference (VTC2019-Spring), 2019.

8. M. Iwabuchi, J. Tsuboi, Y. Hokazono, Y. Kishiyama, P. Wainio, M. Zierdt, M. Holyoak, J. Kepler, S. Shahramian, P. Rasky, R. Nikides, and A. Ghosh, "93-GHz Experiments with Phased Array Antenna in Anechoic Chamber for 5G Evolution and Beyond", 2019 IEEE Asia-Pacific Microwave Conference, 2019.

I.5 Domestic conferences

1. M. Iwabuchi, T. Murakami, T. Yoneda, and K. Sakaguchi, "", 2021 IEICE Society conference, Sept. 2021.

Reference

[1] E. Bastug, M. Bennis, and M. Debbah. Living on the edge: The role of proactive caching in 5g wireless networks. IEEE Communication Magazine, Vol. 52, No. 8, pp. 8289, August 2014.

[2] Recommendation ITU-R M.2083-0: IMT Vision Framework and overall objectives of the future development of IMT for 2020 and beyond, Sept. 2015.

[3] 3GPP TR 38.913, Study on scenarios and requirements for next generation access technologies, March 2017.

[4] 3GPP TR 38.211 V15.0.0: NR; Physical channels and modulation (Release 15), Dec. 2017.

[5] L. Matti, L. Kari, Key driver and research challenges for 6G ubiquitous wireless intelligence, Sept. 2019.

[6] NTT DOCOMO, Inc., White paper: 5G Evolution and 6G (Version 4.0), Jan. 2022.

[7] H. Tataria, M. Shafi, A. F. Molisch, M. Dohler, H. Sjöland, and F. Tufvession, 6G Wireless Systems: Vision, Requirements, Challenges, Insights, and Opportunities, Proceedings of the IEEE, Vol. 109, Issue: 7, March 2021.

[8] Y. Niu, Y. Li, D. Jin, L. Su, and A. V. Vasilakos, "A survey of millimeter wave communications (mmWave) for 5G: opportunities and challenges", Wireless Netw 21, 26572676 (2015). https://doi.org/10.1007/s11276-015-0942-z, April 2015.

[9] A. Benjebbour, et al., 3GPP defined 5G requirements and evaluation conditions, NTT DOCOMO Technical Journal, Vol. 19, No. 3, Jan. 2018.

[10] ITU Resolution COM6/20, Provisional final acts world radio conference 2015, Nov. 2015.

[11] A. I. Sulyman, et al., "Radio propagation path loss models for 5G cellular networks in the 28 GHZ and 38 GHZ millimeter-wave bands," IEEE Communications Magazine, vol. 52, no. 9, pp. 78-86, 2014.

[12] T. S. Rappaport, et al., "Broadband millimeter-wave propagation measurements and models using adaptive-beam antennas for outdoor urban cellular communications," IEEE Transactions on Antennas and Propagation, vol. 61, no. 4, pp. 1850-1859, 2013.

[13] S. Sun, et al., "Path loss shadow fading and line-of-sight probability models for 5G urban macro-cellular scenarios," 2015 IEEE Globecom Workshops (GC Workshops), pp. 1-7, 2015.

[14] T. Obara, et al., "Experiment of 28 GHz band 5G super wideband transmission using beamforming and beam tracking in high mobility environment," 2016 IEEE 27th Annual International Symposium on Personal, Indoor, and Mobile Radio Communications (PIMRC), Sept. 2016.

[15] D. Kurita, et al., "Outdoor experiments on 5G radio access using distributed MIMO and beamforming in 28-GHz frequency band," 2017 IEEE 28th Annual International Symposium on Personal, Indoor, and Mobile Radio Communications (PIMRC), Oct. 2017.

[16] S. Yoshioka, et al., "Field experimental evaluation of beamtracking and latency performance for 5G mmWave radio access in outdoor mobile environment," 2016 IEEE 27th Annual International Symposium on Personal, Indoor, and Mobile Radio Communications (PIMRC), Sept. 2016.

[17] X. Li, et al., A 39 GHz MIMO transceiver based on dynamic multi-beam architecture for 5G communication with 150 meter coverage, 2018 IEEE/MTT-S International Microwave Symposium (IMS), June 2018.

[18] A. Benjebbour, et al., Outdoor experimental trials of long range mobile communications using 39 GHz, Proc. of 2018 IEEE 87th Vehicular Technology Conference (VTC Spring), June 2018.

[19] S. Suyama, et al., 5G multi-antenna technology, DOCOMO Technical Journal, vol. 17, no. 4, April 2016.

[20] W. Tang, et al., "Discrete coordinate transformation for designing all-dielectric flat antennas," IEEE Transactions on Antennas and Propagation, vol. 58, no. 12, Dec. 2010.

[21] C. Mateo-Segura, et al., Flat Luneburg lens via transformation optics for directive antenna applications, IEEE Trans. Antennas Propag., vol. 62, no. 4, pp. 19451953, Apr. 2014.

[22] H. Bölcskei, et al., Impact of the propagation environment on the performance of space-frequency coded MIMO-OFDM, IEEE Journal on Selected Areas in Communications, Vol. 21, Issue 3, pp. 427-439, April 2003.

[23] 3GPP TS 36.211 V15.2.0, Evolved Universal Terrestrial Radio Access (E-UTRA); Physical channel and modulation (Release 15), June 2018.

[24] D. S. Baum, D. Gore, et al., Measurements and characterization of broadband MIMO fixed wireless channels at 2.5 GHz, Proc. of ICPWC00, Dec. 2000.

[25] T S. Rappaport, et al., Millimeter wave mobile communications for 5G cellular: It will work! IEEE Access, Vol. 1, pp. 335-349, May 2013.

[26] A. Shahsin, A. Belogaev, A. Krasilov, and E. Khorov, "Adaptive Transmission Parameters Selection Algorithm for URLLC Traffic in Uplink," 2020 International Conference Engineering and Telecommunication (En&T), Nov. 2020.

[27] 3GPP TS 38.306, "5G NR User Equipment (UE) radio access capabilities (version 15.2.0, Release 15)," Sept. 2018.

[28] 3GPP TR 38.901 V14.3.0, 5G; Study on channel model for frequencies from 0.5 to 100 GHz (version 14.3.0, Release 14), Jan. 2018.

[29] M. Boban, A. Kousaridas, K. Manolakis, J. Eichinger, and W. Xu, Connected Roads of the Future: Use Cases, Requirements, and Design Considerations for Vehicle-to-Everything Communications, IEEE Vehicular Technology Magazine, Vol. 13, Is-sue: 3, Sept. 2018.

[30] M. Iwabuchi, A. Benjebbour, Y. Kishiyama, G. Ren, C. Tang, T. Tian, L. Gu, Y. Cui, T. Takada, Outdoor Experiments on Long-Range and Mobile Communications Using 39-GHz Band for 5G and Beyond, IEICE transaction on communications, Vol. E102-B, No. 8, pp. 1437-1446, Aug. 2019.

[31] Q. Wu, and R. Zhang, Towards Smart and Reconfigurable Environment: Intelligent Reflecting Surface Aided Wireless Network, IEEE Communications Magazine, Vol. 58, Issue: 1, Jan. 2020.

[32] E. C. Strinati, et al., Reconfigurable, Intelligent, and Sustainable Wireless Environments for 6G Smart Connectivity, IEEE Communications Magazine, Vol. 59, Issue: 10, Oct. 2021.

[33] 3GPP TS 38.174 V16.0.0, 5G NR Integrated Access and Backhaul (IAB) radio transmission and reception (Release 16), Nov. 2020.

[34] E. Basar, M. D. Renzo, J. D. Rosny, M. Debbah, M.-S. Alouini, and R. Zhang, Wireless Communications Through Reconfigurable Intelligent Surfaces, IEEE Access, Vol. 7, Aug. 2019.

[35] L. Dai, et al., Reconfigurable Intelligent Surface-Based Wireless Communications: Antenna Design, Prototyping, and Ex-perimental Results, IEEE Acess, Vol. 8, March 2020.

[36] 3GPP TR 38.867 V1.0.0, Study on NR network-controlled repeaters (Release 18), Sept. 2022.

[37] H. Abbas, and K. Hamdi, "Millimeter Wave Communications over Relay Networks", 2017 IEEE Wireless Communications and Networking Conference, March 2017.

[38] K. Sakaguchi, T. Yoneda, M. Iwabuchi, and T. Murakami, Mmwave massive Analog relay MIMO, ITU Journal on Future and Evolving Technologies, Vol. 2, Issue 6, pp. 43-55, Sept. 2021.

[39] ETSI EN 302 637-2, V1.4.1, Intelligent Transport Systems (ITS); Vehicular Communications; Basic Set of Applications; Part 2: Specification of Cooperative Awareness Basic Service, April 2019.

[40] J. Choi, V. Va, N. Gonzalez-Prelcic, R. Daniels, C. R. Bhat, and R. W. Heath, "Millimeter-Wave Vehicular Communication to Support Massive Automotive Sensing", IEEE Communication Magazine, Vol. 54, Issue 12, Dec. 2016.

[41] T. Shimizu, V. Va, G. Bansal, and R. W. Heath, "Millimeter Wave V2X Communications: Use Cases and Design Considera-tions of Beam Management", 2018 Asia-Pacific Microwave Conference, 2018.

[42] S. Han, C. I, Z. Xu, and C. Rowell, "Large-scale antenna systems with hybrid analog and digital beamforming for millimeter wave 5G", IEEE Communication Magazine, Vol. 53, Issue: 1, Jan. 2015.

[43] R. Keating, M. Säily, J. Hulkkonen, and J. Karjakainen, Overview of Positioning in 5G New Radio, 2019 16th International Symposium on Wireless Communication Systems (ISWCS), Aug. 2019.

[44] V. A. Reddy, and G. L. Stüber, Multi-User Position Estimation and Performance Trade-offs in IEEE 802.11az WLANs, 2022 IEEE 95th Vehicular Technology Conference: (VTC2022-Spring), June 2022.

[45] J.-H. Ahn, and J.-H. Won, Location Based on Lidar and GNSS for Connected Vehicles, 2020 IEEE/ION Position, Location and Navigation Symposium (PLANS), April 2020.

[46] Q. Liu, et al., A highly accurate positioning solution for C-V2X systems, MDPI Sensors, Vol.21, Issue 4, Feb. 2021. Availa-ble: https://doi.org/10.3390/s21041175.

[47] M. H. C. Garcia, A. Molina-Galan, M. Boban, J. Gonzalez, B. Coll-Perales, and A. Kousaridas, A Tutorial on 5G NR V2X communications, IEEE Commun. Surveys & Tutorials, Vol. 23, No. 3, Third quarter 2021.

[48] Y. R. Li, B. Gao, X. Zhang, and K. Huang, "Beam Management in Millimeter-wave Communications for 5G and Beyond", IEEE Access, Vol. 8, Jan. 2020.

[49] B. Sadhu, et al., A 24-to-30GHz 256-Element Dual-Polarized 5G Phased Array with Fast Beam-Switching Support for >30,000 Beams, 2022 IEEE International Solid- State Circuits Conference, Feb. 2022.

[50] CAR 2 CAR Communication Consortium Technical Report 2052, "Survey on ITS-G5 CAM statistics", Dec. 2018.

[51] Recommendation ITU-R M.2083-0, IMT-vision Framework and overall objectives of the future development of IMT for 2020 and beyond, Sept. 2015.

[52] A. Osseiran, F. Boccardi, V. Braun, K. Kusume, P. Marsch, M. Maternia, O. Queseth, M. Schellmann, H. Schotten, H. Taoka, H. Tullberg, M A. Uusitalo, B. Timus, and M. Fallgren, Scenarios for 5G mobile and wireless communications: The vision of the METIS project, IEEE Communication Magazine, vol. 52, issue 5, May 2014.

[53] NGMN, NGMN 5G white paper, Feb. 2015.

[54] 3GPP TR 38.913 v14.0.0, Study on scenarios and requirements for next generation access technologies; (Release 14), Oct. 2016.

[55] 3GPP, R1-168371, WF on URLLC evaluation parameter and LLS method, Aug. 2016.

[56] 3GPP, R1-1609664, Comparison of slot and mini-slot based approaches for URLLC, Oct. 2016.

[57] 3GPP, R1-1609663, On the mini-slot structure, Oct. 2016.

[58] P. Kala, M. Casta, J. Salmi, K. Leppännen, T. Turkka, T. Hiltunen, and M. Hronec, A novel radio frame structure for 5G dense outdoor radio frame structure for 5G dense outdoor radio access networks, 2015 IEEE 81st Vehicular Technology Conference (VTC Spring), May 2015.

[59] 3GPP, R1-167269, On the URLLC transmission formats for NR TDD, Aug. 2016.

[60] 3GPP, TS 38.211 v15.0.0, NR; Physical channels and modulation, Dec. 2017.

[61] K. Pedersen, F. Frederiksen, and G. Berardinelli, A flexible frame structure for 5G wide area, 2015 IEEE 82nd Vehicular Technology Conference (VTC Fall), Sept. 2015.

[62] 3GPP R1-1611220, Overview of UL URLLC support in NR, Nov. 2016.

[63] 3GPP TS 36.211 v14.0.0, Evolved Universal Terrestrial Radio Access (E-UTRA); Physical channel and modulation, Sept. 2016.

[64] 3GPP TR 36.912 v14.0.0, Feasibility study for Further Advancements for E-UTRA (LTE-Advanced), April. 2017.

[65] A. Duran, M. Toril, and F. Ruiz, Self-optimization algorithm for outer loop link adaptation in LTE, IEEE Communication Letters, vol. 19, Issue 11, Nov. 2015.

[66] T.S. Rappaport, Wireless Communications, Prentice Hall, 2002.